Understanding the Reactivities and Mechanisms of Action of Organosilicons as Additives for Next-Generation Lithium-ion Battery Electrolytes

By

Louis Vincent Morris

A dissertation submitted in partial fulfillment of

the requirements for the degree of

Doctor of Philosophy

(Chemistry)

at the

UNIVERSITY OF WISCONSIN-MADISON

2023

Date of final examination: 9/7/2023

This dissertation is approved by the following members of the Final Oral Committee:

Robert J. Hamers, Professor, Chemistry, Materials Chemistry

Kyoung-Shin Choi, Professor, Chemistry, Materials Chemistry

Song Jin, Professor, Chemistry, Materials Chemistry

Heike Hofstetter, Staff, Chemistry, NMR Spectroscopy

Understanding the Reactivities and Mechanisms of Action of Organosilicons as Additives for Next-Generation Lithium-ion Battery Electrolytes

Louis Vincent Morris

Under the Supervision of Professor Robert J. Hamers

University of Wisconsin-Madison

Abstract

Lithium-ion batteries are the electrochemical energy storage medium which has come to dominate applications ranging from personal electronics to electric transportation. As these devices are increasingly employed in applications which demand greater power and energy density, however, battery scientists are required to adopt electrode materials which can deliver greater performance. These high-performance materials, however, are often more chemically and electrochemically reactive, hastening the decomposition reactions which already threaten cell performance, sometimes to the point that they may even compromise the cell's safety. To counter these decomposition reactions, the battery community has long utilized electrolyte additives, small molecules incorporated into the solvent in limited concentrations which improve cell performance. These molecules are commonly structural relatives of the existing alkyl carbonates which comprise most of the solvent. These kinds of additives, including fluoroethylene carbonate for instance, are often intended to be used as sacrificial additives which decompose prior to the bulk of the solvent and attempt to passivate reactive electrode surfaces before they pose a risk to the rest of the material. Such strategies have been successful when used in cells which contain conventional electrode materials, however as meeting demands for increasing capacity require the use of next generation electrode materials, these same strategies are proving less effective. A critical limiting factor to the design of new additive strategies that better suit the needs of next generation electrode materials, however, is a poor fundamental understanding of the chemical and electrochemical processes which drive solvent decomposition.

This thesis seeks to provide fundamental insights by presenting two studies which develop new methodologies for the investigation of lithium-ion battery additives. The first study presented here adapts simultaneous, in operando electrochemical quartz crystal microbalance and electrochemical impedance spectroscopy to the study of interfacial layer formation on Si anode surfaces, and then demonstrates the usefulness of the technique by determining the interfacial effects of a novel organosilicon lithium-ion battery additive which had previously been shown to suppress solvent decomposition on Si anodes via an unknown mechanism. The second study presents a method for assembling a superoxide radical scavenging activity series among structurally related additive molecules and then goes on the determine a mechanism of action by which these additives perform the scavenging reaction.

Acknowledgements

The completion of a Ph.D. represents the work of dozens of people, all working together in the pursuit of scientific and academic progress. Even though this document bears only my name, and I am the primary author of its text, none of the scientific work represented here would have been possible without my mentors, teachers, family, and friends. The thanks I owe and the gratitude I feel for all the people who have surrounded and supported me over my career so far are immeasurable, but I will do my best to distill it into a few paragraphs.

To my family, especially my mom. You have represented a constant backdrop of support for me through my entire life, and I would not have been able to make it through the instability and difficulty of graduate school without the lessons and identity that you have instilled in me. I know that you're always behind me, and I cannot wait to show you how much more I can accomplish.

To Bob, thank you so much for believing in me, even when I was losing confidence in myself. Thank you for your positivity and support of my ideas, and for always being willing to let me take a chance on the experiments that got me excited about doing science. This was far from a conventional time in the group or the department, but as your students we always knew that you were advocating as hard as you possibly could for us, and that you had our backs no matter what. I can't imagine having gone through this without your guidance and support.

To Cesar Ortiz, it isn't an exaggeration to say that you saved my project. When you joined the group and became my mentor, I was completely lost. I knew that what I was doing wasn't working, but I didn't yet have the knowledge or the voice as a scientist to fix it. You provided me with the technical knowledge that I desperately needed to get my experiments off the ground, but much more importantly than that you lifted me back into a position where I could start building out experiments on my own and then gave me the push I needed to start putting those tools to use. I can never thank you enough for all that you have done for me, your guidance helped me find the ways to push my scientific aims forward, and your encouragement (and sometimes goading, because I needed that too) pushed me to make them happen.

To Deb Gilbert, Monica Usrey, Peng Du, Sarah Guillot, and all of the friends I have made at Silatronix: nothing of the work that went into this thesis would have been possible without your support. You have enabled every single experiment I have done, every conference I have attended, and paper I have published. I could never have asked for the level of patience and care you provided for me as a student, and I can never thank you enough for the opportunities that your support has afforded me. You all have shown me that scientists are at their best when they care for one another as much as they do their research, and it has been an incredible honor to be able to work with and learn from you all.

To the Hamers Group, you all are the best possible group of human beings I could have ever hoped to work with. We have survived an onslaught of once-in-a-lifetime disasters, building closures, equipment failures, and disruptions, but through it all we supported one another with kindness, humor, and genuine love. You all helped me learn who I wanted to be as a scientist and as a young adult and gave me to courage to fully embrace a version of myself that I can be truly proud of. Thank you to the older group members who came before me, Sarah, Kelly, Liz, Austin, Zach, Jaya, Paige, Curtis, and Ben. You were amazing and inspirational mentors to me, and you showed us every day that everything we needed to succeed in graduate school was

within our grasp so long as we were able to show up for each other. To my cohort, Katie, Alicia, and Cesar Saucedo, and the cohort behind me, Connor, and Anand: I don't think any of us knew what we were signing up for when we joined this department or group at the times we did. We were knocked down so, so many times but we hung together and kept each other afloat in the offices, over zoom, and through so many movie nights and excursions. It seems both impossible and inevitable that we've all made it through, I am so proud to have gone on this journey with you.

To Trey, you have been my closest friend throughout graduate school almost from the very start. You were one of the very first people in a long time who I felt understood me and was someone I could fully relate to. I am so grateful to have been your friend and roommate for the last few years, and I can easily say that I would not have come out of this the way that I have without you. You are an amazing person and a great friend, and I am so excited to see what you will do once we're both done here, though selfishly, I hope whatever it is brings you out closer to wherever I land.

To Amanda, you have been the absolute heart of me since we met. You have stood by me through the very worst of everything that this experience brought and have never flinched from loving and supporting me in every way that you could. I truly would not have been able to do this without you, and I owe so much of what I have been able to make of my time here to you. Thank you for believing in me, and in everything that we will be able to do together.

Table of Contents

Chapter 1: Background and Introduction

1.1 Introduction to Lithium-ion Batteries

Since their introduction by Sony in 1991, lithium-ion batteries (LIBs) have become the preeminent energy storage medium for applications ranging from personal electronics to electrified vehicles.[1-3] This market dominance can be attributed to the large energy density (measured in mAh/g) of LIB systems which in turn arises from a few intrinsic properties of Li itself.[4, 5] Li is the lightest of all metals, with a molecular weight of about 7 g/mol. With a single electron in its 2s valence orbital, Li also has a stable 1+ oxidation state, meaning the Li/Li^+ redox couple can store electrons at a remarkable gravimetric efficiency of 7 g/mol of electrons.[5, 6] This mass efficiency is compounded upon Li/Li^+ having a very negative standard reduction potential of -3.04 V Li/Li^+ redox couple, meaning electrons stored in the reduction of Li^+ to Li metal also store quite a bit of free energy.[7] These two intrinsic properties allow Li to store electrons of very high energy with superb mass efficiency, lending battery systems based on this redox couple their great energy density. As with most systems which endeavor to store as much energy into as little space or mass as possible, however, stability and chemical reactivity of the system are core concerns in LIBs.[6, 8-10] Commercial LIB systems utilize organic solvents which are prone to electrochemical and chemical decomposition at both the positive and negative electrodes, and the lithium salts used as electrolytes are incredibly sensitive to water contamination.[8, 9, 11-16] If left unchecked, these decomposition processes will not only lead to the loss of cell functionality, but may also cause the generation of large quantities of flammable gases and heat, making thermal runaway and explosion real possibilities.[17-19] These risks create an acute need to control these deleterious side reactions, however efforts to do so are often frustrated by an incomplete understanding of the fundamental chemical processes taking place within operational LIBs which drive these side reactions.[20-23] To

help overcome these obstacles, this work will detail two different studies, each focused on decomposition processes native to either the cathode or anode and the ways in which solvent molecules are decomposed at or near the electrode/electrolyte interface.

In the first study, presented in chapter two, a novel adaptation of simultaneous, *in operando* electrochemical quartz crystal microbalance (EQCM) measurements together with electrochemical impedance spectroscopy (EIS) is made to study the interfacial layers generated by solvent decomposition at the surfaces of Si anodes in LIBs. This study endeavors to uncover novel insights into the dynamics of this layer formation process and the ways in which the so-called solid electrolyte interface (SEI) forms and develops its core functional properties *in operando*. A proof-of-concept study is then undertaken to demonstrate the ways in which this combined *in* operando method can unveil the mechanisms of action for additive molecules that suppress solvent decomposition, in this case using an organosilicon (OS) additive. In chapter 3, the second study in this work moves from the anode-related decomposition processes to the cathode, and to the evolution of gaseous products from solvent decomposition rather than the accumulation of solids. This study is dedicated to understanding the mechanism of action by which OS additives work to suppress gassing in batteries, particularly when those cells use nickel manganese cobalt oxide (NMC) cathodes. In pursuit of this molecular perspective, the study details a method of approach that can be used to understand the reactivities of novel additive molecules to hopefully enable the rational design of next generation additive chemistries.

The following sections of this introductory chapter will serve as additional background and motivation for the two chapters to follow, mostly to assist readers who are not already intimately familiar with the LIB literature. If you are comfortable doing so, I invite you to skip

these sections and move on to the research chapters. If you are not, I hope these sections give a bit of helpful context to the rest of this work and enable you to engage with it more readily.

1.2 Solvent Decomposition at LIB Anodes and the Solid Electrolyte Interface (SEI)

As mentioned previously, the standard reduction potential of Li is unusually negative (-3.04V vs SHE). While this is a boon in the case of energy density, it places extreme demands on the stability of the surrounding materials in the cell. In a conventional graphite LIB anode, Li^+ ions are intercalated (stored between the sheets of graphite rather than plated as a metal) during charging at potentials as low as 0.1V vs Li/Li^+.[2, 5, 6] At these potentials, several components of the electrolyte are prone to decomposition, but the solvent molecules are at particular risk as they are in direct contact with the anode.[13-16, 24, 25] The organic solvents typically used in LIBs are a blend of ethylene carbonate (a cyclic carbonate ester) with some linear carbonates such as either diethyl carbonate, dimethyl carbonate, or ethyl methyl carbonate. $LiPF_6$ is conventionally included as both the supporting electrolyte and Li^+ source at concentrations around 1 molar. Ethylene carbonate is prone to decomposition at the anode during charging at potentials as positive as 0.7 V vs Li/Li^+ and forms a variety of decomposition products including insoluble materials that precipitate onto the anode surface. These solids comprise the initial SEI layer.[24-28] As the cell is biased to even more negative potentials during charging, it will begin accumulating inorganic decomposition products including Li_2CO_3, Li_2O, and importantly LiF from secondary decomposition of the organic material and from the decomposition of the PF_6^- anion.[29, 30] Over the initial cycles in a battery's life (called formation by battery scientists) these inorganic products form a dense layer of electrically insulating (but Li^+ conductive) material on the surface. Ideally, this inorganic layer will eventually coat the anode surface thoroughly enough that solvent molecules stop reacting with the graphite anode, but Li^+ are still allowed access to

the surface for intercalation and deintercalation. At this point, the SEI is complete, and the cell is ready to be cycled stably. Because graphite anodes store Li^+ by intercalating, rather than plating it as a metal, graphite electrodes do not experience large changes in electrode volume or surface area during charge and discharge. This relative stationarity allows SEI layer formation to self-terminating on graphite anodes.[16, 29, 30] The downside of the increased cycling stability offered by this intercalation mode, however, is that it is both volume and mass inefficient. The bulk of the anode active material is essentially taken up by the host crystal lattice, and very little space is taken up by the intercalated Li.

In the case of Si anodes, however, Li is stored via the formation of a lithiated alloy phase rather than intercalating, and Si therefore has a specific capacity almost ten-times larger than that of graphite.[31] The alloying process, however efficient in storing Li, leads to massive volume expansion in the anode active material, which in turn causes the surface area of the electrode to grow during charging[31-33]. This means that at the same time as the SEI is working to passivate the electrode surface during lithiation, the surface is changing, cracking, and generating more surface area that needs to be covered, prolonging the formation process.[31-33] Upon discharge, the alloy is delithiated and shrinks, often causing the SEI to collapse and break from the anode surface, exposing the active material beneath and forcing the SEI formation process to start over. This breakdown in the anode passivation process means that Si anode cells undergo far more deleterious solvent decomposition than their graphite counterparts, and eventually cause a premature cell failure.[31-33] Eliminating or at least limiting this behavior will require us to more fully understand the underlying chemical processes that drive it. Deriving that insight is much more easily said than done, however, as even studying the SEI layer itself is fraught with technical challenges. [34-36] The SEI layer is a passivating layer formed *in situ* from decomposition

products which are themselves extremely sensitive to further decomposition. The inorganic Li salts found in the SEI are generally extremely sensitive to moisture and oxygen, the primary organic deposits are only loosely adhered to the surface and even gentle washing steps can change their composition and morphology. In general, simply disassembling the cell can introduce periods in which the electrochemical potential of the surface is disrupted.[34-36] All this means that studying the SEI using conventional *ex situ* methods cannot provide robust and accurate information about the SEI as it forms, nor necessarily as it exists in a functional cell.[34-36] Novel, *in operando* techniques must be developed which can provide as much information as possible about the status and functional properties of an active anode/electrolyte interface while in the process of cycling and formation. To this end, Chapter 2 presents the development and validation of a simultaneous, *in operando* EQCM-EIS approach to better study the dynamics of SEI layer formation on a model Si anode. We then go on to demonstrate the power of this method by studying the impact of incorporating 5 vol% of an OS additive, showing the ways in which the additive effects the interfacial and electrochemical dynamics of the anode surface and how it suppresses the formation of organic decomposition products. EQCM is an unusual technique, and for that reason I provide a brief description of the operational principle of the technique below.

1.3 The Electrochemical Quartz Crystal Microbalance as a Method for Studying LIB Interfaces

The operational principles of the quartz crystal microbalance (QCM) were originally described by Günter Saurbrey in 1959.[37] In essence, when a specifically prepared cross section of a quartz crystal is exposed to DC voltage, it will exhibit a piezoelectric behavior in which it

vibrates at a very stable and well-defined frequency. The frequency of this oscillation also varies linearly with small changes to the mass of the crystal described by the Saurbrey equation:

$$\Delta f = \frac{2{f_0}^2}{A\sqrt{\rho_q \mu_q}} \Delta m$$

where Δf and Δm are the change in oscillation frequency and change in mass respectively, f_0 is the fundamental frequency of the crystal, A is the piezoelectric area of the crystal, and ρ_q and μ_q are the density and sheer modulus of quartz respectively. The constants within the fraction on the right-hand side of the Saurbrey equation are often collected into a single proportionality constant for a given oscillator and reported as a Saurbrey constant. Modern digital electronics make it relatively easy to measure the frequency of a MHz oscillator like those used in most QCM applications to the single Hz or even 0.1 Hz level, meaning the QCM can reliably sense mass changes at the level of tens of nanograms. The EQCM system presented in Chapter 2, for instance, is a relatively mundane instrument but features noise levels as low as 1 Hz and an oscillator with a Saurbrey constant of -17.7 Hz/(cm^2ng), enabling the reliable sensation of changes in mass on the order of 1 ng. From here, the jump to the electrochemical quartz crystal microbalance involves attaching or lithographically printing a working electrode onto a quartz crystal oscillator and monitoring the changes in the crystal oscillator frequency as a function of electrochemical reaction progress on the working electrode. One of the very first adaptations of EQCM to the study of film formation in LIB systems was presented by Doran Aurbach in 1995 using noble metal electrodes.[38] This approach has since then has been expanded to include EQCM systems with dissipation monitoring (EQCM-D), model working electrode materials, and has also been combined with other *in operando* techniques to provide critical insights into the behaviors of these complex and non-stationary systems.[37-43]

1.4 Reactive Oxygen Species and Gas Formation at the Cathode

As discussed in the previous section, the reductive decomposition of solvent compounds during SEI formation can lead to the accumulation of gaseous byproducts in LIB cells, however the anode is not the only electrode interface at which gas evolution can occur. The transition metal oxides typically used as cathodes in LIBs, including $LiCoO_2$ (LCO) and the more reactive next generation $LiNi_xMn_yCo_zO_2$ (NMC) materials, are strongly alkaline and will rapidly react with any trace moisture or oxygen to form Li salts such as Li_2CO_3.[44, 45] These inorganic salts sequester Li^+, reducing cell capacity, but Li_2CO_3 in particular is implicated in a number of solvent decomposition pathways localized to the cathode.[44-47] The work detailed in chapter 3 focuses on a decomposition pathway by which Li_2CO_3 has been shown to undergo secondary oxidation and release superoxide, a radical anion with the formula $O_2^{\bullet-}$. Superoxide is a very strongly nucleophilic reactive oxygen species (ROS), and in the LIB context has been shown to decompose the cyclic carbonate solvents, such as ethylene carbonate, generating gaseous byproduct upon high temperature storage.[48-50] Previous studies have shown that fluorinated organosilicon additives incorporated at 3 vol% can reduce gassing during the high-temperature storage of NMC cathode LIBs by as much as 50%.[19] The study in chapter 3 combines these two insights--that superoxide generation at NMC cathode interfaces is a key trigger for gas generation upon storage, and that OS additives massively abate gas accumulation under those same conditions--and hypothesizes that the additives may suppress this gassing mechanism by scavenging the superoxide radical before it could attack the carbonate solvent. To demonstrate this, we undertook first a reactivity series study, demonstrating that the degree of fluorination in OS additives drives the radical scavenging ability of the additives, and then a structural determination study on the product of the scavenging reaction. Together, the insights provided by

these studies are then used propose a mechanism of action by which the additives successfully scavenge the radical anion.

1.5 References

(1) Whittingham, M. S. History, Evolution, and Future Status of Energy Storage. *Proceedings of the IEEE* **2012**, *100* (Special Centennial Issue), 1518-1534. DOI: 10.1109/jproc.2012.2190170.

(2) Brandt, K. Historical Development of Secondary Lithium Batteries. *Solid State Ionics* **1994**, *69*, 173-183.

(3) Julien, C.; Mauger, A.; Vijh, A.; Zaghib, K. Lithium Batteries. In *Lithium Batteries: Science and Technology*, Springer International Publishing, 2016; pp 29-68.

(4) Warner, J. Lithium-Ion Battery Packs for EVs. In *Lithium-Ion Batteries*, 2014; pp 127-150.

(5) Tarascon, J.-M.; Armand, M. Issuess and Challanges Facing Rechargable Lithium Batteries. *Nature* **2001**, *414*, 359-367.

(6) Xu, K. Nonaqueous Liquid Electrolytes for Lithium-Based Rechargeable Batteries. *Chemical Reviews* **2004**, *104*, 4303-4417.

(7) Liu, C.; Neale, Z. G.; Cao, G. Understanding electrochemical potentials of cathode materials in rechargeable batteries. *Materials Today* **2016**, *19* (2), 109-123. DOI: 10.1016/j.mattod.2015.10.009.

(8) Peled, E. The Electrochemical Behavior or Alkali and Alkaline Earth Metals in Nonaqueous Battery Systems-- The Solid Electrolyte Interphase Model. *Journal of The Electrochemical Society* **1979**, *126* (12), 2047-2051.

(9) Peled, E.; Menkin, S. Review—SEI: Past, Present and Future. *Journal of The Electrochemical Society* **2017**, *164* (7), A1703-A1719. DOI: 10.1149/2.1441707jes.

(10) Aurbach, D.; Talyosef, Y.; Markovsky, B.; Markevich, E.; Zinigrad, E.; Asraf, L.; Gnanaraj, J. S.; Kim, H.-J. Design of electrolyte solutions for Li and Li-ion batteries: a review. *Electrochemica Acta* **2004**, *50*, 247-254. DOI: 10.1016/j.electacta.2004.01.090.

(11) Campion, C. L.; Li, W.; Euler, W. B.; Lucht, B. L.; Ravdel, B.; DiCarlo, J. F.; Gitzendanner, R.; Abraham, K. M. Suppression of Toxic Compounds Produced in the Decomposition of Lithium-ion Battery Electrolytes. *Electrochemical and Solid State Letters* **2004**, *7* (7), A194-A197. DOI: 10.1149/1.1738551兴.

(12) Hargewoin, A. M.; Leggesse, E. G.; Jiang, J.-C.; Wang, F.-M.; Hwang, B.-J.; Lin, S. D. Comparative Study

on the Solid Electrolyte Interface Formation by the Reduction of Alkyl Carbonates in Lithium ion Battery. *Electrochemica Acta* **2014**, *136*, 274-285. DOI: 10.1016/j.electacta.2014.05.103.

(13) Koch, V. R.; Dominey, L. A.; Nanjundiah, C.; Ondrechen, M. J. The Intrinsic Anodic Stability of Several Anions Comprising Solvent Free Ionic Liquids. *Journal of The Electrochemical Society* **1996**, *143* (3), 798-803.

(14) Aurbach, D.; Gofer, Y. The Behavior of Lithium Electrodes in Mixtures of Alkyl Carbonates and Ethers. *Journal of The Electrochemical Society* **1991**, *138* (12), 3529-3536.

(15) Aurbach, D.; Gofer, Y.; Ben-Zion, M.; Aped, P. The behavior of lithium electrodes in propylene and ethylene carbonate: the major factors that influence lithium cycling efficiency. *Journal of Electroanalytical Chemistry* **1992**, *339*, 451-471.

(16) Zhang, X.; Kostechi, R.; Richardson, T. J.; Pugh, J. K.; Ross Jr., P. N. Electrochemical and Infrared Studies of the Reduction of Organic Carbonates. *Journal of The Electrochemical Society* **2001**, *148* (12), A1341-A1345. DOI: 10.1149/1.1415547.

(17) Lee, K. H.; Song, E. H.; Lee, J. Y.; Jung, B. H.; Lim, H. S. Mechanism of gas build-up in a Li-ion cell at elevated temperature. *Journal of Power Sources* **2004**, *132* (1-2), 201-205. DOI: 10.1016/j.jpowsour.2004.01.042.

(18) Mao, C.; Ruther, R. E.; Geng, L.; Li, Z.; Leonard, D. N.; Meyer, H. M., 3rd; Sacci, R. L.; Wood, D. L., 3rd. Evaluation of Gas Formation and Consumption Driven by Crossover Effect in High-Voltage Lithium-Ion Batteries with Ni-Rich NMC Cathodes. *ACS Appl Mater Interfaces* **2019**, *11* (46), 43235-43243. DOI: 10.1021/acsami.9b15916 From NLM PubMed-not-MEDLINE.

(19) Guillot, S. L.; Usrey, M. L.; Peña-Hueso, A.; Kerber, B. M.; Zhou, L.; Du, P.; Johnson, T. Reduced Gassing In Lithium-Ion Batteries With Organosilicon Additives. *Journal of The Electrochemical Society* **2021**, *168* (3). DOI: 10.1149/1945-7111/abed25.

(20) Ein-Eli, Y.; Thomas, S. R.; Chadha, R.; Blakley, T. J.; Koch, V. R. Li-lon Battery Electrolyte Formulated for Low Temperature Applications. *Journal of The Electrochemical Society* **1997**, *144* (3), 823-829.

(21) Aurbach, D.; Ein-Eli, Y.; Markovsky, B.; Zaban, A.; Luski, S.; Carmeli, Y.; Yamin, H. The Study of Electrolyte Solutions Based on Ethylene and Diethyl Carbonates for Rechargeable Li Batteries II. Graphite Electrodes. *Journal of The Electrochemical Society* **1995**, *142* (9), 2882-2890.

(22) Aurbach, D.; Zaban, A.; Schechter, A.; Ein-Eli, Y.; Zinigrad, E.; Markovsky, B. The Study of Electrolyte Solutions Based on Ethylene and Diethyl Carbonates for Rechargeable Li Batteries 1 Li metal Electrodes. *Journal of The Electrochemical Society* **1995**, *142* (9), 2873-2882.

(23) Endo, E.; Ata, M.; Tanaka, K.; Sekai, K. Electron Spin Resonance Siudy of the Electrochemical Reduction of Electrolyte Solutions for Li Secondary Batteries. *Journal of The Electrochemical Society* **1998**, *145* (11), 3757-3764.

(24) Wang, Y.; Nakamura, S.; Ue, M.; Balbuena, P. B. Theoretical Studies To Understand Surface Chemistry on Carbon anodes for Lithium-Ion Batteries: Reduction Mechanisms of Ethylene Carbonate. *Journal of the American Chemical Society* **2001**, *123* (47), 11708-11718.

(25) Yanase, S.; Oi, T. Solvation of Lithium Ion in Organic Electrolyte Solutions and Its Isotopie Reduced Partition Function Ratios Studied byab initioMolecular Orbital Method. *Journal of Nuclear Science and Technology* **2002**, *39* (10), 1060-1064. DOI: 10.1080/18811248.2002.9715294.

(26) Fong, R.; von Sacken, U.; Dahn, J. R. Studies of Lithium Intercalation into Carbons Using Nonaqueous Electrochemical Cells. *Journal of The Electrochemical Society* **1990**, *137* (7), 2009-2013.

(27) Arakawa, M.; Yamaki, J.-I. The Cathodic Decomposition of Propylene Carbonate in Lithium Batteries. *Journal of Electroanalytical Chemistry* **1987**, *219*, 273-280.

(28) Shu, Z. X.; McMillan, R. S.; Murray, J. J. Electrochemical Intercalation of Lithium into Graphite. *Journal of The Electrochemical Society* **1993**, *140* (4), 922-927.

(29) Naji, N.; Ghanbaja, J.; Humbert, B.; Willmann, P.; Billaud, D. Electroreduction of graphite in LiClO4-
ethylene carbonate electrolyte. Characterization of the passivating layer by transmission electron microscopy and Fourier-transform infrared spectroscopy. *Journal of Power Sources* **1996**, *63*, 33-39.

(30) Zhang, S.; Ding, M. S.; Xu, K.; Allen, J.; Jow, T. R. Understanding Solid Electrolyte Interface Film Formation on Graphite Electrodes. *Journal of The Electrochemical Society* **2001**, *4* (12), A206-A208. DOI: 10.1149/1.1414946.

(31) Jin, Y.; Zhu, B.; Lu, Z.; Liu, N.; Zhu, J. Challenges and Recent Progress in the Development of Si Anodes for Lithium-Ion Battery. *Advanced Energy Materials* **2017**, *7* (23). DOI: 10.1002/aenm.201700715.

(32) Zuo, X.; Zhu, J.; Müller-Buschbaum, P.; Cheng, Y.-J. Silicon based lithium-ion battery anodes: A chronicle perspective review. *Nano Energy* **2017**, *31*, 113-143. DOI: 10.1016/j.nanoen.2016.11.013.

(33) Wu, Q.; Shi, B.; Bareno, J.; Liu, Y.; Maroni, V. A.; Zhai, D.; Dees, D. W.; Lu, W. Investigations of Si Thin Films as Anode of Lithium-Ion Batteries. *ACS Appl Mater Interfaces* **2018**, *10* (4), 3487-3494. DOI: 10.1021/acsami.7b13980 From NLM PubMed-not-MEDLINE.

(34) Saqib, N.; Ganim, C. M.; Shelton, A. E.; Porter, J. M. On the Decomposition of Carbonate-Based Lithium-Ion Battery Electrolytes Studied Using Operando Infrared Spectroscopy. *Journal of The Electrochemical Society* **2018**, *165* (16), A4051-A4057. DOI: 10.1149/2.1051816jes.

(35) Kumar, R.; Tokranov, A.; Sheldon, B. W.; Xiao, X.; Huang, Z.; Li, C.; Mueller, T. In Situ and Operando Investigations of Failure Mechanisms of the Solid Electrolyte Interphase on Silicon Electrodes. *ACS Energy Letters* **2016**, *1* (4), 689-697. DOI: 10.1021/acsenergylett.6b00284.

(36) Shi, F.; Ross, P. N.; Somorjai, G. A.; Komvopoulos, K. The Chemistry of Electrolyte Reduction on Silicon Electrodes Revealed by in Situ ATR-FTIR Spectroscopy. *The Journal of Physical Chemistry C* **2017**, *121* (27), 14476-14483. DOI: 10.1021/acs.jpcc.7b04132.

(37) Saurbrey, G. Verwendung von Schwingquarzen zur Wagung diinner Schichten und zur Mikrowagung. *Zeitschrift fur Physik* **1959**, (155), 206-222.

(38) Aurbach, D.; Zaban, A. The application of EQCM to the study of the electrochemical behavior of propylene carbonate solutions. *Journal of Electroanalytical Chemistry* **1995**, *393*, 43-53.

(39) Dargel, V.; Shpigel, N.; Sigalov, S.; Nayak, P.; Levi, M. D.; Daikhin, L.; Aurbach, D. In situ real-time gravimetric and viscoelastic probing of surface films formation on lithium batteries electrodes. *Nat Commun* **2017**, *8* (1), 1389. DOI: 10.1038/s41467-017-01722-x From NLM PubMed-not-MEDLINE.

(40) Kitz, P. G.; Lacey, M. J.; Novak, P.; Berg, E. J. Operando EQCM-D with Simultaneous in Situ EIS: New Insights into Interphase Formation in Li Ion Batteries. *Anal Chem* **2019**, *91* (3), 2296-2303. DOI: 10.1021/acs.analchem.8b04924 From NLM PubMed-not-MEDLINE.

(41) Hubaud, A. A.; Yang, Z.; Schroeder, D. J.; Dogan, F.; Trahey, L.; Vaughey, J. T. Interfacial study of the role of SiO2 on Si anodes using electrochemical quartz crystal microbalance. *Journal of Power Sources* **2015**, *282*, 639-644. DOI: 10.1016/j.jpowsour.2015.02.006.

(42) Nishizawa, M.; Uchiyama, T.; Itoh, T.; Abe, T.; Uchida, I. Electrochemical Quartz Crystal Microbalance for Insertion/Extraction of Lithium in Spinel LiMn2O4 Thin Films. *Langmuir* **1999**, (15), 4949-4951.

(43) Tavassol, H.; Buthker, J. W.; Ferguson, G. A.; Curtiss, L. A.; Gewirth, A. A. Solvent Oligomerization during SEI Formation on Model Systems for Li-Ion Battery Anodes. *Journal of The Electrochemical Society* **2012**, *159* (6), A730-A738. DOI: 10.1149/2.067206jes.

(44) Kaufman, L. A.; McCloskey, B. D. Surface Lithium Carbonate Influences Electrolyte Degradation via Reactive Oxygen Attack in Lithium-Excess Cathode Materials. *Chemistry of Materials* **2021**, *33* (11), 4170-4176. DOI: 10.1021/acs.chemmater.1c00935.

(45) Park, C.; Lee, E.; Kim, S. H.; Han, J.-G.; Hwang, C.; Joo, S. H.; Baek, K.; Kang, S. J.; Kwak, S. K.; Song, H.-K.; et al. Malonic-acid-functionalized fullerene enables the interfacial stabilization of Ni-rich cathodes in lithium-ion batteries. *Journal of Power Sources* **2022**, *521*. DOI: 10.1016/j.jpowsour.2021.230923.

(46) Strehle, B.; Kleiner, K.; Jung, R.; Chesneau, F.; Mendez, M.; Gasteiger, H. A.; Piana, M. The Role of Oxygen Release from Li- and Mn-Rich Layered Oxides during the First Cycles Investigated by On-Line Electrochemical Mass Spectrometry. *Journal of The Electrochemical Society* **2017**, *164* (2), A400-A406. DOI: 10.1149/2.1001702jes.

(47) Teufl, T.; Strehle, B.; Müller, P.; Gasteiger, H. A.; Mendez, M. A. Oxygen Release and Surface Degradation of Li- and Mn-Rich Layered Oxides in Variation of the Li2MnO3Content. *Journal of The Electrochemical Society* **2018**, *165* (11), A2718-A2731. DOI: 10.1149/2.0691811jes.

(48) Teufl, T.; Pritzl, D.; Krieg, P.; Strehle, B.; Mendez, M. A.; Gasteiger, H. A. Operating EC-based Electrolytes with Li- and Mn-Rich NCMs: The Role of O2-Release on the Choice of the Cyclic Carbonate. *Journal of The Electrochemical Society* **2020**, *167* (11). DOI: 10.1149/1945-7111/ab9e7f.

(49) Yabuuchi, N.; Yoshii, K.; Myung, S. T.; Nakai, I.; Komaba, S. Detailed studies of a high-capacity electrode material for rechargeable batteries, Li2MnO3-LiCo(1/3)Ni(1/3)Mn(1/3)O2. *J Am Chem Soc* **2011**, *133* (12), 4404-4419. DOI: 10.1021/ja108588y From NLM PubMed-not-MEDLINE.

(50) Castel, E.; Berg, E. J.; El Kazzi, M.; Novák, P.; Villevieille, C. Differential Electrochemical Mass Spectrometry Study of the Interface of xLi2MnO3·(1–x)LiMO2 (M = Ni, Co, and Mn) Material as a Positive Electrode in Li-Ion Batteries. *Chemistry of Materials* **2014**, *26* (17), 5051-5057. DOI: 10.1021/cm502201z.

Chapter 2: Adapting Simultaneous *in Operando* Electrochemical Quartz Crystal Microbalance (EQCM) and Electrochemical Impedance Spectroscopy (EIS) to Studies of SEI Layer Formation on Amorphous Silicon Anodes

These materials presented in this chapter were previously published as a research article under the same title, and can be found in that format using the citation:

L. V. Morris *et al* 2023 *J. Electrochem. Soc.* **170** 050503

DOI 10.1149/1945-7111/accf3d

2.1 Abstract

Lithium-ion Batteries (LIBs) are the electrochemical energy storage technology of choice for an incredible range of technologies. The application of these batteries has, however, been limited by poor energy density, which is due to the low theoretical energy density of the graphite anodes that are standard in the field. Si has long been targeted as a higher energy density anode material, however uncontrolled electrolyte decomposition on its surface has caused poor cycle life and low columbic efficiencies in Si-containing cells. In this work, a new class of organosilicon (OS) additives were introduced to the Si anode literature and their effect on the first-cycle electrochemistry of model anode surfaces was explored using *in operando* electrochemical quartz crystal microbalance (EQCM) and electrochemical impedance spectroscopy (EIS). X-ray photoelectron spectroscopy (XPS) was also used to investigate the differences in composition of solid electrolyte interface (SEI) layers formed in the presence and absence of additive. EQCM-EIS experiments demonstrated an increase in OS-treated cell impedance early in the cycle, which lead to the suppression of early electrolyte decomposition on the model anode surface. XPS revealed that OS-treated cells create thinner SEI layers that were richer in LiF and contained less organic material than cells without OS.

2.2 Introduction

To meet the increasing demands on the energy density of lithium-ion batteries (LIBs) batteries, the energy storage community has identified silicon as a next generation anode

material, possessing a theoretical energy density an order of magnitude greater than the graphite anodes that are traditionally employed[1]. A major concern barring the deployment of Si anodes, however, is the stability of the passivating solid electrolyte interface layer (SEI) that forms on LIB anodes[1-3].

The SEI layer formed on LIB anodes has been studied extensively, primarily using *ex-situ* techniques such as XPS, SEM, and FTIR to elucidate the chemical structure and function of the deposited material[4-8]. Due to the *ex-situ* nature of these techniques, especially in the case of electron emission techniques that require high vacuum, samples must undergo substantial preparation. Preparatory washing, drying, sample transfer between instruments can introduce significant changes to the SEI layer morphology and composition, and make elucidation of the functional structure and composition of the layer in operational batteries much more difficult[9-12]. Therefore, *in situ* techniques are necessary to determine how the SEI layer is formed and how it functions during battery cycling.

In this work, we have adapted a pair of *in operando* techniques, electrochemical quartz crystal microbalance (EQCM) and electrical impedance spectroscopy (EIS), to work in concert during the initial electrochemical cycling of a model Si anode. These complementary techniques offer a unique perspective on SEI layer formation. EQCM allows the accumulation of material on the anode surface to be tracked gravimetrically, showing the progression of SEI layer development and anode lithiation[13-18] while EIS provides insight into the electrochemical qualities of the layer at each stage of its development[19-22]. We further apply these combined *in operando* methods to study the impact of an organosilicon electrolyte (OS) additive on the initial electrochemical cycling and SEI layer formation and the roots of its observed benefits to Si

anode cycling stability. This combination provides new insight into the electrochemical processes that drive SEI layer formation.

2.3 Experimental

Electrolyte Formulation

The electrolyte blends used in this study were 1:1:1 blends (by volume) of ethylene carbonate, dimethyl carbonate, and diethyl carbonate, with a 1M concentration of $LiPF_6$. The OS additive-treated electrolyte blend was identical except for the addition of 5 volume percent of the additive compound.

EQCM-EIS Electrode Fabrication

EQCM quartz crystal oscillators, 1 inch diameter, were obtained from Inficon with a Au/Cr electrode surface (product number QM1001). These oscillators were then coated on their working side first in 100nm of Ti metal and then in 100nm of amorphous Si (both obtained from Kurt J. Lesker) using electron-beam metal evaporation. SEM images of the finished surface of prepared electrode are included in Figure S1 in the supplementary information at the end of this chapter.

EQCM-EIS Cell Construction

EQCM-EIS experiments were conducted using a custom machined cell cap developed to enable air-free cycling of the model electrodes which interfacing with the SRSQCM200 quartz crystal microbalance instrument. This cell cap was constructed of PEEK with a stainless-steel plug press-fitted into it to create an air-tight electrical contact into the cell interior, into which Li foil was pressed to create Li counter/reference electrode to facilitate electrochemical cycling and

analysis in a two-electrode geometry. A schematic representation of the cell cap with additional information about cell geometry is provided in Figure S2 of the supplementary information.

Cycling of Model Cells

Coated oscillators were installed into the sensor head of a Stanford Research Systems QCM200 quartz crystal microbalance. Inside of an Ar filled glovebox (LC Technology Solutions, O_2<1ppm H_2O<1ppm), the sensor head was then fitted with a custom-built electrochemical cell assembly constructed by the authors, which created an air-tight thin layer electrochemical cell volume directly on top of the sensor head such that a Li metal counter/reference electrode was suspended <1mm above the Si working electrode surface. This electrochemical cell was then filled with electrolyte solution, and the sensor head and counter reference electrodes were attached to the appropriate leads of a potentiostat (Gamry Instruments Interface 1010E) that was co-located within the glovebox. To characterize the electrochemical properties, we used a cyclic potential sweep that was divided into 8 segments: 1.5-1.0, 1.0-0.7, 0.7-0.5, 0.5-0.25, 0.25-0.05, 0.0-0.4, 0.4-0.8, and 0.8-1.5 V vs Li/Li^+. Within in each segment the potential was swept at a rate of 0.1mV/s. At the end of each segment, we performed a potentiostatic EIS measurement with the potential fixed at the last value from the just-completed segment. EIS measurements utilized a ±10 mV AC oscillation with 5 frequency points per decade between 1 MHz and 0.1 Hz. Throughout the electrochemical cycling, the oscillating frequency of the modified quartz crystal was measured by the SRS QCM200 module and recorded using custom LabView software. The change in the mass of the electrode was calculated utilizing the Saurbrey constant for the quartz crystal oscillators, which for the crystals used here was -56.6 $Hz*cm^2/\mu g$ as supplied by the manufacturer.

EIS Data Processing

EIS data was collected during the potentiostatic cycling of the EQCM electrodes and processed using the Impedance.py Python package[23]. Nyquist plots displaying both the raw impedance data and the fitting results produced by Impedancy.py are provided in Figure S3 and S4.

X-ray Photoelectron Spectroscopy

Samples for XPS were fabricated by depositing 100nm of amorphous Si onto Ti substrates (0.5 mm thick) using electron-beam evaporation; these samples were then cut into 1cm square electrodes. These electrodes were then assembled into half-cells using 2032 Li-ion battery coin cell casings (MTI) using a glass fiber separator (Millipore Sigma Grade AP40 Glass Filter) and a Li metal counter-electrode. These half cells were then flooded with 200µL of electrolyte and the casings were crimped closed using a Hohsen coin cell crimper (Hohsen Scientific). Samples were then cycled via cyclic voltammetry from 1.5-0.05 V vs Li/Li^+ at 0.1 mV/s. Coin cells were then disassembled in an argon-filled glovebox, and Si electrodes were washed in 100 µL of diethyl carbonate two times before being dried under vacuum at room temperature. After drying, electrodes were placed in a vacuum-transfer module (Thermo Scientific) and transported to the XPS instrument under vacuum. The vacuum-transfer module was only opened within the evacuated antechamber of the XPS instrument, ensuring that the surface of the Si anodes was not disturbed by atmospheric water or oxygen.

XPS spectra were collected on a Thermo Scientific K-Alpha XPS instrument using a monochromatic Al K_α X-ray source and a 200 µm spot size. Emitted photoelectrons were analyzed using a 180º hemispherical analyzer with a 128-channel detector and an analyzer pass energy of 280 eV in survey spectra and 50 eV in multiplex spectra. All XPS data were processed using CasaXPS[24]. XPS data analysis in this work utilized a Shirley background and a GL(30)

mixed Gaussian-Lorentzian peak shape was used to model the contributions of unique chemical states.

Percent relative elemental abundances were calculated from XPS survey spectra with appropriate backgrounds fitted to the major emission features of the key elements in question. First, the areas enclosed between the collected signal curve and its background A_i were tabulated for each element *i*, and then each individual area was divided by a sensitivity factor SF_i, normalizing its electron yield in counts to another element (in this case carbon). The sensitivity factor adjusted areas are then each divided by the sum of all adjusted areas and multiplied by 100 to yield a percent relative abundance, as summarized in equation 1:

$$\%\ Rel\ Abundance = \frac{\frac{A_i}{SF_i}}{\sum_0^n \frac{A_i}{SF_i}} * 100$$

2.4 Results and Discussion

In our experiments, we simultaneously track the current and the change in mass as the cell is cycled, in addition to the single EIS measurement at the end of each segment. Figure 1a shows an 8-segment voltammogram cycle starting at a potential of 1.5 V vs Li/Li^+ and scanning down to 0.05V vs Li/Li^+, and then returning to 1.5 V while Figure 1b shows the corresponding EQCM data measured during this voltametric cycle. Each of linear sweeps comprising the complete potentiostatic cycle is color-coded in Figure 1a and Figure 1b to distinguish them from one another and to facilitate correlating each segment of the voltammogram (1a) to its corresponding section of the massogram (1b). The color coding is reinforced by sequentially assigning the first eight letters of the Greek alphabet to the corresponding segment. Figure 1a exhibits a peak at 0.65V vs Li/Li^+ during the cathodic scan, which spans both segments b and g. A comparison of

Figure 1a and Figure 1b shows that the peak at 0.65 V in Figure 1a corresponds to a large increase in electrode mass. At more negative potentials we observe two reductive (and thus downward pointing) peaks at 0.25V and 0.05V vs Li/Li^+ in Figure 1a (segments δ and ε again correlating to an increase in the electrode mass in Figure 1b before the negative sweep ends. The reverse scan shows the current reversing sign near 0.4V (segment ζ) and reaching a local maximum near 0.55.V (segment η). Figure 1b shows that the anodic current in segments ζ and η is correlated with a *decrease* in mass. As noted earlier, the breaks in both the voltammogram and mass accumulation curve correspond to the potentials at which *in operando* EIS measurements were performed. The discontinuities in the observed current are generated because the applied voltage at the end of each sweep is maintained during the impedance measurement, during which time the observed current decayed slightly.

In order to validate the methods we use here, we first investigated the use of these correlated approaches to study the behavior of Si anodes in a conventional electrolyte blend using 1:1:1 ethylene carbonate, dimethyl carbonate, and diethyl carbonate and 1M $LiPF_6$. Figure 1 shows the correlation between electrochemical activity and electrode mass throughout the first potentiostatic charge and discharge cycle of a model Si anode. The first cycle of any LIB anode is expected to include both reversible lithiation/delithiation and irreversible electrolyte decomposition resulting in SEI layer formation. The principal advantage of potentiostatic cycling is that, within reason, these processes can be resolved from one another in time. This temporal resolution allows us to study the effects of the OS additive on both SEI layer formation processes (i.e., electrolyte decomposition) and anode lithiation and delithiation separately. When this electrochemical information is combined with the gravimetric information provided in the massogram in Figure 1b, it is possible to tell which processes that we have resolved and

observed in the voltammetry are responsible for the formation of surface layers on the electrode surface or the addition or removal of lithium from the anode.

For Si anodes, lithiation of vacuum-deposited films is not expected at potentials above 0.1-0.3V vs Li/Li^{+}[25-29]. Consequently, we attribute all features in segments α, β, γ, and δ to reductive decomposition of the electrolyte in accordance with previous studies[30]. In these regions, the most apparent feature is the large reduction event that peaks near 0.65V and the associated mass accumulation events in segments β and γ. The large current and associated mass change below ~0.3 V are due primarily to lithium intercalation.

Prior studies have shown that delithiation of Si anodes typically occurs at 0.4-0.5V vs Li/Li^{+}[12,26, 27, 29], but due to lithium trapping and dynamics unique to the film construction it can continue to much higher potentials[31-35]. In Figure 1a and 1b, we attribute the oxidative current and mass loss at 0.4 -0.8 V in segments η and θ to the delithiation of the silicon anode.

The experiments above demonstrate that the correlated methods used here can identify the major chemical and physical processes occurring at Si anodes in a simple carbonate-based electrolyte. With these methodologies validated, we proceeded to probe the influence of a model organosilicon-based additive that has been shown to be effective in improving cell performance[36]. For these studies, we used an organosilicon electrolyte additive whose structure is presented in Figure 3 below. We will refer to this compound as “OS” or “OS additive”, and in all studies will have added 5% by volume of this additive to the carbonate electrolyte blend used for the control studies in Figure 1.

Figure 2 shows EQCM plots similar to those in Figure 1 for a cell containing 5% by volume OS additive in green and without OS additive in black overlaid. The data for the control electrolyte

in black is identical to that shown in Figure 1, but Fig. 2 overlays the results from cells prepared with the addition of OS electrolyte (in green) to facilitate a direct comparison between treated and untreated electrolyte. The Greek letters assigned to each segment are carried forward from Figure 1 to assist in correlating sections of the CV and massogram in time. In Figure 2a, the additive treated cell (green) passes less current in segments β and γ compared to the control sample (black) without additive. This reduced electrochemical activity in the presence of OS is correlated with a smaller accumulation of mass on the model anode surface than was experienced by the control cell as seen in Figure 2b.

While the OS additive decreases the observed current and associated mass changes during early stages of the initial charge cycle, this trend is reversed in segments δ and ε, where the cell with OS shows more reductive current and greater mass changes than the control cell. During the return (anodic) sweep, in segment ζ the cell with OS additive shows a reversal of current to positive (cathodic) values at a potential of 0.2V, while current reversal in the control cell requires a more positive potential. This increased electrochemical activity are reflected in the earlier and more intense onset of mass loss observed in the additive treated sample in Figure 2b. In segment η, the cell with OS additive displays substantially more oxidative current than the control cell, correlated again with greater and faster mass loss in segment η of the massogram.

To understand the chemical origins of the above observations, we note that electrochemical activity in segments β and γ, between 1.0 and 0.4V vs Li/Li^+ in the initial (cathodic) sweep, is primarily due to the reductive decomposition of the electrolyte, and the associated mass increase due to the associated formation of insoluble reaction products that form on the Si anode. The reduced electrochemical activity and mass accumulation in the additive-treated cell at these potentials show that the OS additive suppresses reductive electrolyte decomposition and SEI

layer formation. As lithiation of the Si anode begins in segment δ, the higher current and greater mass change observed in the OS-containing cell demonstrate that the thinner SEI layer formed in the prior segments leads to more facile lithium intercalation. Correspondingly, during the cathodic sweep the reversal of current at more negative potentials and the greater current and mass change associated with delithiation in the cells containing OS all point to more facile lithiation and delithiation of the model anode.

Figure 4 shows the XPS elemental abundances of several key elements at electrodes cycled with and without OS additive. The first differences of note are that introduction of OS decreases the relative abundance of carbon and oxygen, with nominal decreases in nitrogen and phosphorus as well. Conversely, introduction of the OS additive increases the abundance of Li and F. The decreased abundance of C and O suggests that the electrode cycled in the presence of additive accumulated less organic material from the decomposition of solvent molecules. This interpretation is consistent with the EQCM data shown in Figure 2, which also suggests that the decomposition of organic solvent species has been suppressed. The increased relative abundances of lithium and fluorine indicate that the surface layer formed in the presence of the additive could be richer in inorganic SEI layer components. To better understand the identity of the additional fluorine containing material, we performed high-resolution scans in the F1s region and used peak fitting analysis to divide the F1s signal into contributions made by LiF and those made by other F-containing species. This analysis showed that the increase in F signal was principally due to an increase in fractional abundance of LiF at the OS-treated electrode surface, while the fractional abundance of species other than LiF was constant between the experimental additive containing cell and the control. LiF has been identified previously as a very beneficial component to the SEI layer[37,38] and LiF-enriched surface layers have been reported in studies of

other additives known to benefit Si anode LIB chemistries such as fluoroethylene carbonate (FEC).[37],[4],[38]. Although LiF is electrically insulating, it allows relatively easy passage of Li^+ ions, passivating the anode surface without impeding cycling, and the increased LiF abundance we observe on the OS-treated anode surface suggests that the OS could be providing a similar benefit to FEC. We further note that a previous investigation using this same OS additive showed that it persists through extended cycling in active cells[36]; while FEC, in contrast, acts as a sacrificial additive[30, 37, 38]. The persistence of the OS additive throughout cycling coupled with the above observation that its inclusion in the battery electrolyte results in effects similar to those attributed to sacrificial additives like FEC could mean that the organosilicon additive contributes to the formation of an effective SEI layer on Si anodes by a mechanism that is distinct from that observed with other common additives.

In order to enable the comparison of charge-transfer resistance of the cell at each point in the cycle, we used equivalent-circuit modeling to analyze the impedance spectra collected during the EQCM-EIS measuremens. This analysis initially used a more complicated equivalent-citcuit model circuit containing two RC elements[22, 39-42]. However, when that model was applied to the vast majority of the EIS spectra, the resulting fits contained values whose uncertainties were larger than the projected values themselves. This indicated that the fits could assign a value of zero to those parameters within statistical certainty, and that those parameters were not necessary to fit the data set. Taking this into consideration, we removed one RC element from the model circuit to create the model circuit shown in 5a. This model succesfully fit all EIS spectra except those collected at the end of segment γ. In the case of those specta, the equivalent circuit shown in Figure 5b was used.

During potentiostatic cycling, major electron transfer processes can be resolved from one another as a function of potential[12, 26, 29]. For the purposes of the present analysis, electron transfer from the reductive decomposition of solvent components and electron transfer from lithium alloying are resolved in all impedance spectra except those taken at the end of segment γ. As a result, for all spectra except those the single-RC element model circuit in (5a) provided high quality data fitting with a minimum number of parameters. For the spectra recorded at the end of segment γ, the two RC element model circuit in (5b) was necessary to achieve suitable fits.

Figure 6 plots the charge-transfer resistance values calculated using equivalent-circuit modeling of the impedance spectra collected during the EQCM-EIS cycling shown in Figure 2. At the end of each linear sweep segment of the voltammogram, the potential sweep was paused and a potentiostatic EIS spectrum was collected of the cell at the applied potential. Those EIS spectra were then fit to an equivalent model circuit from Figure 5. The spectra collected during segment γ was analyzed using the two electron-transfer model circuit (5b), produced two different charge-transfer resistances, which are labelled γ R1 and γ R2.

The observed resistance values followed a clear trend through the potentiostatic cycle. At the beginning of the cycle, resistance values from the relatively pristine surface were high and decreased throughout the charging sweep until they reached a minimum at the end of the charging sweep. As the cells began to discharge, impedance values rose again through the remainder of the sweep. In the presence of the OS additive, charge-transfer resistances were higher at the end of segments α and β. The cell moved through a transitional period in segment γ as two electron transfer processes appeared in the impedance spectra collected at the end of segment γ. One of the observed parameters, γ R2, followed the trend established in segments α and β, yielding a larger value in presence of OS electrolyte. In contrast, γ R1 was lower in the

presence of OS additive. In segments δ and ε, anode lithiation became the dominant electron transfer process on the anode surface and charge-transfer resistances are lower in the presence of the additive at the end of those segments. The trend of smaller charge-transfer resistance in the presence of OS held for the entirety of the discharging sweep through segments ζ, η, and θ.

The combination of real-time gravimetric and electrochemical analysis techniques, as shown in in this work, provide a uniquely powerful level of insight into the SEI-layer formation process. The SEI layer formation process is notoriously difficult to interrogate using traditional *ex-situ* techniques due to the nanometer-scale depth of the layer and its components instability even within the cell context, let alone after disassembly. For these reasons, surface sensitive, i*n-operando* methodologies are essential tool to further develop our understanding of the SEI layer formation process and of the chemical and electrochemical mechanisms underpinning its behavior. Simultaneous EQCM-EIS is a perfectly suited technique to this purpose, and this work demonstrates the illuminating power that it can bring to explorations of not only specific anode chemistries but also to the effects of small molecule electrolyte additives.

Our data point to a more detailed understanding of how the presence of this model OS additive impacts the electrochemical performance during charging. During the initial phases (α, β, and γ), the dominant charge-transfer process is expected to be electrolyte decomposition [10, 12, 25]. In these segments, EIS analysis shows that the presence of the OS species substantially increases the charge-transfer resistance at the electrode-electrolyte interface. This increase has beneficial effects by decreasing the cathodic current and decreasing the accumulation of mass associated with SEI layer formation in the OS-containing cells those times. As the cell advances toward more cathodic potentials and begins to lithiate (segments δ and ε), the additive-treated cell exhibits less interfacial resistance compared with cells not containing OS. We attribute

improved conductivity to the fact that the SEI layer formed in the presence of the additive contains less organic material and is enriched in LiF, leading to higher ionic conductivity. After reversing the scan direction, the model anode in OS-containing electrolyte experiences less resistance to delithiation and achieves greater cathodic currents in regions ζ and η compared to a control electrolyte for the same reasons. Overall, the incorporation of the OS additive into the electrolyte mixture has the net effect of forming an SEI layer that is thinner, enriched in LiF, and exhibits improved electrical properties compared to electrolytes without the OS additive.

2.5 Conclusions

The use of electrochemical measurements combined with simultaneous QCM measurements provide new insights into the formation and electrical properties of SEI layers and the impact of additives on SEI layer properties. The presence of a model organosilicon-based additive suppressed organic solvent reduction early (>0.5V vs Li/Li^+) in the first potentiostatic charge of amorphous silicon model anodes as indicated by EQCM cycling. Later in the first potentiostatic cycle, the model anodes cycled in the presence of OS lithiated and delithiated more readily than those cycled without additive. After cycling, XPS analysis showed that in addition to having less mass, SEI layers formed in the presence of additive contain less organic material and more LiF than those formed in the control blend, corroborating the observed suppression of solvent molecule decomposition suggested by EQCM. EIS analysis confirmed that charge transfer resistances related to solvent decomposition were higher and that charge transfer resistances related to lithiation and delithiation were lower in the presence of the additive. Taken as a whole, these observations suggest that the organosilicon additive improved the first potentiostatic cycling performance of model Si anodes by suppressing the deleterious reductive decomposition of organic solvent species early in the charging sweep, leading to the formation of

a thinner, more ion conductive SEI layer. These changes to the SEI layer formation process suggest that addition of the organosilicon compound to Si-containing anode cell formulations may improve first cycle columbic efficiency and improve cell lifetime in next-generation lithium-ion devices.

2.6 Acknowledgments

This material is based upon work supported by the Office of Naval Research under Contract No. N00014-21-C-1075. Any opinions, findings and conclusions or recommendations expressed in this material are those of the Author(s) and do not necessarily reflect the views of the Office of Naval Research.

2.7 Figures

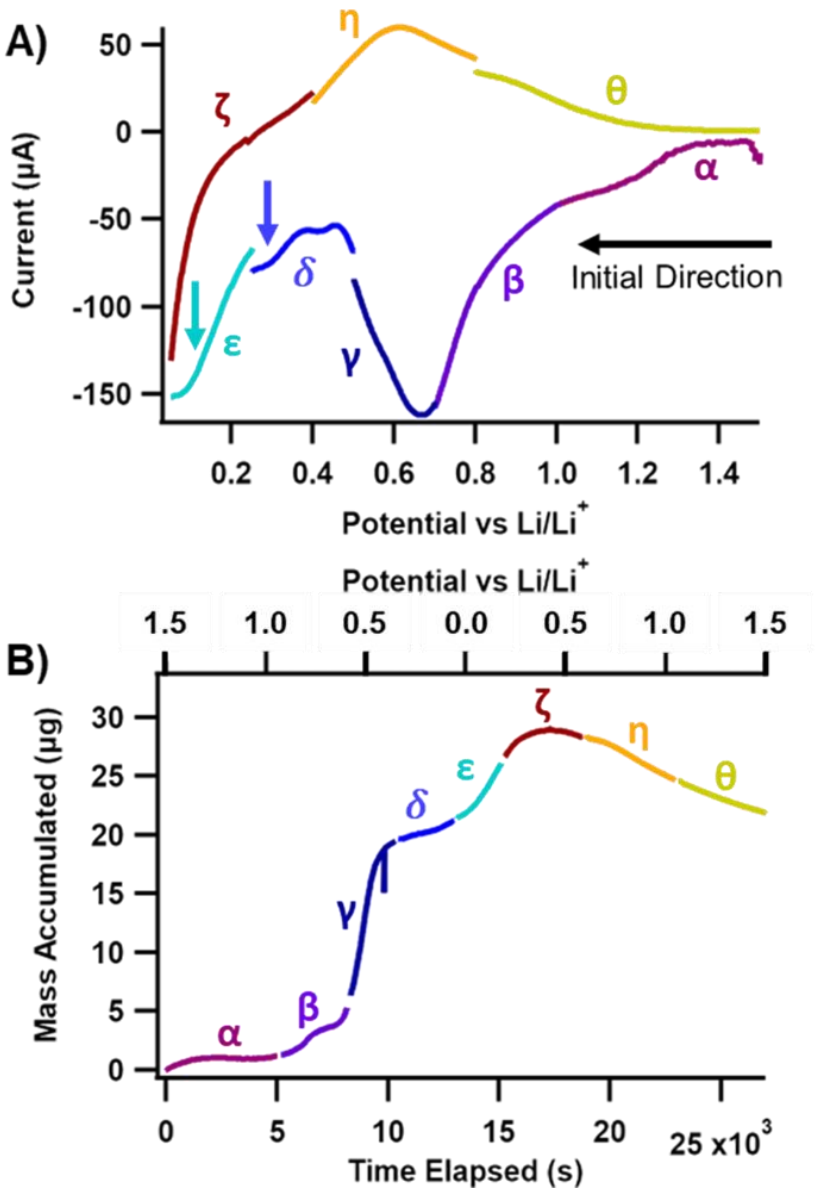

Figure 1. Complete potentiostatic cycle of model Si anode in the *in operando* EQCM-EIS cell (A) and recorded mass accumulation curve of the model anode as a function of time (B). The plots are color coded to show which segments were recorded simultaneously. The color coding is reinforced by Greek letters assigned to each segment. Arrows are included to indicate the initial scan direction (black) as well as the observed reduction events at 0.25V (blue) and 0.05V (teal) vs Li/Li^+ in the cathodic sweep.

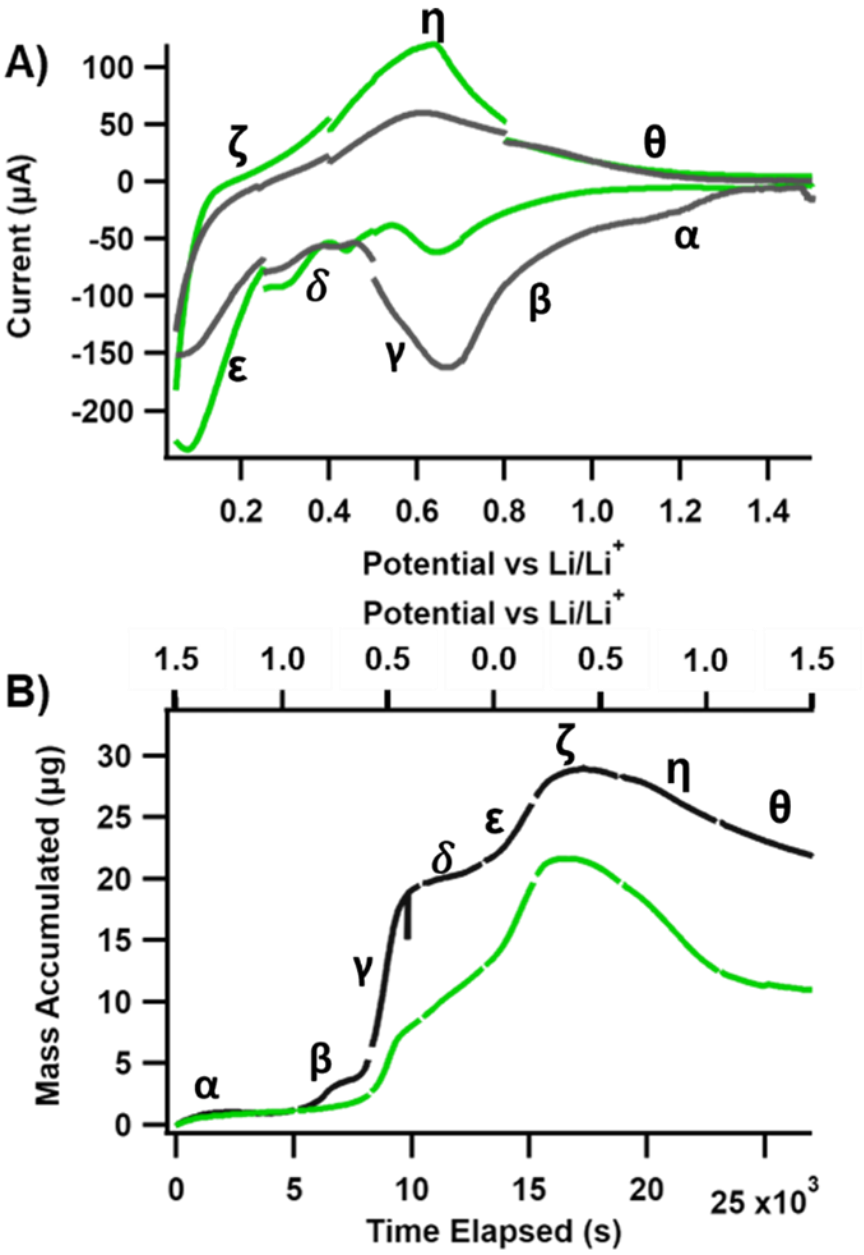

Figure 2. Overlaid EQCM voltammetry (A) and mass accumulation (B) curves for electrodes cycled with (green) and without (black) 5% by volume OS additive. The color coding from Figure 1 has been replaced, however the Greek letters assigned to each segment remain.

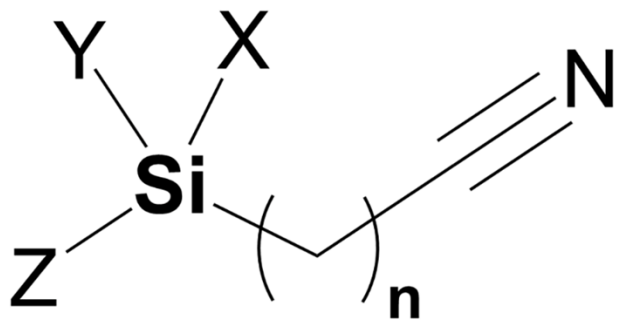

Figure 3. General molecular structure of organosilicon electrolyte additives. In this study, the organosilicon species used had the following structural features: X=fluorine, Y=CH_3, Z=CH_3, and n=3.

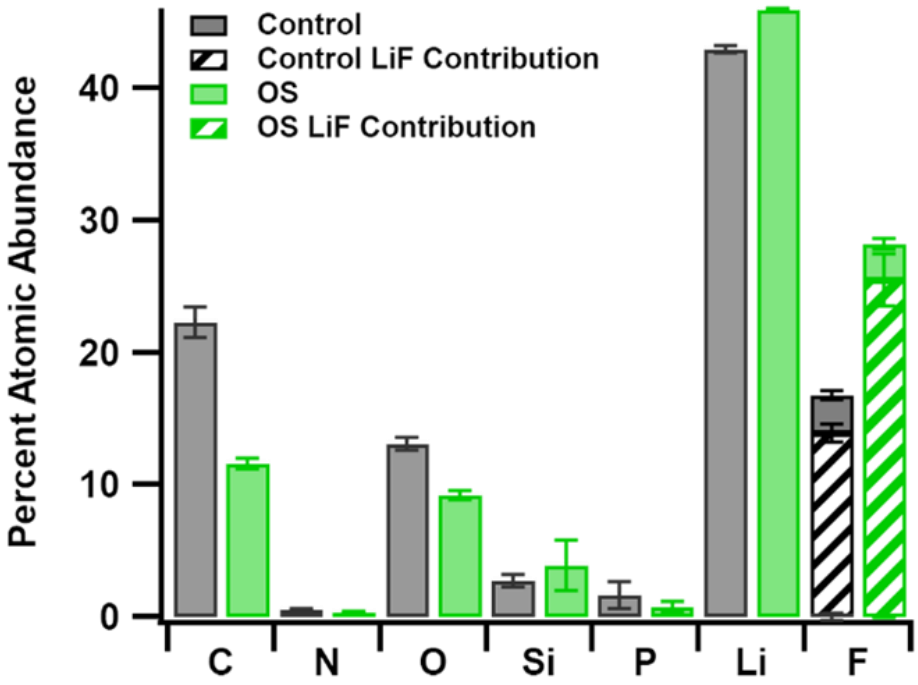

Figure 4. Percent atomic abundances on the surfaces of a-Si electrodes after one potentiostatic cycle. These electrodes were cycled in a coin cell geometry from 1.5 to 0.05V vs Li/Li^+ with a lithium counter/reference electrode. For the abundances of F in both the control and OS treated samples, the fraction of the F signal which is attributable to LiF is represented as a patterned bar, and the F signal from all other sources is represented with a solid bar. The overall height of the F bars still represents the total relative atomic abundance of F in the samples. High resolution scans of the F1S region are provided in Figure S5.

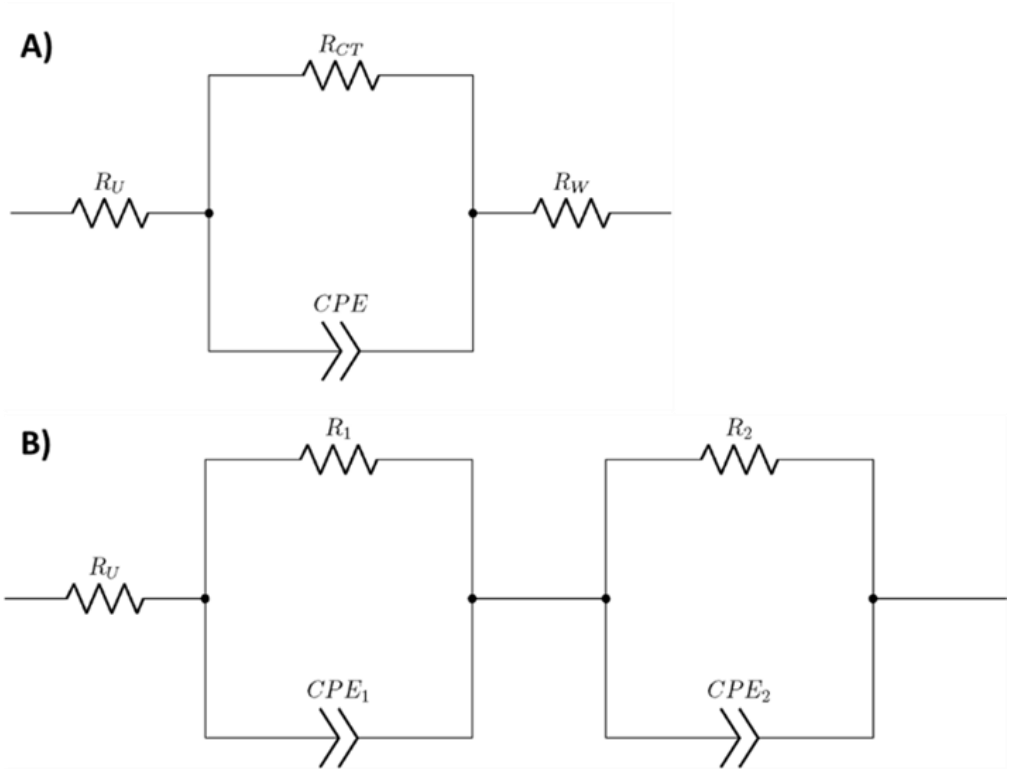

Figure 5. Equivalent model circuits used to analyze the impedance spectrscopy collected during the EQCM-EIS experiments. R_U represents the uncompensated resistance in the cell, R_{CT} in 5a is the charge-transfer resistance of the single electron transfer process. In Figure 5b, R_1 and R_2 represent charge-transfer resistances for the high and low frequency impedance responses respectively. The double chevrons in Figures 5a and 5b represent a constant phase element (CPE), and finally element R_W in 5a represents a Warburg impedance element. The single RC element model circuit (A) was used for all of the impedance spectra except for those collected at the end of segment γ. For the spectra collected at the end of segment γ, the two RC element model circuit (B) was used. Nyquist plots showing both raw impedance data and the equivalent circuit modelling results are provided in Figures S3 and S4.

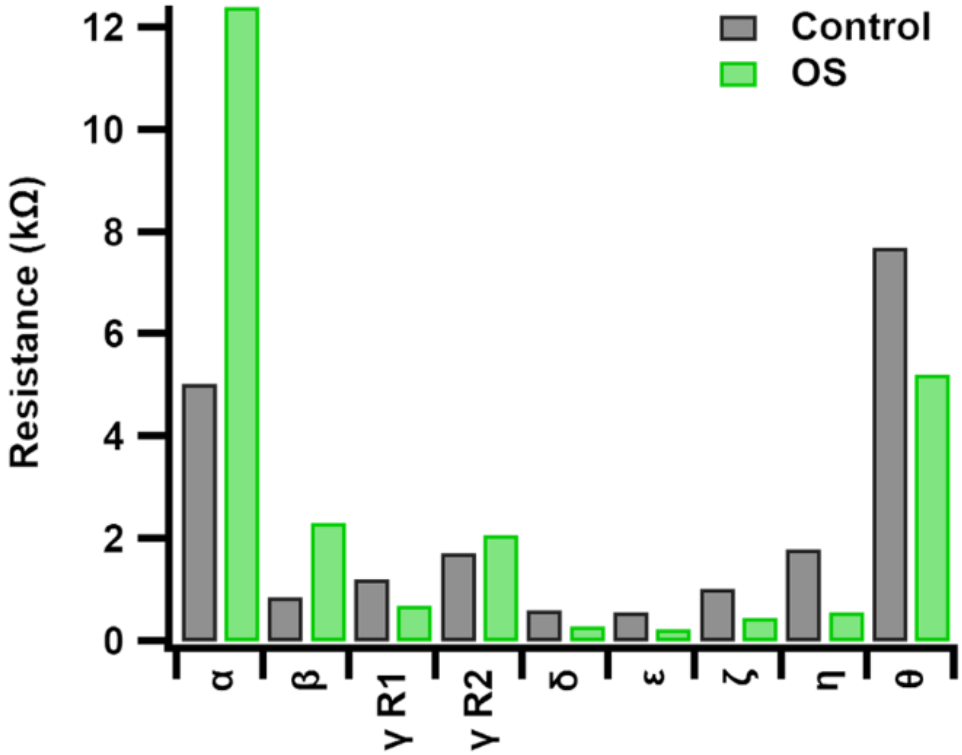

Figure 6. Charge-transfer resistance values calculated by equivalent circuit modeling of impedance data using the equivalent model circuits in Figure 5. Resistance values between the cell with OS additive (green) and without additive (grey) are compared for each impedance measurement. Note that in the case of the impedance measurement at the end of segment γ, there were two observed charge-transfer events in the Nyquist plot and thus two charge transfer resistance values are reported. The bars labelled γ R1 report values for the higher frequency event, and those labelled γ R2 the lower frequency event.

2.8 Supplementary Information

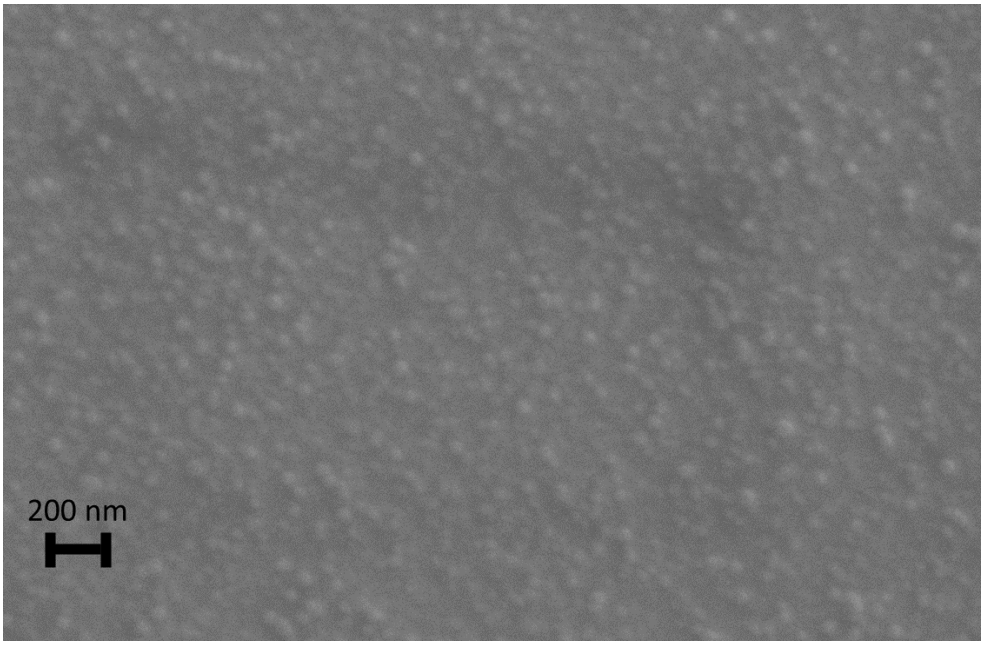

Figure S1. SEM Image of Finished Model electrode surface. This image shows that the prepared model electrodes are both non-porous and relatively flat.

Film density was also investigated by measuring the oscillation frequency of a 5 MHz Au/Cr crystal before and after test depositions of Si thin films. The recorded frequency change of these crystals was -1493, which when combined with the -56.6 Hz•cm^2/μg mass sensitivity of these crystals gives a film mass of 133.7 ug. Using a nominal thickness of 100 nm as provided by the calibrated crystal monitors in the metal evaporation tool used to generate the film and the area of 1 inch diameter coated surface of the oscillator, this gives a film density of 2.33 g/mL, which is in excellent agreement with commonly reported values for the density of silicon. This suggests that the films contain very little void volume and are likely non-porous, and this is corroborated by an SEM image of the prepared surface.

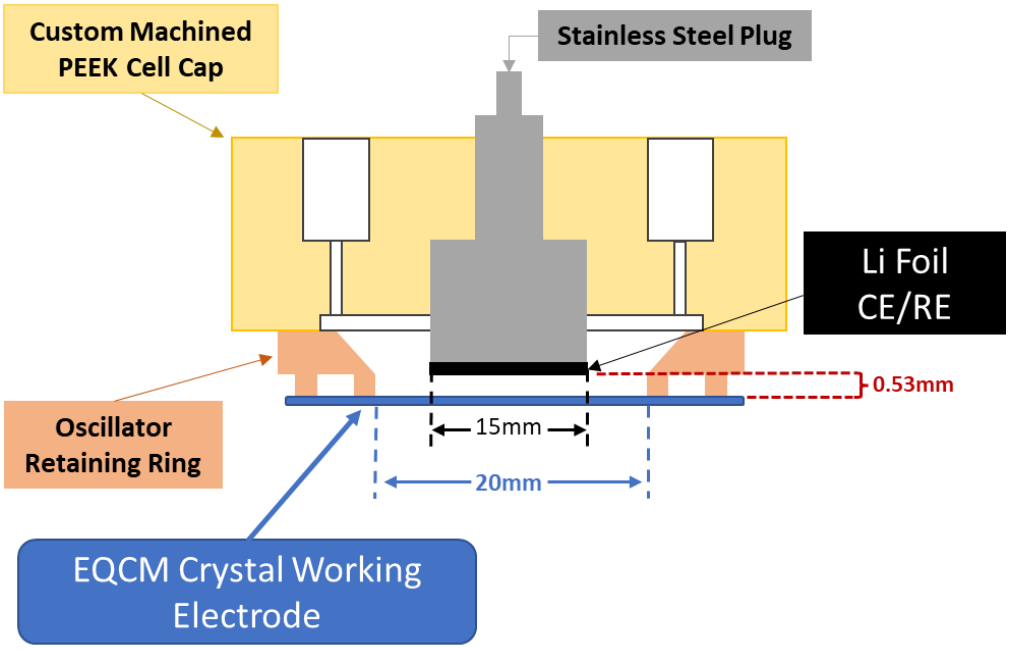

Figure S2. Cut-away schematic of the custom machined EQCM cell cap made to interface with the SRSQCM200 instrument utilized in this work. This cell was constructed in a 2-electrode setup with a Li metal counter/reference electrode with an electrode separation between the Si coated EQCM crystal working electrode and the Li foil of 0.53mm.

The internal electrolyte capacity of the PEEK cell cap was calculated to be 533 µL, which when filled completely with electrolyte solution would result in a solution loading of about 640 mg assuming a solution density of 1.2 g/mL. This yields a solution mass to electrode mass ratio of about 4800, which is comparable to the flooding factors of EQCM cell designs previously reported in the literature [15,16].

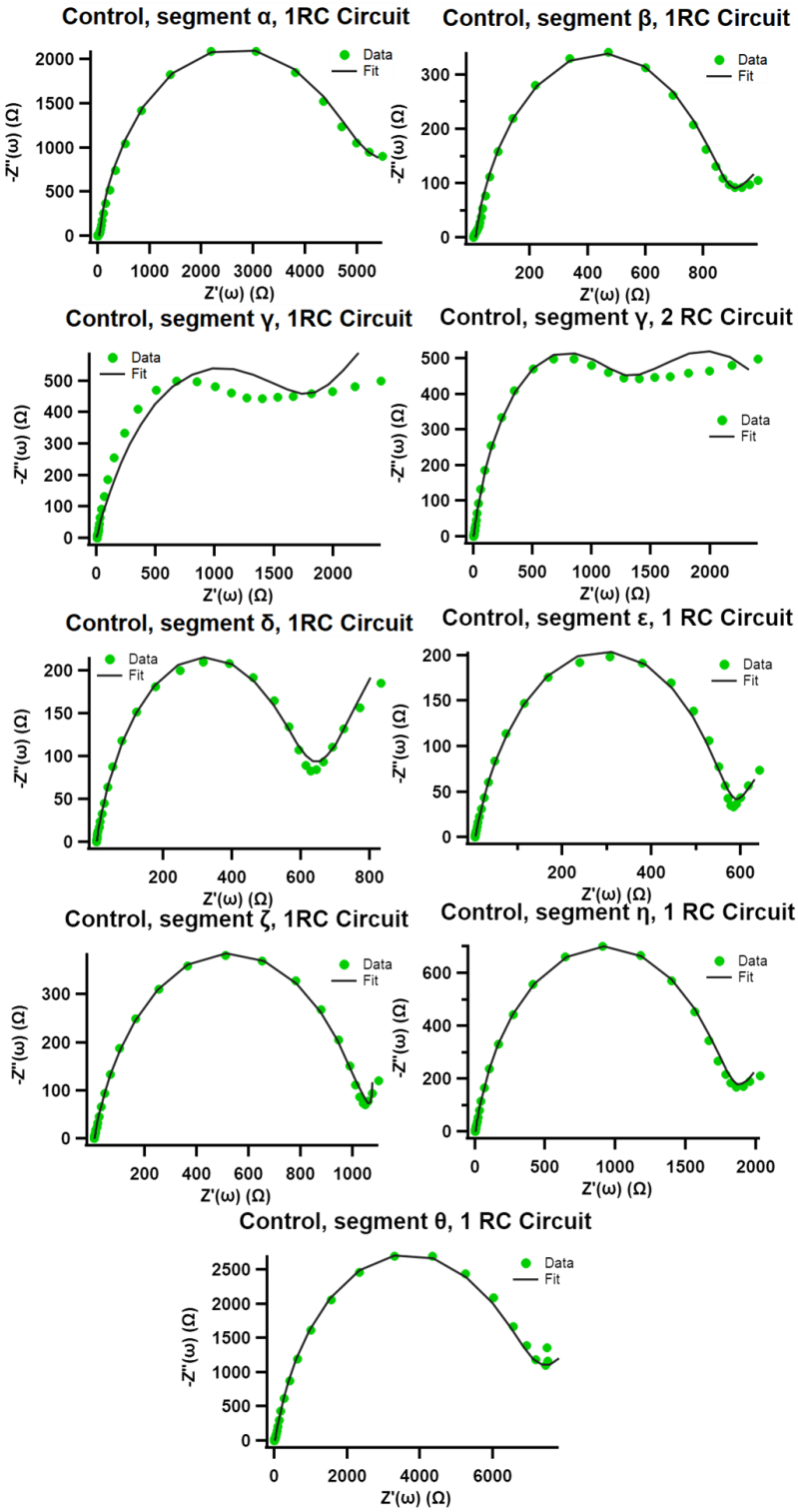

Figure S3. Nyquist plots of EIS data collected during *in operando* EQCMEIS experiments performed using the control electrolyte. Both the 1RC and 2RC element equivalent model circuit fitting results are shown for the data collected at the end of segment γ.

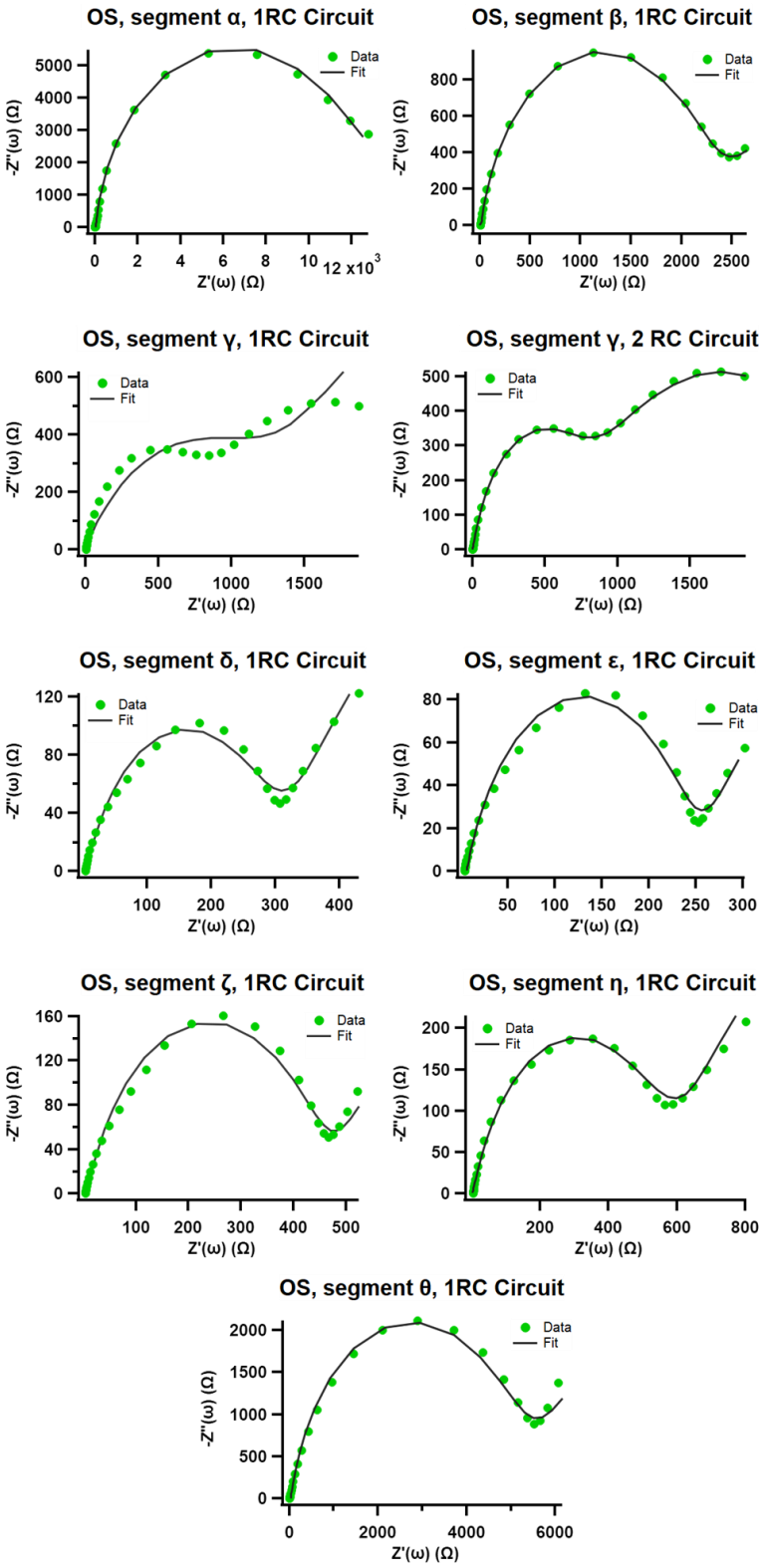

Figure S4. Nyquist plots of EIS data collected during *in operando* EQCMEIS experiments performed using OS-containing electrolyte. Both the 1RC and 2RC element equivalent model circuit fitting results are shown for the data collected at the end of segment γ.

All data in both the additive treated and control sets, except the ones collected at the end of segment γ, are fit very well by the 1 RC element equivalent model circuit featured in Figure 5a. The segment γ data is shown with both the 1 RC element model fit as well as the 2 RC element fit shown in Figure 5b, demonstrating the inability of the 1RC element model to appropriately fit those data sets and thus the necessity of the 2RC element model circuit that was used in this work.

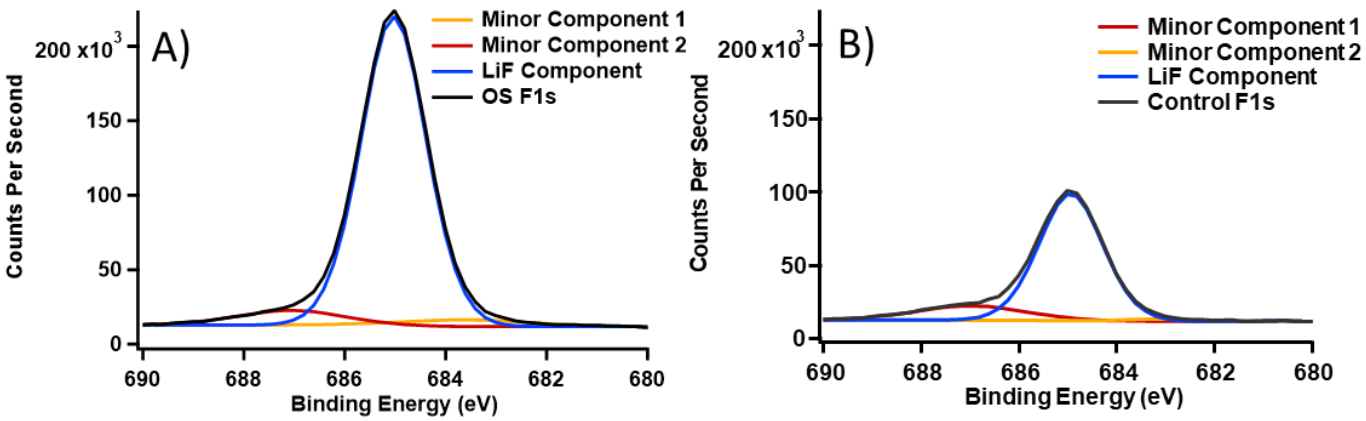

Figure S5. F1s region high resolution scans (black traces) of an A) OS-treated cell and B) a control cell. Each scan required three component peaks to fit appropriately, two of which are minority components (red and yellow traces) and one which is the LiF component peak (blue) centered at 685 eV.

The F high resolution scan shows that the increase in F abundance discussed in Figure 4 is entirely due to the increase in peak area from a component peak centered at 685eV, which is strong evidence of it being LiF. Peak areas of the two minor components between the additive-treated and control cells are also largely consistent, which is also echoed in Figure 4.

Regarding the flooding factor of coin cell assemblies used this this study, the same 100 nm Si thin films as in the EQCM-EIS sample preparations were deposited on to 1 cm^2 squares of Ti shim, giving a Si loading of 42 µg. Our coin cells were heavily flooded, using 200 µL of electrolyte solution to facilitate better comparison to the comparatively large free volume of the EQCM cell, which gives a flooding factor in the coin cells of 5600. This is of course an exceptionally large flooding factor for a coin cell; however, it was chosen to make comparisons in surface chemistry between the coin cells used to generate XPS data and the EQCM cells used for gravimetric and impedance studies more reliable.

2.9 References

(1) Jin, Y.; Zhu, B.; Lu, Z.; Liu, N.; Zhu, J. Challenges and Recent Progress in the Development of Si Anodes for Lithium-Ion Battery. *Advanced Energy Materials* **2017**, *7* (23). DOI: 10.1002/aenm.201700715.

(2) Zuo, X.; Zhu, J.; Müller-Buschbaum, P.; Cheng, Y.-J. Silicon based lithium-ion battery anodes: A chronicle perspective review. *Nano Energy* **2017**, *31*, 113-143. DOI: 10.1016/j.nanoen.2016.11.013.

(3) Wu, Q.; Shi, B.; Bareno, J.; Liu, Y.; Maroni, V. A.; Zhai, D.; Dees, D. W.; Lu, W. Investigations of Si Thin Films as Anode of Lithium-Ion Batteries. *ACS Appl Mater Interfaces* **2018**, *10* (4), 3487-3494. DOI: 10.1021/acsami.7b13980 From NLM PubMed-not-MEDLINE.

(4) Xu, C.; Lindgren, F.; Philippe, B.; Gorgoi, M.; Björefors, F.; Edström, K.; Gustafsson, T. Improved Performance of the Silicon Anode for Li-Ion Batteries: Understanding the Surface Modification Mechanism of Fluoroethylene Carbonate as an Effective Electrolyte Additive. *Chemistry of Materials* **2015**, *27* (7), 2591-2599. DOI: 10.1021/acs.chemmater.5b00339.

(5) Nie, M.; Abraham, D. P.; Chen, Y.; Bose, A.; Lucht, B. L. Silicon Solid Electrolyte Interphase (SEI) of Lithium Ion Battery Characterized by Microscopy and Spectroscopy. *The Journal of Physical Chemistry C* **2013**, *117* (26), 13403-13412. DOI: 10.1021/jp404155y.

(6) Rikka, V. R.; Sahu, S. R.; Chatterjee, A.; Satyam, P. V.; Prakash, R.; Rao, M. S. R.; Gopalan, R.; Sundararajan, G. In Situ/ex Situ Investigations on the Formation of the Mosaic Solid Electrolyte Interface Layer on Graphite Anode for Lithium-Ion Batteries. *The Journal of Physical Chemistry C* **2018**, *122* (50), 28717-28726. DOI: 10.1021/acs.jpcc.8b09210.

(7) Dedryvère, R.; Laruelle, S.; Grugeon, S.; Gireaud, L.; Tarascon, J. M.; Gonbeau, D. XPS Identification of the Organic and Inorganic Components of the Electrode/Electrolyte Interface Formed on a Metallic Cathode. *Journal of The Electrochemical Society* **2005**, *152* (4). DOI: 10.1149/1.1861994.

(8) Hui, J.; Gossage, Z. T.; Sarbapalli, D.; Hernandez-Burgos, K.; Rodriguez-Lopez, J. Advanced Electrochemical Analysis for Energy Storage Interfaces. *Anal Chem* **2019**, *91* (1), 60-83. DOI: 10.1021/acs.analchem.8b05115 From NLM PubMed-not-MEDLINE.

(9) Saqib, N.; Ganim, C. M.; Shelton, A. E.; Porter, J. M. On the Decomposition of Carbonate-Based Lithium-Ion Battery Electrolytes Studied Using Operando Infrared Spectroscopy. *Journal of The Electrochemical Society* **2018**, *165* (16), A4051-A4057. DOI: 10.1149/2.1051816jes.

(10) Kumar, R.; Tokranov, A.; Sheldon, B. W.; Xiao, X.; Huang, Z.; Li, C.; Mueller, T. In Situ and Operando Investigations of Failure Mechanisms of the Solid Electrolyte Interphase on Silicon Electrodes. *ACS Energy Letters* **2016**, *1* (4), 689-697. DOI: 10.1021/acsenergylett.6b00284.

(11) Tokranov, A.; Kumar, R.; Li, C.; Minne, S.; Xiao, X.; Sheldon, B. W. Control and Optimization of the Electrochemical and Mechanical Properties of the Solid Electrolyte Interphase on Silicon Electrodes in Lithium Ion Batteries. *Advanced Energy Materials* **2016**, *6* (8). DOI: 10.1002/aenm.201502302.

(12) Shi, F.; Ross, P. N.; Somorjai, G. A.; Komvopoulos, K. The Chemistry of Electrolyte Reduction on Silicon Electrodes Revealed by in Situ ATR-FTIR Spectroscopy. *The Journal of Physical Chemistry C* **2017**, *121* (27), 14476-14483. DOI: 10.1021/acs.jpcc.7b04132.

(13) Saurbrey, G. Verwendung von Schwingquarzen zur Wagung diinner Schichten und zur Mikrowagung. *Zeitschrift fur Physik* **1959**, (155), 206-222.

(14) Dargel, V.; Shpigel, N.; Sigalov, S.; Nayak, P.; Levi, M. D.; Daikhin, L.; Aurbach, D. In situ real-time gravimetric and viscoelastic probing of surface films formation on lithium batteries electrodes. *Nat Commun* **2017**, *8* (1), 1389. DOI: 10.1038/s41467-017-01722-x From NLM PubMed-not-MEDLINE.

(15) Kitz, P. G.; Lacey, M. J.; Novak, P.; Berg, E. J. Operando EQCM-D with Simultaneous in Situ EIS: New Insights into Interphase Formation in Li Ion Batteries. *Anal Chem* **2019**, *91* (3), 2296-2303. DOI: 10.1021/acs.analchem.8b04924 From NLM PubMed-not-MEDLINE.

(16) Hubaud, A. A.; Yang, Z.; Schroeder, D. J.; Dogan, F.; Trahey, L.; Vaughey, J. T. Interfacial study of the role of SiO2 on Si anodes using electrochemical quartz crystal microbalance. *Journal of Power Sources* **2015**, *282*, 639-644. DOI: 10.1016/j.jpowsour.2015.02.006.

(17) Nishizawa, M.; Uchiyama, T.; Itoh, T.; Abe, T.; Uchida, I. Electrochemical Quartz Crystal Microbalance for Insertion/Extraction of Lithium in Spinel LiMn2O4 Thin Films. *Langmuir* **1999**, (15), 4949-4951.

(18) Tavassol, H.; Buthker, J. W.; Ferguson, G. A.; Curtiss, L. A.; Gewirth, A. A. Solvent Oligomerization
during SEI Formation on Model Systems for Li-Ion Battery Anodes. *Journal of The Electrochemical Society* **2012**, *159* (6), A730-A738. DOI: 10.1149/2.067206jes.

(19) Middlemiss, L. A.; Rennie, A. J. R.; Sayers, R.; West, A. R. Characterisation of batteries by electrochemical impedance spectroscopy. *Energy Reports* **2020**, *6*, 232-241. DOI: 10.1016/j.egyr.2020.03.029.

(20) Shim, J.; Striebel, K. A. Characterization of high-power lithium-ion cells during constant current cycling. *Journal of Power Sources* **2003**, *122* (2), 188-194. DOI: 10.1016/s0378-7753(03)00351-3.

(21) Andre, D.; Meiler, M.; Steiner, K.; Walz, H.; Soczka-Guth, T.; Sauer, D. U. Characterization of high-power lithium-ion batteries by electrochemical impedance spectroscopy. II: Modelling. *Journal of Power Sources* **2011**, *196* (12), 5349-5356. DOI: 10.1016/j.jpowsour.2010.07.071.

(22) Zhang, S. S.; Xu, K.; Jow, T. R. EIS study on the formation of solid electrolyte interface in Li-ion battery. *Electrochimica Acta* **2006**, *51* (8-9), 1636-1640. DOI: 10.1016/j.electacta.2005.02.137.

(23) Murbach, M.; Gerwe, B.; Dawson-Elli, N.; Tsui, L.-k. impedance.py: A Python package for electrochemical impedance analysis. *Journal of Open Source Software* **2020**, *5* (52). DOI: 10.21105/joss.02349.

(24) Fairley, N.; Fernandez, V.; Richard-Plouet, M.; Guillot-Deudon, C.; Walton, J.; Smith, E.; Flahaut, D.; Greiner, M.; Biesinger, M.; Tougaard, S.; et al. Systematic and collaborative approach to problem solving using X-ray photoelectron spectroscopy. *Applied Surface Science Advances* **2021**, *5*. DOI: 10.1016/j.apsadv.2021.100112.

(25) Michan, A. L.; Leskes, M.; Grey, C. P. Voltage Dependent Solid Electrolyte Interphase Formation in Silicon Electrodes: Monitoring the Formation of Organic Decomposition Products. *Chemistry of Materials* **2015**, *28* (1), 385-398. DOI: 10.1021/acs.chemmater.5b04408.

(26) Ohara, S.; Suzuki, J.; Sekine, K.; Takamura, T. Li insertion/extraction reaction at a Si film evaporated on a Ni foil. *Journal of Power Sources* **2003**, *119-121*, 591-596. DOI: 10.1016/s0378-7753(03)00301-x.

(27) Takamura, T.; Ohara, S.; Uehara, M.; Suzuki, J.; Sekine, K. A vacuum deposited Si film having a Li extraction capacity over 2000 mAh/g with a long cycle life. *Journal of Power Sources* **2004**, *129* (1), 96-100. DOI: 10.1016/j.jpowsour.2003.11.014.

(28) Graetz, J.; Ahn, C. C.; Yazami, R.; Fultz, B. Highly Reversible Lithium Storage in Nanostructured Silicon. *Electrochemical and Solid-State Letters* **2003**, *6* (9). DOI: 10.1149/1.1596917.

(29) Obrovac, M. N.; Krause, L. J. Reversible Cycling of Crystalline Silicon Powder. *Journal of The Electrochemical Society* **2007**, *154* (2). DOI: 10.1149/1.2402112.

(30) Choi, N.-S.; Yew, K. H.; Lee, K. Y.; Sung, M.; Kim, H.; Kim, S.-S. Effect of fluoroethylene carbonate
additive on interfacial properties of silicon thin-film electrode. *Journal of Power Sources* **2006**, *161* (2), 1254-1259. DOI: 10.1016/j.jpowsour.2006.05.049.

(31) Kim, H.; Choi, J.; Sohn, H.-J.; Kang, T. The Insertion Mechanism of Lithium into Mg_2Si Anode Material for Li-Ion Batteries. *Journal of The Electrochemical Society* **1999**, *146* (12), 4401-4405.

(32) Yang, J.; Wachtler, M.; Winter, M.; Besenhard, J. O. Sub-Microcrystalline Sn and Sn - SnSb Powders as Lithium Storage Materials for Lithium-Ion Batteries. *Electrochemical and Solid State Letters* **1999**, *2* (4), 161-163.

(33) Zhang, W.-J. A review of the electrochemical performance of alloy anodes for lithium-ion batteries. *Journal of Power Sources* **2011**, *196* (1), 13-24. DOI: 10.1016/j.jpowsour.2010.07.020.

(34) Kim, J.-B.; Lee, H.-Y.; Lee, K.-S.; Lim, S.-H.; Lee, S.-M. Fe/Si multi-layer thin film anodes for lithium rechargeable thin film batteries. *Electrochemistry Communications* **2003**, *5* (7), 544-548. DOI: 10.1016/s1388-2481(03)00120-6.

(35) Takamura, T.; Uehara, M.; Suzuki, J.; Sekine, K.; Tamura, K. High capacity and long cycle life silicon anode for Li-ion battery. *Journal of Power Sources* **2006**, *158* (2), 1401-1404. DOI: 10.1016/j.jpowsour.2005.10.081.

(36) Guillot, S. L.; Usrey, M. L.; Peña-Hueso, A.; Kerber, B. M.; Zhou, L.; Du, P.; Johnson, T. Reduced Gassing In Lithium-Ion Batteries With Organosilicon Additives. *Journal of The Electrochemical Society* **2021**, *168* (3). DOI: 10.1149/1945-7111/abed25.

(37) Chen, X.; Li, X.; Mei, D.; Feng, J.; Hu, M. Y.; Hu, J.; Engelhard, M.; Zheng, J.; Xu, W.; Xiao, J.; et al. Reduction mechanism of fluoroethylene carbonate for stable solid-electrolyte interphase film on silicon anode. *ChemSusChem* **2014**, *7* (2), 549-554. DOI: 10.1002/cssc.201300770 From NLM Medline.

(38) Okuno, Y.; Ushirogata, K.; Sodeyama, K.; Tateyama, Y. Decomposition of the fluoroethylene carbonate additive and the glue effect of lithium fluoride products for the solid electrolyte interphase: an ab initio study. *Phys Chem Chem Phys* **2016**, *18* (12), 8643-8653. DOI: 10.1039/c5cp07583a From NLM PubMed-not-MEDLINE.

(39) Wenzel, S.; Randau, S.; Leichtweiß, T.; Weber, D. A.; Sann, J.; Zeier, W. G.; Janek, J. Direct Observation of the Interfacial Instability of the Fast Ionic Conductor Li10GeP2S12 at the Lithium Metal Anode. *Chemistry of Materials* **2016**, *28* (7), 2400-2407. DOI: 10.1021/acs.chemmater.6b00610.

(40) Sang, L.; Haasch, R. T.; Gewirth, A. A.; Nuzzo, R. G. Evolution at the Solid Electrolyte/Gold Electrode Interface during Lithium Deposition and Stripping. *Chemistry of Materials* **2017**, *29* (7), 3029-3037. DOI: 10.1021/acs.chemmater.7b00034.

(41) Ogihara, N.; Itou, Y.; Sasaki, T.; Takeuchi, Y. Impedance Spectroscopy Characterization of Porous Electrodes under Different Electrode Thickness Using a Symmetric Cell for High-Performance Lithium-Ion Batteries. *The Journal of Physical Chemistry C* **2015**, *119* (9), 4612-4619. DOI: 10.1021/jp512564f.

(42) Huang, Q.-A.; Shen, Y.; Huang, Y.; Zhang, L.; Zhang, J. Impedance Characteristics and Diagnoses of Automotive Lithium-Ion Batteries at 7.5% to 93.0% State of Charge. *Electrochimica Acta* **2016**, *219*, 751-765. DOI: 10.1016/j.electacta.2016.09.154.

Chapter 3: Uncovering the Mechanism of $O_2^{\bullet-}$ Scavenging by Organosilicon LIB Electrolyte Additives

This work is part of a manuscript currently in preparation. It is not the final version and will likely undergo further revision prior to submission and then again during peer review before publication.

3.1 Abstract

Reactive oxygen species, among them radical anions, have been a subject of numerous investigations within the lithium-ion battery and lithium-air battery communities because of their capacity for destructive side reactions with both solvent and electrolyte components of their chemistries. Electrolyte additive components which can control these destructive species represent an opportunity for technical innovation. Such innovation, however, is hampered by a lack of fundamental understanding of the reactive pathways that these compounds might take in systems as complex as battery electrolyte. With this in mind, we have explored a family of structurally related reactive oxygen species scavenging electrolyte additive molecules and quantified their fundamental reactivity with the superoxide radical anion. These experiments have also allowed us to determine the mechanism of action by which these additives scavenge radical anions, thereby supporting the rational design of future additives aimed at reactive oxygen species suppression in battery contexts.

3.2 Introduction

Gaseous byproducts generated during the cycling of pouch cell lithium-ion batteries (LIBs) are an issue of prominent concern in the battery community. Gas generation causes pouch swelling which not only decreases cell performance but also presents a considerable safety risk.[1-3] To address this problem, the battery community has produced consistent research into

electrolyte additives designed to limit gas production, however none have been completely successful.[4-12] Recently, a new family of organosilicon electrolyte additives has been introduced which features multiple functional avenues for suppression of electrolyte decomposition.[3, 13, 14] These organosilicon additives have further been demonstrated through post-mortem gassing analysis to be predominantly reducing gassing by preventing the decomposition of ethylene carbonate during high temperature storage and they have also been shown to provide increasingly potent gassing reduction with increasing degrees of fluorination. However, neither the mechanism by which this cyclic carbonate protection nor the source of the observed structure/function relationship between fluorination and gassing reduction potency are achieved are understood.[3]

Previous investigations into the mechanism of gas formation in LIB cells, particularly those employing high-energy cathode materials, have implicated reactive oxygen species release from cathode lattices or via the decomposition of adsorbed Li_2CO_3 as the trigger for carbonate decomposition and thus gas evolution.[15-21] The superoxide anion has been shown in related explorations to be especially reactive toward the cyclic carbonates in a nucleophilic attack pathway.[15, 16, 22, 23] Research efforts to limit the destructive potential of these nucleophilic oxygen species have produced several scavenging additive molecules with specific activity toward the superoxide anion in the past, these studies have identified several functional moieties to be beneficial to scavenger functionality, including silanes.[12, 24-30]

This study seeks to demonstrate that linear, fluorinated organosilicons represent a new and especially promising platform for development of multifunctional gas-suppressant additives. We will first demonstrate that these molecules have specific and rapid scavenging activity toward the superoxide radial, and thus likely perform the gas suppressing behavior identified by Guillot

et al by scavenging reactive oxygen species generated under their experimental conditions. We will further explore the structure-function relationship displayed by these additives between the degree of fluorination at the silane position and the species' superoxide scavenging activity and explain the root of this behavior by proposing a reaction mechanism for the scavenging reaction by these additives.

3.3 Materials and Methods

Cyclic Voltammetry Studies

Cyclic voltammetry experiments were conducted using a three-electrode cell, utilizing a planar glassy carbon working electrode, a platinum mesh counter electrode, and a Ag wire reference electrode. Electrolyte solutions for CV studies were prepared using dry acetonitrile (Millipore Sigma) dried over 4 Å molecular sieves (Alpha Aesar) and stored in an Argon atmosphere glovebox (LC Technology Solutions) (<1 ppm H_2O, <1 ppm O_2) and 0.1 M tetrabutylammonium perchlorate (TBAP) supporting electrolyte (Sigma Aldrich). Where indicated, solutions were sparged with oxygen gas for at least 15 minutes to saturate those solutions with dissolved oxygen. Electrolytes containing organosilicon additives were made by adding 2 vol% of the nonfluorinated and monofluorinated additive molecules or 0.25 vol% of the difluorinated additive molecule to the base electrolyte solution. Voltammograms were taken using a Biologic VSP-300 potentiostat with an installed Analog Ramp Generator to enable fast scan operation. Voltammograms were analyzed using the CVFit utility of the EC Lab software suite distributed by Biologic.

NMR Structural Determination

All NMR samples were prepared inside an Ar glovebox. Samples were prepared using a saturated solution of KO_2 (Acros Organics) in anhydrous deuterated acetonitrile (Sigma Aldrich), while control samples consisted of neat deuterated acetonitrile. Samples containing organosilicon additive were prepared by placing 12 μL of the neat monofluorinated organosilicon in an NMR tube and then a volume of KO2/acetonitrile sufficient to yield 0.01 M solutions of the organosilicon. Air free tubes were allowed to react for 10 minutes in the glovebox to help ensure reactions were complete before measurement, then capped and removed from the glovebox. Sealed samples were measured on a Bruker Neo-500 MHz spectrometer with a Prodigy BBO cryoprobe.

Gas Chromatography – Mass Spectroscopy

Samples for GC/MS analysis were prepared inside the glovebox using anhydrous acetonitrile either neat or saturated with KO_2 much like the NMR samples described above. GC-MS samples were prepared in GC vials by combining the dry acetonitrile with 12 μL of the neat monofluorinated organosilicon. Samples were again allowed to react in the glovebox for 10 minutes before being sealed and removed from the glovebox for analysis. GCMS samples were analyzed using a Shimadzu GCMS- QP2010 Ultra instrument. Analysis was performed using an injection volume of 1 μL and a split ratio of 150 onto a Select Silanes column (Agilent), running at 90 °C with a linear flow velocity of 46.6 cm/sec. MS analysis flowing the GC separation utilized a 3-minute solvent cut time and scanned from 10 to 200 m/z for 23 minutes.

3.4 Results and Discussion

A previous study performed by Guillot et al. presented two fluorinated organosilicon molecules as uniquely potent additives for gas suppression in lithium-ion batteries under high temperature storage conditions.[3] In the present study, we demonstrate the effect of increasing

degrees of fluorination on the superoxide scavenging ability of these additives as an indication of a possible mechanism by which these additives suppress gassing in Lithium-ion batteries. For the purposes of this work, we will focus on the 0-F additive (Figure 1A) the 1-F additive (Figure 1B), and the 2-F additive (Figure 1C).

The present study explores the structure-function relationship between the degree of fluorination in a set of model organosilicon additives via cyclic voltammetry. In dry, aprotic solvent, dissolved oxygen gas can be reduced to generate the superoxide radical anion. Previous studies have shown superoxide is generated in a one-electron transfer process as shown in Eq. 1.

$$O_2 + e^- \rightleftharpoons O_2^{\bullet -} \qquad \textit{Eq. 1}$$

and that this reaction can be characterized using classical theory for a heterogeneous electrochemical reaction under diffusion-controlled conditions.[31-33]

Figure 2 shows representative cyclic voltammograms measured at different scan rates for the base electrolyte (O_2 saturated, 1 M TBAP acetonitrile) and for the base electrolyte with the indicated amounts of the three different organosilicon (OS) additives. In the base electrolyte (Fig 2A), sweeping the potential to -1.0 V vs. Ag wire leads to a cathodic peak due to reduction of O_2 to $O_2^{\bullet -}$; as the potential is brought more positive there is an anodic peak near -0.4 V of nearly equal size due to re-oxidation of $O_2^{\bullet -}$ to O_2. The presence of the -0.4 V $O_2^{\bullet -}$ oxidation peak even at scan rates as slow as 200 mV/s shows that $O_2^{\bullet -}$ is highly stable in the base electrolyte.

Fig. 2B-2D show the impact of organosilicon additives on cyclic voltammograms. Fig. 2B shows data for the base electrolyte treated with a small amount of the non-fluorinated (0-F) OS additive. In this case the -0.4-eV peak is again nearly the same size as the -1.0 peak, indicating that the 0-F additive has no appreciable reactivity toward the superoxide radical anion.

When the 1F additive is used (Fib. 1C), superoxide is still formed but the anodic peak due to re-oxidation of $O_2^{\bullet-}$ back to O_2 is smaller than in the control and is nearly absent at the slowest scan rates. This behavior arises because the monofluorinated (1-F) organosilicon additives react with the generated superoxide radical, depleting the $O_2^{\bullet-}$ concentration before it can be oxidized back to O_2. This resulting electrochemical system comprised of an electron transfer process followed by a coupled homogeneous chemical reaction can be described in a 2-step reaction as described by Eq. 2 and Eq. 3:[31, 34]

$$O_2 + e^- \rightleftharpoons O_2^{\bullet-} \qquad \textit{Eq. 2}$$

$$O_2^{\bullet-} + OS \rightarrow X \qquad \textit{Eq. 3}$$

in which the organosilicon is represented as *OS* and the product generated by that chemical reaction is simply *X*. Notably, the absence of the $O_2^{\bullet-}$ peak at slow scan rates implies that the product "X" is electrochemically inactive. Consequently, when the electrode potential is swept back up to more positive potentials on the reverse scan of the voltammogram, less $O_2^{\bullet-}$ remains in solution to be converted back into O_2 and less anodic current is observed in the presence of the organosilicon. This observed suppression of the anodic peak is even more apparent in figure 2D, in the difluorinated additive 2-F was used. Here, even at a lower concentration (only 0.25%) the anodic peak is strongly reduced, indicating that the 2-F additive is even more reactive toward $O_2^{\bullet-}$ than 1-F additive is. Visual observation of the voltammograms provides a qualitative sense of the speed of the scavenging reaction, but to gain quantitative insight into this reaction, numerical modelling is required.

We performed modeling to extract kinetic parameters from voltametric data from a following reaction that was performed in two steps. First, a single cycle of the voltammetry of the electrochemical step alone, without the $O_2^{\bullet-}$ re-oxidation reaction, was modelled using the CVFit modelling software. CVFit uses a finite-element approach to fit experimental data to a

kinetics model based on the Butler-Vollmer equation and diffusion reactions, yielding values for the standard reduction potential (E^0), rate constant of the electron transfer step (k^0), transfer coefficient (α), and diffusion coefficients for O_2 and $O_2^{\bullet-}$. Fig. 3A shows a representative fit to experimental data, and Table S1 of the Supplementary Information shows the fit parameters for the optimized fit.

To abstract rates for $O_2^{\bullet-}$ scavenging reaction, similar fitting was performed using an extended model with an added irreversible. $O_2^{\bullet-}$ scavenging reaction (Eq.3). For a reaction of the form:

$$O_2^{\bullet-} + OS \rightarrow X$$

the kinetic reaction rate is given by[33]:

$$Rate = -\frac{d[O_2^{\bullet-}]}{dt} = k_{BM}[OS][O_2^{\bullet-}]$$

where k_{BM} is a bimolecular rate constant. If the concentration of OS is constant, this can be simplified into a pseudo-first-order reaction as: $Rate = -\frac{d[O_2^{\bullet-}]}{dt} = k_1[O_2^{\bullet-}]$ and rearranged to $\frac{1}{[O_2^{\bullet-}]}\frac{d[O_2^{\bullet-}]}{dt} = k_1$ where $k_1 = k_{BM}[OS]$ is a pseudo-first-order rate constant with units of sec^{-1}, which represents the effective lifetime of superoxide under the experimental conditions. Fitting in CVFit yields values of k_1. However, because k_1 depends on the concentration of OS the bimolecular rate constant k_{BM} is a better parameter for gauging the effectiveness of measurements performed at different concentrations.

We performed both constrained and relaxed fits. In the constrained fits, all parameters except the single rate constant k_1 were fixed at the values obtained from the initial fit to the starting (non-OS-containing) electrolyte. In the relaxed fits, values for the fitting parameters obtained from the starting electrolyte (with no OS, Fig. 2A) were used as initial values, but all fit

parameters were then allowed to relax to optimal values during the fit optimization. To get the most robust fit, we chose input data acquired at a scan rate where the OS reduces the amplitude of the $O_2^{\bullet-}$ re-oxidation peak to approximately half its initial value, so that the electrochemical re-oxidation and the $O_2^{\bullet-}$ scavenging occur at similar rates. Figure 3B shows results using the 2V/cycle data (from Fig. 2C).

Figure 3 shows the experimental CV and fit data for the baseline solution as well as the solution with all three additives, and the fitting results are summarized in Table 1 below. Comparing the voltammetry and fitting results between systems treated with each additive reveals a clear trend. The nonfluorinated additive (Figure 3B) displays no reactivity at all with the superoxide radical, even at a modest additive concentration of 2 vol%. The monofluorinated additive, (Figure 3C) has a rapid scavenging reaction with the superoxide radical, with an effective rate constant of 2.13 s^{-1} at 2 vol%. Finally, the difluorinated additive displays rapid scavenging activity, giving an effective rate constant of nearly 8 s^{-1} at 0.25 vol% in solution. These figures can be made directly comparable by converting from the effective rate constant to the bimolecular rate constant, achieved by dividing the effective rate constants by the molar concentration of the additives (0.14 M for 0-F and 1-F, and 0.02 M for 2-F) These results, as well as the collection of effective rate constants, molar concentrations of additives, and calculated bimolecular rate constants are collected in Table 1.

It should be noted that the physical constants produced by this approach are not necessarily consistent with those presented by other authors investigating the O_2/ $O_2^{\bullet-}$ couple in the past.[31, 32] In particular, the rate constant of the electron transfer process, k^0, produced by this method is about 10-times faster than Laoire et al. measured using the more traditional Tafel line method.[32] Determinations of k^0 are, however, known to be very sensitive to the status and

preparation of the electrode surface, and discrepancies as large as an order of magnitude are not uncommon.[35]

Regardless, the data within this study are internally consistent and reveal several interesting trends. First, the inactivity of the nonfluorinated 0-F additive suggests that the scavenging activity of the organosilicons is directly tied to the presence of that fluorine substituent. The fluorinated versions 1-F and 2F show a remarkable ability to react with and $O_2^{\bullet-}$. The bimolecular rate constants for the additives' reaction with superoxide increase from about 15 $M^{-1}s^{-1}$ in the singly fluorinated 1-F to 398 $M^{-1}s^{-1}$ in the doubly fluorinated 2-F, a 26-fold increase with addition of one more F atom. The above observations demonstrate that the scavenging activity of OS additives is highly dependent on the degree of fluorination at the silane position of the organosilicon additive. To further contextualize this finding, along with previous observations of the gassing suppressant qualities of the OS additives[3], it is possible to compare the rates of reaction with $O_2^{\bullet-}$ with that of ethylene carbonate (EC). To facilitate this comparison, the same process of measuring O_2/ $O_2^{\bullet-}$ and generating fitting results was repeated in an acetonitrile solution which contained 0.1 M TBAP with 50 vol% dissolved EC, and the data is presented in Figure 4, as well as in Table 1.

Figure 4 shows the experimental CV and fit data for the reduction of O_2 in an acetonitrile solution like the one used in the experiments detailed in Figure 3 but with a substantial fraction of 50 vol% EC and at much slower scan rates to those used for the OS compounds. This higher concentration and slower scan rate were necessary to accommodate the much slower reaction between EC and $O_2^{\bullet-}$ than was observed between the fluorinated OS compounds and $O_2^{\bullet-}$. When compared to EC, the 1-F additive reacts with $O_2^{\bullet-}$ 5 times faster than EC and in the case of the 2-F additive that ratio increases to more than 130 times. This large disparity in reactivities suggests

that the OS additives, even when present in low concentrations, could be preventing cell gassing in LIB systems by reacting with $O_2^{\bullet-}$ before the surrounding carbonate solvent can, thereby shielding them from decomposition.

To further the understanding of the superoxide scavenging performed by OS, we performed experiments aimed at identifying the reaction products using several NMR-based techniques including ^{1}H, ^{13}C, ^{19}F 1D NMR spectroscopy, and more advanced methods including ^{1}H-^{13}C Heteronuclear Single Quantum Coherence (HSQC) spectroscopy and Heteronuclear Multiple Bond Coherence (HMBC) measurements. Due to the complexity of the NMR experiments and data analysis, we focused these analyses on the monofluorinated additive (1-F) as a model system and summarize some of the main experimental observations in Fig. 5 and Fig. 6. More detailed procedures and analysis of the data from these experiments can be found in the Supplementary Information. In order to generate enough product for analysis by NMR, we introduced $O_2^{\bullet-}$ directly by adding potassium superoxide to deuterated acetonitrile and then adding 10 mM of the 1-F additive.

Fig. 5 shows ^{29}Si spectra of the two reactant solutions (acetonitrile and acetonitrile with added 1-F) after KO2 was added to both. In the control sample (i.e., with no OS compound added), the lone silicon chemical environment produces a doublet peak with a chemical shift (d) of δ=32.6 ppm. The splitting of this peak is caused by a hyperfine interaction between the ^{29}Si and the directly bonded fluorine atom. In the sample with included 1F (top, teal), a single new product peak appears as a singlet at δ=8.0 ppm. The presence of only one new peak strongly suggests that reaction between 1-F and the $O_2^{\bullet-}$ yields only one product. Further, the fact that this lone product produces a singlet peak in the ^{29}Si NMR spectrum indicates that the fluorine atom in the 1-F structure has been removed in the product. Together, these observations suggest that

the principal chemical change in the product structure involves removal of the F atom substituent.

To probe the integrity of the remaining bonds in the molecule, we performed HMBC spectroscopy on the reaction mixture. This technique selectively probes the presence of ^{1}H nuclei at different separations (numbers of intervening chemical bonds) from the ^{13}C atoms by identifying correlations between their respective atomic nuclei. Figure 6 presents the results of this experiment. Here, the ^{13}C NMR spectrum is shown along the left axis, and the ^{1}H NMR spectrum is shown along the top axis. The main body of the figures reveals the strength of any correlations between the ^{13}C and ^{1}H nuclei. Labels on individual peaks indicate whether the peaks are associated with the original reactant ("R") or with a reaction product ("P"), with an additional arbitrary number to enable specifying individual reactant and product peak (e.g., ^{1}H-P1, ^{1}H-P2, etc.).

In Figure 6, the HMBC spectrum of the reaction mixture is shown in two different scan windows, representing the same data plotted on two different regions of the chemical shifts The data in Fig. 6 show three important correlations between ^{1}H and ^{13}C resonances that are key to identifying the product structure. (1) In Figure 6A, two correlations are circled, one in blue between ^{1}H signal ^{1}H-P2 and ^{13}C-P4 (0.91 ^{1}H ppm, 122.6 ^{13}C ppm) and one in purple between ^{1}H signal ^{1}H-P3 and the same carbon signal ^{13}C-P4 (2.38 ^{1}H ppm, 122.6 ^{13}C ppm). These correlations are also represented on the structure of the product molecule drawn in the main figure area using colored arrows that point from each H atom on the molecule to the carbons it is correlated with. The presence of these correlations between the H atoms on the methylene carbons of the product structure and the carbon atom in the nitrile functional group indicate that the nitrile tail remains connected to the rest of the molecule in the product structure, as pictured

in Figure 6. (2) The enlarged region in 6B shows correlations between the H atoms on the methylene carbons (signals ^{1}H-P2 and ^{1}H-P3) and their neighboring carbons (signals ^{13}C-P2 and ^{13}C-P3) circled in orange and green respectively. These correlations are also represented using orange and green arrows on the structure in Figure 6B. The presence of these correlations, as well as those noted above in 6A, indicate that the carbon-carbon bond between the two methylene carbons in the product molecule structure remains intact after the scavenging reaction. Finally, (3) a correlation exists between the H atoms on the methyl groups attached to the Si atom, signal ^{1}H-P1, and the carbon atom of the methylene carbon nearest to the Si atom, signal ^{13}C-P3, circled in red. This correlation is represented with a red arrow connecting the H atoms on the methyl groups to the carbon on the other side of the Si atom. This last correlation demonstrates that the methyl groups on the silicon head group are attached, and that the silicon itself is still bound to the rest of the molecule in the product structure.

Taken together, the three correlations described immediately above indicate that no carbon-carbon, carbon-silicon, carbon-nitrogen, or carbon-hydrogen bonds were broken by the scavenging reaction, while the ^{29}Si spectrum shows that there is only one product and that his product involves loss of the F atom on the silicon head group. While the NMR analysis does not identify what replaced the F, we presume that since we introduced $O_2^{\bullet -}$ into the reactant mixture, the product structure likely incorporated an oxygen atom. Unfortunately, ^{17}O NMR is challenging due to the nature of the quadrupolar nucleus, so we turn to gas chromatography-mass spectroscopy to determine what substituent the product molecule has incorporated in place of the removed fluorine atom.

To further identify the reaction product structure, we conducted gas chromatography-mass spectrometry (GC-MS) analysis of the reaction mixture. These GC-MS studies showed

masses and fragmentation patterns consistent with the incorporation of a hydroxyl group as shown in Fig. 7 below. Further details of the GC-MS analysis and analysis of fragmentation patterns are provided in the supplementary information.

From these experiments, a few salient observations become quite evident. First, the fluorinated organosilicon additives presented in Figure 1 are capable of scavenging $O_2^{\bullet-}$ from solution at concentrations of several percent or less (typical of other additives commonly used in battery electrolytes), while the non-fluorinated structural relative has little or no reactivity. Our data show that the rate of the scavenging reaction increases dramatically when the degree of fluorination at the silicon position is raised from one to two. Taken together, these key observations from the voltammetry experiments presented here indicate that fluorination plays a critical role in endowing these additives with the ability to scavenge superoxide. Further exploration into the nature of the scavenging process revealed that the $O_2^{\bullet-}$ scavenging reaction performed by the 1-F additive generated only one product. This product maintains the internal structure of the original 1-F molecule with the substitution of a hydroxyl group in place of the F atom, as pictured in Figure 7. An earlier study on the reaction mechanism between $O_2^{\bullet-}$ and alkyl halides demonstrated that the radical anion dehalogenates such compounds in an S_N2 mechanism[33], and it is fully possible that the 1-F additive reacts with the radical in a similar way. This stands in great contrast to the cyclic carbonate solvents conventionally employed in LIB systems, such as ethylene carbonate or fluoroethylene carbonate, which upon nucleophilic attack are subject to complex decomposition pathways involving reactive intermediates as well as the generation of gaseous byproducts.[36] It is therefore suggested that the observed effectiveness of the fluorinated organosilicons as gassing suppressant additives in high-nickel NMC cells previously reported may be due to this underlying chemical reactivity, The organosilicons

scavenge the $O_2^{\bullet-}$ generated by the high energy cathodes before the reactive oxygen species can attack the bulk carbonate electrolyte, and sequester the oxygen into a relatively stable product, thereby preventing the decomposition of the carbonate solvents and the eventual generation of gas typically observed during high temperature storage of the cells.

The studies presented in this work were all conducted in acetonitrile as it provides a stable solvent with which the superoxide anion will not react. This allowed for the establishment of reaction conditions in which the reactivities of the individual additives could be isolated and studied. Though these observations are not made directly in a battery system, we believe this work provides important insights into the mechanisms of action by which fluorinated OS additives may suppress gassing in actual batteries, and that these insights would have been inaccessible if we had limited our investigation to explicitly applied contexts.

3.5 Conclusion

In this study, we combined the use of fundamental kinetic insights as well as chemical structure elucidation to suggest a potential mechanism by which fluorinated organosilicon additives may achieve their observed effectiveness as gas suppressing additives in lithium-ion batteries. CV analysis, coupled with finite element simulation, demonstrated that not only is the singly fluorinated 1-F many times more reactive toward $O_2^{\bullet-}$ than ethylene carbonate, but that the already impressive reactivity can be magnified by the inclusion of a second F atom in the 2-F additive. The drastic difference between the reactivity of the OS molecules and EC regarding their reactivity toward $O_2^{\bullet-}$ also helps to explain how these additives can successfully protect the carbonate solvent from attack by $O_2^{\bullet-}$ even at very low volume percentages. Finally, analysis of the product generated by the reaction between the 1-F additive and $O_2^{\bullet-}$ showed that the additive can sequester the radical into a single, nonreactive product. Further, this product appears to be

the result of a nucleophilic substitution reaction at the silicon position of the molecule, in which the F atom in 1-F is replaced by a hydroxyl group in the product.

3.6 Acknowledgments

This material is based upon work supported by the Office of Naval Research under Contract No. N00014-21-C-1075. Any opinions, findings and conclusions or recommendations expressed in this material are those of the Author(s) and do not necessarily reflect the views of the Office of Naval Research.

3.7 Figures and Tables

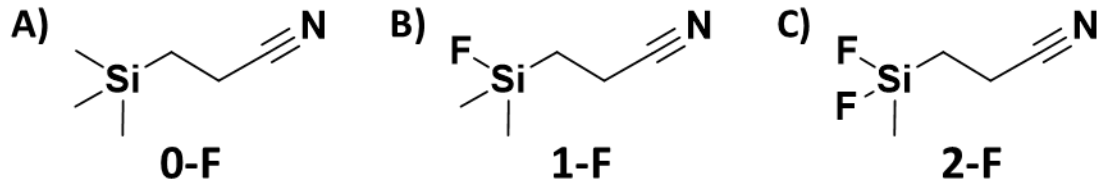

Figure 1. Molecular Structures of the three organosilicon molecules included in this study, exploring the structure across three degrees of fluorination at the silane position, zero (A), one (B), and two (C) with abbreviations 0-F, 1-F, and 2-F respectively.

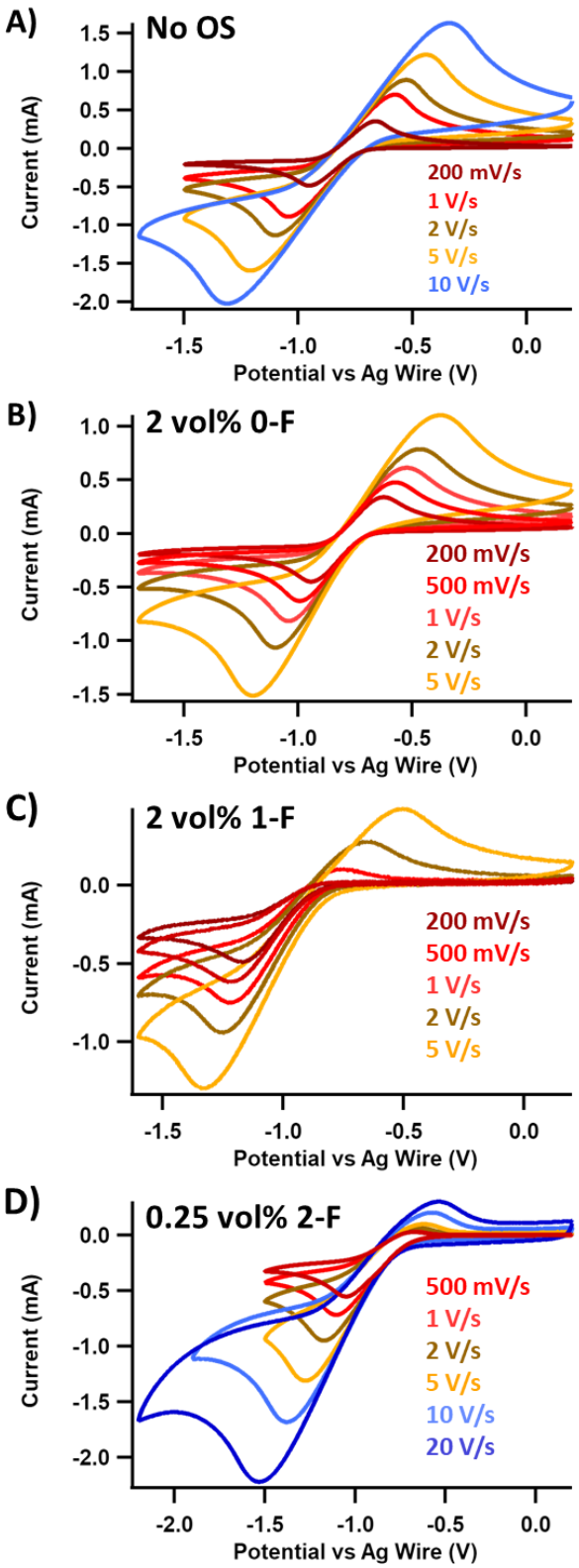

Figure 2. Cyclic Voltammograms of O_2 reduction in acetonitrile with 0.1 M TBAP supporting electrolyte on a glassy carbon working electrode. (A) No Additive, (B) 2 vol% 0-F, (C) 2 vol% 1-F, and (D) 0.25 vol% 2-F across several scan rates.

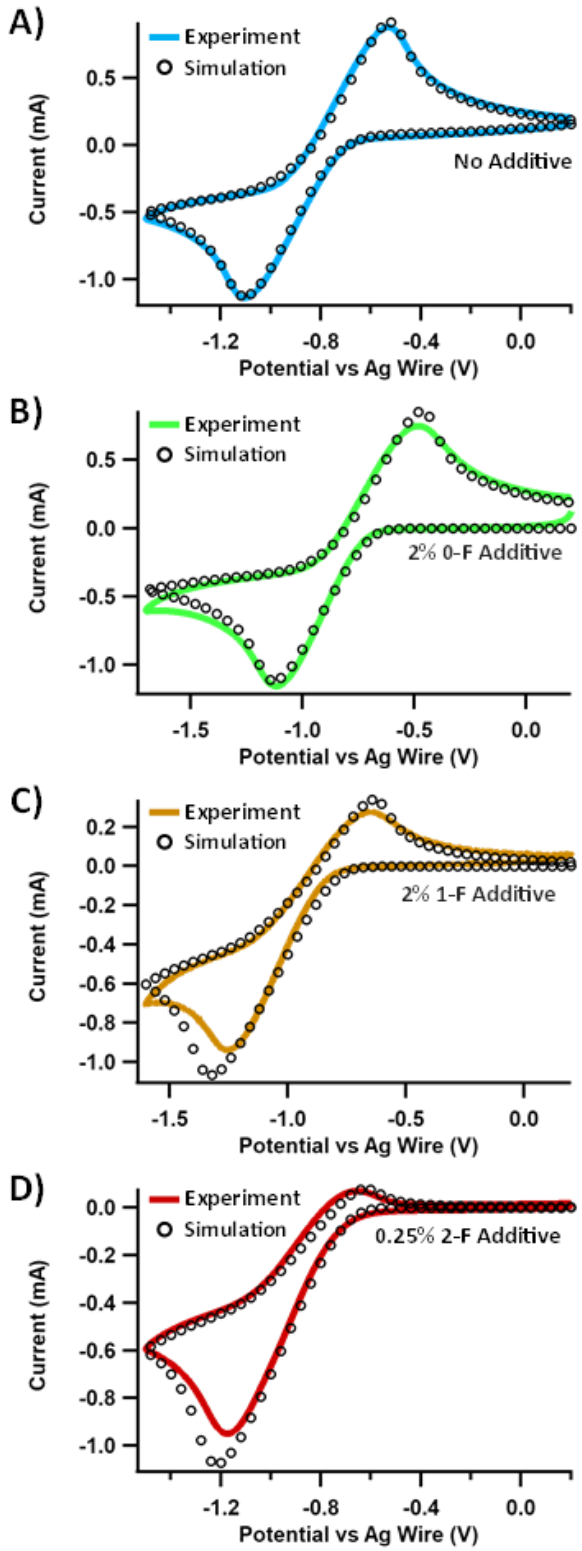

Figure 3. Cyclic voltammogram of reduction of O_2 in acetonitrile with 0.1 M TBAP on a glassy carbon electrode. All voltammograms are measured at 2 V/s scan rate. A) No additive, B) 2 vol% 0-F, C) 2 vol% 1-F, D) 0.25 vol% 2-F. Experimental data (solid line) and simulation (symbol).

	No Additive	0-F additive		1-F additive		2-F additive		Ethylene Carbonate	
	E step alone	E and C Steps	E and C Steps	E and C Steps	E and C Steps	E and C Steps	E and C Steps	E and C Steps	E and C Steps
	N/A	Constrained	Relaxed	Constrained	Relaxed	Constrained	Relaxed	Constrained	Relaxed
E^0 (V)	-0.71 ± 0.16	-0.686 ± 0.009	-0.690 ± 0.003	-0.785 ± 0.014	-0.791 ± 0.018	-0.689 ± 0.014	-0.713 ± 0.056	-0.719 ± 0.064	-0.69 ± 0.02
k^0 ($cm*s^{-1}$)	$2.43\times10^{-3} \pm 5.39\times10^{-9}$	2.43×10^{-3}	$(2.97 \pm 0.03)\times10^{-3}$	2.43×10^{-3}	$(2.49 \pm 0.07)\times10^{-3}$	2.43×10^{-3}	$(3.7 \pm 0.3)\times10^{-3}$	2.43×10^{-3}	$(9.7 \pm 0.4)\times10^{-4}$
k_1 (s^{-1})	N/A	$(2.41 \pm 0.19)\times10^{-4}$	$(1.87 \pm 1.79)\times10^{-4}$	2.13 ± 0.09	2.002 ± 0.008	8.0 ± 0.3	8.0 ± 0.4	0.063 ± 0.006	0.077 ± 0.003
Conc. (M)	N/A	0.14	0.14	0.14	0.14	0.02	0.02	6.0	6.0
k_{BM} ($M^{-1}s^{-1}$)	N/A	0.0017	0.0013	15	15	398	398	0.010	0.013

Table 1. Summary of additive concentrations used in voltametric analysis, as well as model-predicted effective rate constants (k_1) and calculated bimolecular rate constants (k_{BM}).

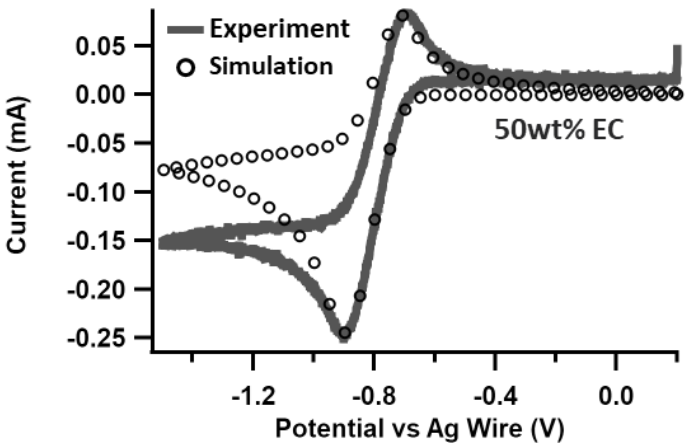

Figure 4. Cyclic voltammogram of reduction of O_2 in acetonitrile with 0.1 M TBAP and 50 wt% EC on a glassy carbon electrode at a scan rate of 50 mV/s.

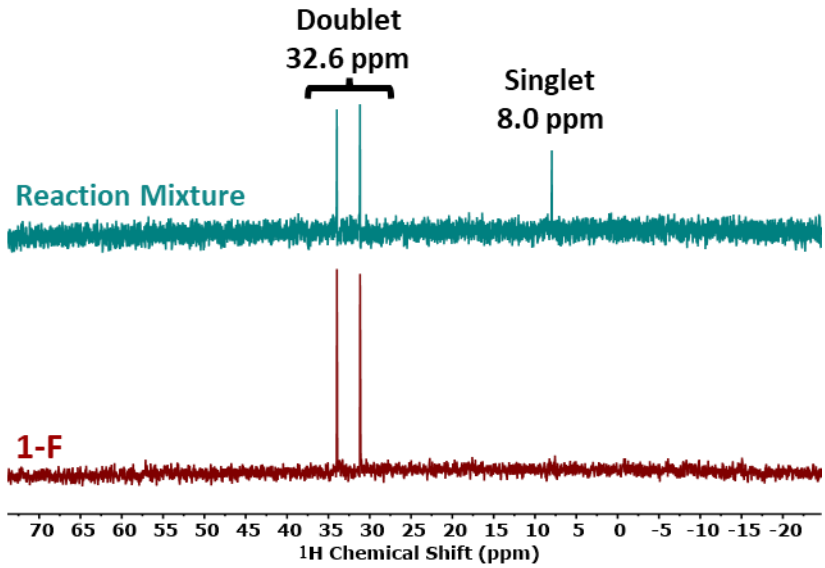

Figure 5. ^{29}Si spectra of the monofluorinated additive starting material (red) and the reaction mixture (teal) generated by adding 10 mM monofluorinated additive to a saturated solution of KO_2 in deuterated acetonitrile.

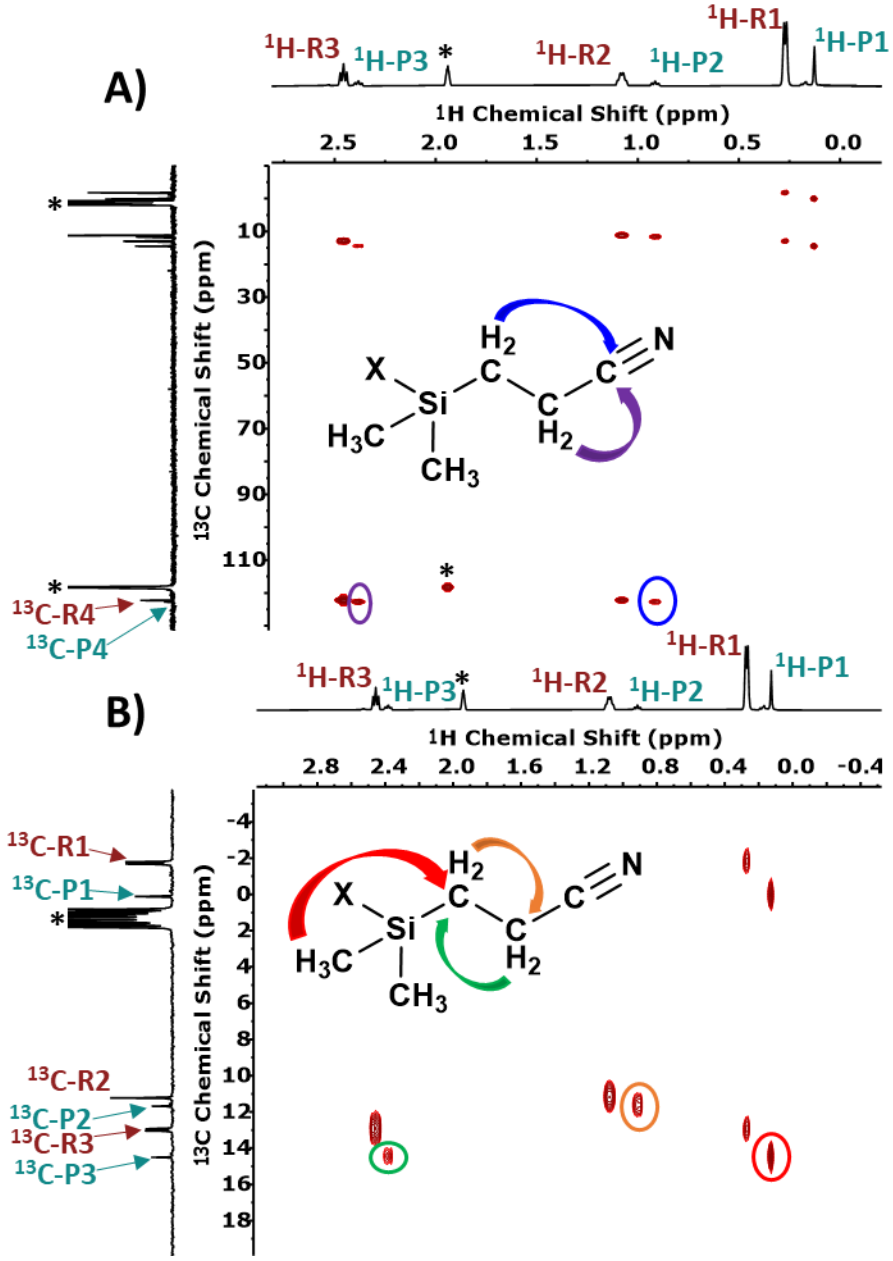

Figure 6. ^{1}H-^{13}C HMBC spectrum of reaction mixture in acetonitrile-d3. The ^{1}H spectrum of the reaction mixture is shown along the horizontal axis of the plot, the ^{13}C spectrum is shown along the vertical axis, and HMBC correlations between peaks are shown in the main plot area. 6a shows and expanded sweep width which demonstrates structural connectivity to the nitrile region of the spectra, and 6b shows a more detailed view of the remaining signals. Peak assignments are detailed in the supplementary information. Signals belonging to the solvent are marked with asterisks.

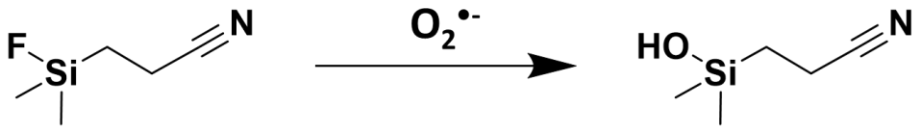

Figure 7. Reaction scheme for the scavenging of superoxide radical anion by the monofluorinated organosilicon additive.

3.8 Supplementary Information

	No Additive	1-F additive		2-F additive	
	E step alone	**E Params Fixed**	**E Params Floating**	**E Params Fixed**	**E Params Floating**
E_0 (V)	-0.715 ± 0.158	-0.785 ± 0.011	-0.791 ± 0.018	-0.689 ± 0.014	-0.713 ± 0.056
k_0 ($cm*s^{-1}$)	$2.43*10^{-3} \pm 5.39*10^{-9}$	$2.43*10^{-3}$	$(2.49 \pm 0.07)*10^{-3}$	$2.43*10^{-3}$	$(3.66 \pm 0.33)*10^{-3}$
α	0.45 ± 0.0001	0.45	0.45	0.45	0.45
C_{O_2} (M)	0.008	0.008	0.008	0.008	0.008
$C_{O_2^{\bullet-}}$ (M)	0	0	0	0	0
D_{O_2} (cm^2s^{-1})	$(8.25 \pm 0.11)*10^{-5}$	$8.25*10^{-5}$	$(7.35 \pm 0.03)*10^{-5}$	$8.25*10^{-5}$	$(6.83 \pm 0.47)*10^{-5}$
$D_{O_2^{\bullet-}}$ (cm^2s^{-1})	$(4.3 \pm 0.1)*10^{-7}$	$4.3*10^{-7}$	$(4.3\pm 0.3)*10^{-7}$	$4.3*10^{-7}$	$(4.4 \pm 0.2)*10^{-7}$
R_u (Ω)	171.5 ± 6.9	273.5 ± 9.2	275.7 ± 6.7	260.4 ± 8.5	272.3 ± 10.7
k_1 (s^{-1})	N/A	**2.125 ± 0.0945**	**2.002 ± 0.0085**	**7.953 ± 0.263**	**7.977 ± 0.413**

Table S1. Modelling parameters generated and used within the CVFit software to generate effective rate constants (K) for the scavenging reaction between the superoxide radical and the 1-F and 2-F organosilicon additives.

Table S1 above shows the modelling parameters generated by the CVFit software, and ultimately the effective rate constants produced by the modelling approach in this study. In the right most column, a parameter list is provided for the initial model shown in Figure 3A where the parameters related to the kinetics of the electron transfer step are generated in the initial modelling of the O_2/ $O_2^{\bullet-}$ redox couple without the coupled homogenous chemical reaction. The next parameter list shows the results of the fit shown in Figure 3B, where the parameters related to the kinetics of the electrochemical step are fixed and only the uncompensated resistance and the effective rate constant of the electrochemical step are allowed to be changed the minimization routine. In the next column, labelled "E params floating" the previously frozen parameters are allowed to move, and the minimization routine is again called to attempt to

improve the quality of the fit. Interestingly, this second, more relaxed fit does not meaningfully change the model's predicted effective rate constant for the scavenging process, indicating that the more constrained modelling approach used in this study produces relatively robust fits of the data. This process is repeated in the case of the 2-F additive, and again the constrained and relaxed models report nearly identical effective rate constants for the scavenging reaction for the 2-F additive.

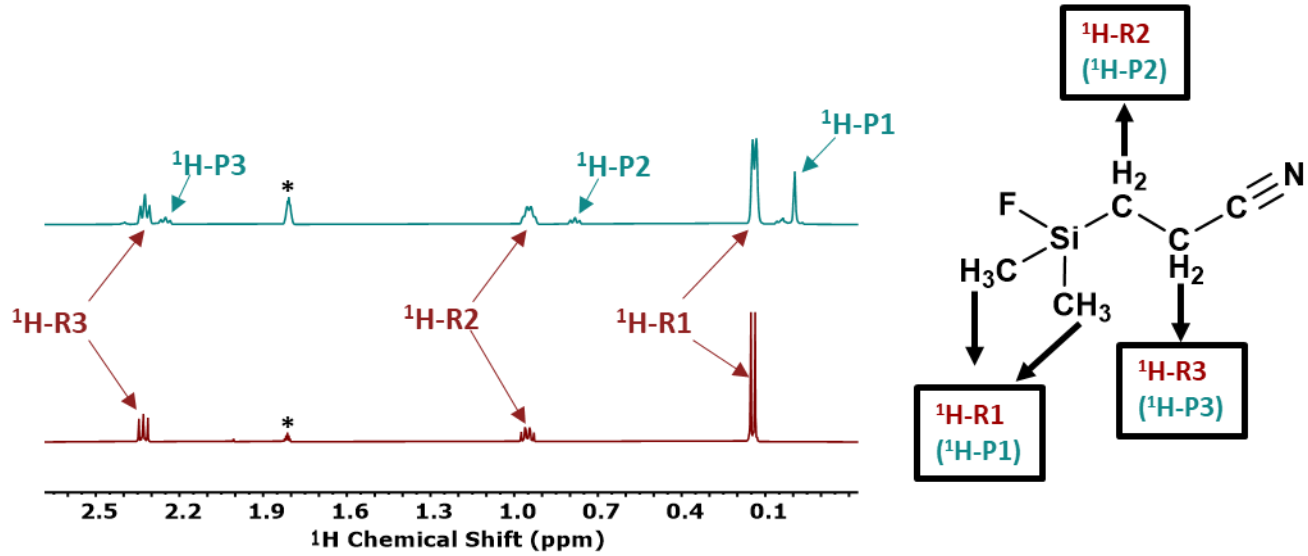

Figure S1. ^{1}H NMR spectra of the 1-F organosilicon (red, lower) and the reaction mixture produced by combining the 1-F organosilicon with KO_2 in solution (teal, upper). Each peak is assigned to either the original 1-F structure, marked with an "R", or a newly formed product species, marked with a "P", and then is numbered from right to left in order of appearance within those two groups. Peaks corresponding to the residual acetonitrile solvent are marked with an asterisk (*). A detailed structure of the 1-F additive is provided as well with the signals in the 1-F ^{1}H spectrum assigned to its corresponding H atom in the molecule, along with the product structure analogue assignments provided in parentheses.

Figure S1 shows a direct comparison between the ^{1}H NMR spectra of the 1-F organosilicon dissolved in deuterated acetonitrile in red and the ^{1}H NMR spectrum of the reaction mixture generated by combining the 1-F organosilicon with KO_2 in solution. KO_2 dissolves to produce K^+ and superoxide radical anion ($O_2^{\bullet-}$) in solution, allowing us to study the

products formed as the organosilicon scavenges the radical. In the ^{1}H spectra above, we see that all the peaks corresponding to the original organosilicon structure are still present in the reaction mixture including 1H-R1 at 0.27 ppm, 1H-R2 at 1.08 ppm, 1H-R3 at 2.46 ppm. In addition to these peaks, the reaction mixture spectrum also shows 3 new peaks, 1H-P1 at 0.13 ppm, 1H-P2 at 0.91 ppm, and 1H-P3 at 2.38 ppm. Based solely on the chemical shifts of these peaks, it appears that one or more product species are formed with functional groups that resemble the original 1-F organosilicon, with some additional shielding in the noted proton environments causing them to appear at less positive chemical shifts. Peak 1H-P1, based on chemical shift, likely corresponds to the methyl protons bound to the silicon atom in the product, have also collapsed from a doublet in the original molecule to a singlet in the product. The peak splitting in the original molecule is due to a two-bond coupling between the F atom on the 1-F structure, so the collapse of this doublet likely indicates that the Si atom in the product is no longer bound to F. Taking this assignment of peaks in the product spectrum to likely analogous functional groups in the product structure, the ^{1}H-P2 peak appears as a triplet while its analogue signal in the original structure appears as a pseudo-quartet, likely also a symptom of the loss of the spin ½ F atom from the product structure. Based on the appearance of long-range F coupling at this position that is not present in the ^{1}H-R3 or ^{1}H-P3 signals, it is likely that the ^{1}H-P2 signal corresponds to the methylene (CH_2) environment which is nearest to the Si atom in the 1-F and product structures. Finally, the ^{1}H-P3 signal likely corresponds to the methylene carbon in the product structure which is analogous to the methylene carbon directly bound to the nitrile functional group at the tail end of the original 1-F structure.

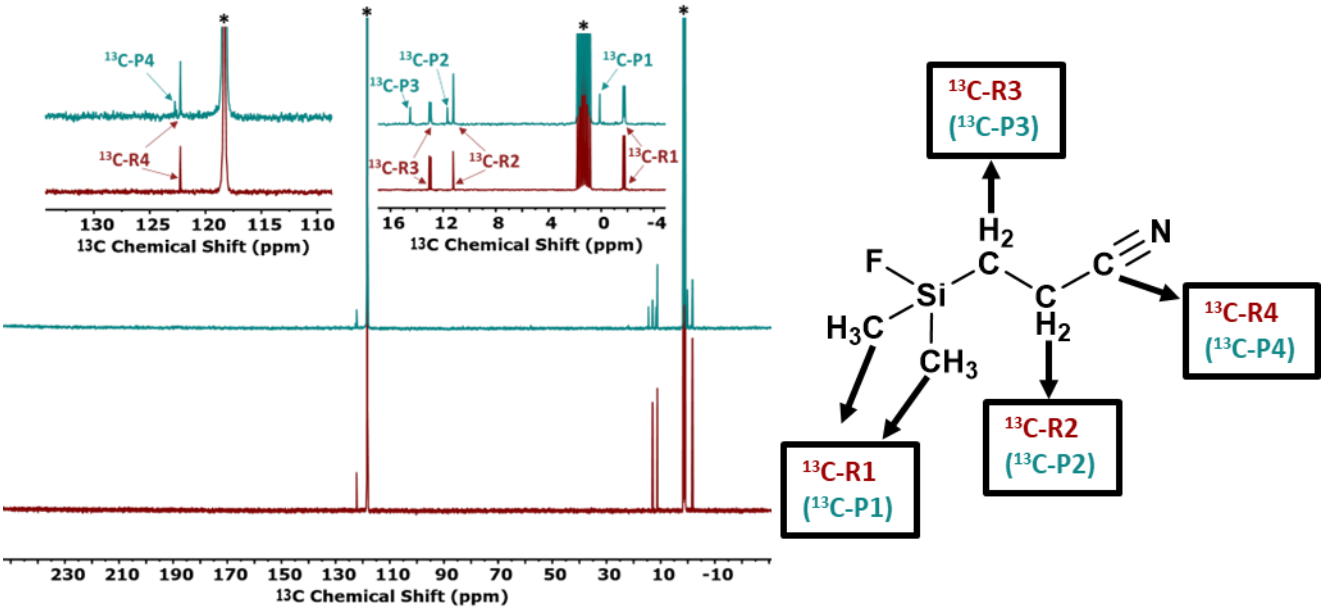

Figure S2. ^{13}C NMR spectra of the 1-F organosilicon (red, lower) and the reaction mixture produced by combining the 1-F organosilicon with KO_2 in solution (teal, upper). Each peak is assigned to either the as-received organosilicon, marked with an "R", or a newly formed product species, marked with a "P", and then is numbered from right to left in order of appearance within those two groups. Peaks corresponding to the residual acetonitrile solvent are marked with an asterisk (*). A detailed structure of the 1-F additive is provided as well with the signals in the 1-F ^{13}C spectrum assigned to its corresponding C atom in the molecule, along with the product structure analogue assignments provided in parentheses.

Figure S2 shows a direct comparison between the ^{13}C NMR spectra of the 1-F organosilicon in red and the reaction mixture of the organosilicon and KO_2 in teal, much as Figure S1 had done for the ^{1}H spectra. In Figure S2, two insets are also provided which allow for the signal dense regions of the spectra to be examined in greater detail. Like in Figure S1, app of the ^{13}C peaks corresponding to the original 1-F organosilicon species are maintained in the reaction mixture spectrum, appearing as ^{13}C-R1 at -1.78 ppm, ^{13}C-R2 at 11.1 ppm, ^{13}C-R3 at 12.9 ppm, and finally ^{13}C-R4 at 122.3 ppm. The reaction mixture spectrum also includes new peaks corresponding to product species including ^{13}C-P1 at 0.17 ppm, ^{13}C-P2 at 11.6 ppm, ^{13}C-P3 at 14.4, and lastly ^{13}C-P4 at 122.7 ppm. As with the ^{1}H-P1 peak in figure S1, it is likely that the ^{13}C-P1 peak corresponds to the methyl carbon atoms bound to the silicon atom in the

product. Also much like ^{1}H-P1, the doublet observed in the ^{13}C-R1 peak due to the two bond coupling to the attached F atom in the original structure collapsed to a singlet in ^{13}C-P1, again suggesting the loss of the F atom after the scavenging reaction. Beyond these general observations, however, it is impossible to tell if or how the proton environments in the product or products are connected to one another, or indeed how many separate product molecules have been generated by the scavenging reaction. Two-dimensional NMR studies are required to further determine the structure of this product(s) of the scavenging process and these are provided in Figures S3 and S4 below.

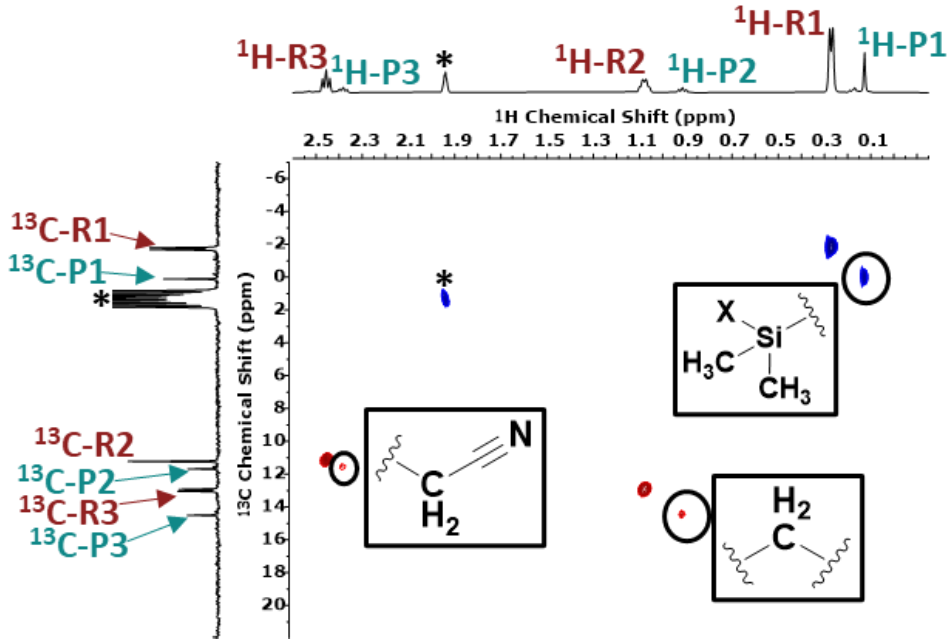

Figure S3. ^{1}H-^{13}C HSQC spectrum of the reaction mixture resulting from 10mM of the 1-F organosilicon being mixed into a saturated KO_2 solution in deuterated acetonitrile. This plot was phased such that correlations corresponding to methyl (CH3) and methine (CH) carbons are colored blue (as the methyl group on acetonitrile does) and methylene (CH2) carbons appear red. In the direct dimension along the horizontal axis, ^{1}H spectrum of the reaction mixture is plotted with the peaks annotated as they were in Figure S1 above. Along the indirect dimension on the vertical axis, the ^{13}C spectrum of the reaction mixture is presented with the same peak annotations as shown in Figure S2. Within the plot, ^{1}H-^{13}C correlations belonging to the product are indicated with arrows, and the local structure suggested by the HSQC result is presented next to the correlation signal. Signals corresponding to the acetonitrile solvent are noted with asterisks.

Figure S3 shows a ^{1}H -^{13}C HSQC spectrum of the product mixture generated by adding 10 mM 1-F additive to a saturated solution of KO_2 in deuterated acetonitrile. ^{1}H-^{13}C HSQC is a 2D NMR experiment that reveals correlations between the signals of hydrogen atoms and carbon atoms that share a direct covalent bond. For the purposes of this study, the HSQC plot above will be used to diagram short range chemical environments in the structure of the product of the superoxide reaction with the 1-F organosilicon. The left and top edges of Fig. S3 show the conventional 1-dimensional ^{13}C and ^{1}H NMR spectra of the reaction mixture respectively, while the larger central region reveals the correlations between the ^{1}H and ^{13}C resonances. In HSQC, the phases of the correlative signals have been adjusted such that correlations involving methylene groups (CH2) are shown in red and those from methyl and methine (CH3 and CH, respectively) are shown in blue, facilitating the identification of these groups.

Starting from the product peaks ^{1}H-P1 and ^{13}C-P1, a correlation is apparent between these peaks indicating that the hydrogen atoms in the product which generated ^{1}H-P1 peak are directly bound to the carbon atoms which generated the ^{13}C-P1 peaks. The phasing of the correlation signal indicates that these atoms are present as a methyl or methylene group and based on the chemical shift of these peaks as discussed in Figures S1 and S2, this signal likely corresponds to the methyl groups attached to the silicon in the product species. Moving in the positive direction along the direct (^{1}H) axis, the next product correlation appears between ^{1}H-P2 peak and the ^{13}C-P3 peak, which based again upon chemical shift and phasing as a methylene carbon most likely corresponds to the methylene carbon which was immediately bound to the silicon position in the starting material, and which connects the silicon group to the rest of the molecule. From this spectrum alone, however, we do not know how this methylene carbon is bound to the rest of the product structure surrounding it. Finally, there is another methylene

carbon correlation between ^{1}H-P3 peak and the ^{13}C-P2 peak, which corresponds to the product structure's methylene carbon which is bound to the carbon of the nitrile tail. It should also be noted that HSQC only shows correlations between hydrogen atoms and the carbon atoms directly bound to them, so the nitrile carbon which has no attached protons is invisible in this spectrum. A further limitation of the fact that HSQC shows only direct carbon-hydrogen bond connections is that it cannot show how these individual environments are bound to one another. HSQC alone cannot tell if the methylene carbon suggested by the resonance between the ^{1}H-P2 and the ^{13}C-P3 is still connected to the silane head group in the product structure, nor can it tell if the methylene carbons are still bound to one another. Further, it cannot tell definitively if the methylene carbon at position ^{13}C-P2 is indeed still bound to the nitrile carbon. To gain insight into these longer-range structural correlations, we must move to the HMBC spectrum shown in Figure 5 in the main body.

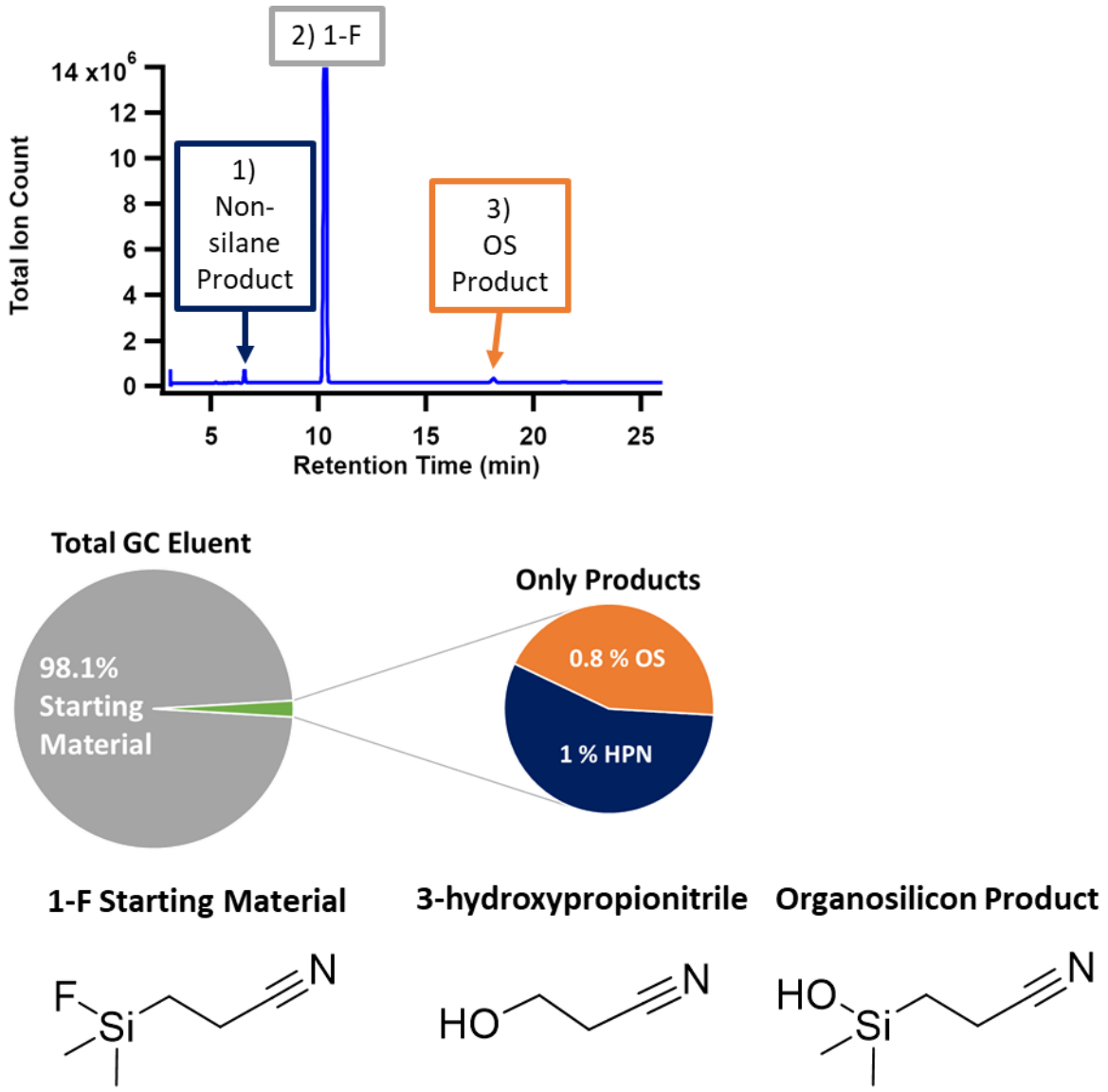

Figure S4. (Top) Gas chromatograph of the reaction mixture with the y axis adjusted so that the two major product peaks could be seen against the predominant species, (Middle) pie chart representation of the species present in the gas chromatogram separated and (Bottom) structures of the three species indicated by the fragmentation patterns produced during each elution.

Figure S4 shows the gas chromatogram of the reaction mixture as read by mass spectrometer detector in total ion count mode, which shows three species. The first, eluting at 6.5 minutes, gives a series of fragments including a base peak of 31 m/z, with other major peaks at 41, 29, and 15 m/z, identifiable as 3-hydroxypropionitrile, abbreviated in the pie chart in the bottom section of S4 as HPN. The second peak to elute shows the characteristic fragmentation pattern of the

original 1-F additive structure and is shown in the pie chart as starting material. The additive shows a base peak of 77 m/z with major peaks at 130, 116, 88, 49 and 47 m/z. Finally, the third peak to elute belongs to a species whose fragmentation pattern resembles that of the 1-F structure with the substitution of an alcohol functional group for the F atom, and shows a base peak at 89 with major peaks at 128, 100, 70, 59, and 43 m/z.

This third eluent, whose structure is provided in the bottom section of Figure S4 and in Figure 6, is likely the product observed in the NMR investigations above, but the 3-hydroxypropionitrile is not observed anywhere in those spectra. It was hypothesized that the hydroxyl derivative product species which is believed to be the direct product of the reaction between the additive and the superoxide radical was not thermally stable within the GC-MS instrument and was undergoing a secondary decomposition at the elevated temperatures required for gas chromatography. To confirm this, a simple NMR experiment was carried out in which 2 samples of the reaction mixture were prepared under air-free conditions in sealed vials along with a control which was also air-free but which contained only the 1-F additive without superoxide. The control vial and one of the reaction mixture vials were heated gently to 50°C in an oil bath for 10 minutes while the other reaction mixture via sat unheated on the bench. After heating, all three samples were diluted into deuterated acetonitrile and taken for ^{1}H NMR analysis. If the 3-hydroxypropionitrile species observed in the GC-MS results was indeed due to the instability of the product species at elevated temperatures, the heated sample should show NMR signals characteristic of the decomposition product. The results of this experiment are provided in Figure S5 below.

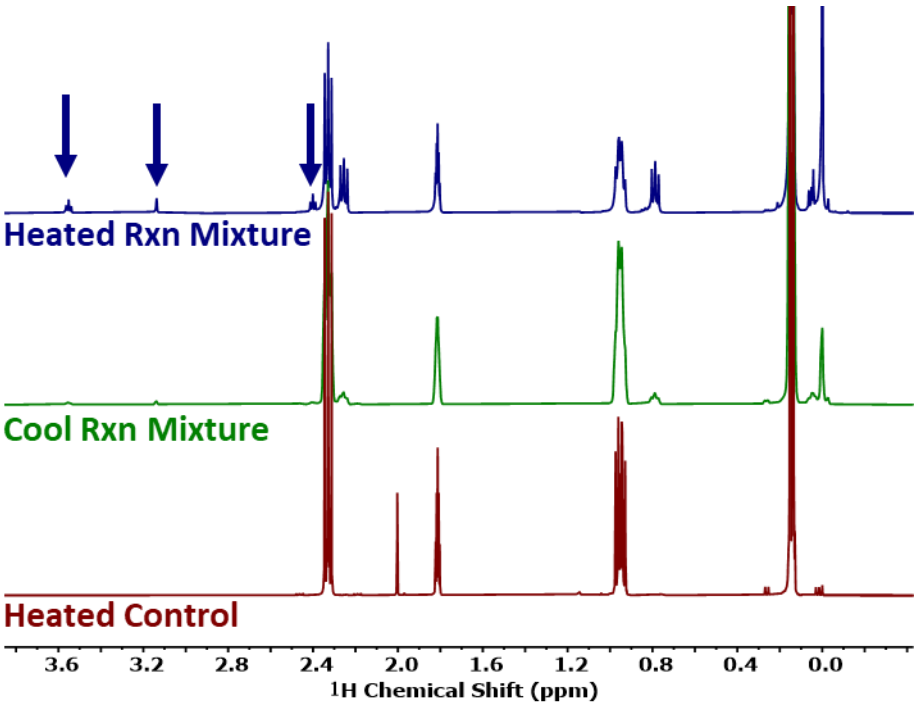

Figure S5. ^{1}H NMR spectra of a heated control 1-F solution (red), a sample of the reaction mixture that stayed cool (green), and a sample of the reaction mixture that was heated (blue). Peaks marked with blue arrows belong to the 3-hydroxypropionitrile.

In Figure S5 above, three ^{1}H peaks consistent with the formation of 3-hydroxypropionitrile (structure provided in Figure S4 above) are observed in the heated reaction mixture spectrum, including a triplet feature at 2.39 ppm, a singlet at 3.14 ppm, and another triplet at 3.55 ppm. These peaks are either totally absent or not distinguishable in the cool reaction mixture spectrum and the heated control, indicating that they must be formed by the product species at elevated temperatures, suggesting that the appearance of 3-hydroxypropionitrile is an artifact caused by the heating of the sample for GC analysis and in fact the singular product of the reaction between the superoxide radical and the 1-F additive is the third eluent identified in Figure S4.

3.9 References

(1) Lee, K. H.; Song, E. H.; Lee, J. Y.; Jung, B. H.; Lim, H. S. Mechanism of gas build-up in a Li-ion cell at elevated temperature. *Journal of Power Sources* **2004**, *132* (1-2), 201-205. DOI: 10.1016/j.jpowsour.2004.01.042.

(2) Mao, C.; Ruther, R. E.; Geng, L.; Li, Z.; Leonard, D. N.; Meyer, H. M., 3rd; Sacci, R. L.; Wood, D. L., 3rd. Evaluation of Gas Formation and Consumption Driven by Crossover Effect in High-Voltage Lithium-Ion Batteries with Ni-Rich NMC Cathodes. *ACS Appl Mater Interfaces* **2019**, *11* (46), 43235-43243. DOI: 10.1021/acsami.9b15916 From NLM PubMed-not-MEDLINE.

(3) Guillot, S. L.; Usrey, M. L.; Peña-Hueso, A.; Kerber, B. M.; Zhou, L.; Du, P.; Johnson, T. Reduced Gassing In Lithium-Ion Batteries With Organosilicon Additives. *Journal of The Electrochemical Society* **2021**, *168* (3). DOI: 10.1149/1945-7111/abed25.

(4) Zhang, B.; Metzger, M.; Solchenbach, S.; Payne, M.; Meini, S.; Gasteiger, H. A.; Garsuch, A.; Lucht, B. L. Role of 1,3-Propane Sultone and Vinylene Carbonate in Solid Electrolyte Interface Formation and Gas Generation. *The Journal of Physical Chemistry C* **2015**, *119* (21), 11337-11348. DOI: 10.1021/acs.jpcc.5b00072.

(5) Lee, H.; Choi, S.; Choi, S.; Kim, H.-J.; Choi, Y.; Yoon, S.; Cho, J.-J. SEI layer-forming additives for LiNi0.5Mn1.5O4/graphite 5V Li-ion batteries. *Electrochemistry Communications* **2007**, *9* (4), 801-806. DOI: 10.1016/j.elecom.2006.11.008.

(6) Xia, J.; Harlow, J. E.; Petibon, R.; Burns, J. C.; Chen, L. P.; Dahn, J. R. Comparative Study on Methylene Methyl Disulfonate (MMDS) and 1,3-Propane Sultone (PS) as Electrolyte Additives for Li-Ion Batteries. *Journal of The Electrochemical Society* **2014**, *161* (4), A547-A553. DOI: 10.1149/2.049404jes.

(7) Kim, G.-Y.; Dahn, J. R. The Effect of Some Nitriles as Electrolyte Additives in Li-Ion Batteries. *Journal of The Electrochemical Society* **2015**, *162* (3), A437-A447. DOI: 10.1149/2.0651503jes.

(8) Zhang, Q.; Liu, K.; Ding, F.; Li, W.; Liu, X.; Zhang, J. Safety-Reinforced Succinonitrile-Based Electrolyte with Interfacial Stability for High-Performance Lithium Batteries. *ACS Appl Mater Interfaces* **2017**, *9* (35), 29820-29828. DOI: 10.1021/acsami.7b09119 From NLM PubMed-not-MEDLINE.

(9) Birrozzi, A.; Laszczynski, N.; Hekmatfar, M.; von Zamory, J.; Giffin, G. A.; Passerini, S. Beneficial effect of propane sultone and tris(trimethylsilyl) borate as electrolyte additives on the cycling stability of the lithium rich nickel manganese cobalt (NMC) oxide. *Journal of Power Sources* **2016**, *325*, 525-533. DOI: 10.1016/j.jpowsour.2016.06.054.

(10) Erickson, E. M.; Markevich, E.; Salitra, G.; Sharon, D.; Hirshberg, D.; de la Llave, E.; Shterenberg, I.; Rosenman, A.; Frimer, A.; Aurbach, D. Review—Development of Advanced

Rechargeable Batteries: A Continuous Challenge in the Choice of Suitable Electrolyte Solutions. *Journal of The Electrochemical Society* **2015**, *162* (14), A2424-A2438. DOI: 10.1149/2.0051514jes.

(11) Haregewoin, A. M.; Wotango, A. S.; Hwang, B.-J. Electrolyte additives for lithium ion battery electrodes: progress and perspectives. *Energy Environ. Sci.* **2016**, *9* (6), 1955-1988. DOI: 10.1039/c6ee00123h.

(12) Han, J. G.; Kim, K.; Lee, Y.; Choi, N. S. Scavenging Materials to Stabilize LiPF(6) - Containing Carbonate-Based Electrolytes for Li-Ion Batteries. *Adv Mater* **2019**, *31* (20), e1804822. DOI: 10.1002/adma.201804822 From NLM PubMed-not-MEDLINE.

(13) Guillot, S. L.; Peña-Hueso, A.; Usrey, M. L.; Hamers, R. J. Thermal and Hydrolytic Decomposition Mechanisms of Organosilicon Electrolytes with Enhanced Thermal Stability for Lithium-Ion Batteries. *Journal of The Electrochemical Society* **2017**, *164* (9), A1907-A1917. DOI: 10.1149/2.0671709jes.

(14) Chen, X.; Usrey, M.; Peña-Hueso, A.; West, R.; Hamers, R. J. Thermal and electrochemical stability of organosilicon electrolytes for lithium-ion batteries. *Journal of Power Sources* **2013**, *241*, 311-319. DOI: 10.1016/j.jpowsour.2013.04.079.

(15) Kaufman, L. A.; McCloskey, B. D. Surface Lithium Carbonate Influences Electrolyte Degradation via Reactive Oxygen Attack in Lithium-Excess Cathode Materials. *Chemistry of Materials* **2021**, *33* (11), 4170-4176. DOI: 10.1021/acs.chemmater.1c00935.

(16) Park, C.; Lee, E.; Kim, S. H.; Han, J.-G.; Hwang, C.; Joo, S. H.; Baek, K.; Kang, S. J.; Kwak, S. K.; Song, H.-K.; et al. Malonic-acid-functionalized fullerene enables the interfacial stabilization of Ni-rich cathodes in lithium-ion batteries. *Journal of Power Sources* **2022**, *521*. DOI: 10.1016/j.jpowsour.2021.230923.

(17) Strehle, B.; Kleiner, K.; Jung, R.; Chesneau, F.; Mendez, M.; Gasteiger, H. A.; Piana, M. The Role of Oxygen Release from Li- and Mn-Rich Layered Oxides during the First Cycles Investigated by On-Line Electrochemical Mass Spectrometry. *Journal of The Electrochemical Society* **2017**, *164* (2), A400-A406. DOI: 10.1149/2.1001702jes.

(18) Teufl, T.; Strehle, B.; Müller, P.; Gasteiger, H. A.; Mendez, M. A. Oxygen Release and Surface Degradation of Li- and Mn-Rich Layered Oxides in Variation of the Li2MnO3Content. *Journal of The Electrochemical Society* **2018**, *165* (11), A2718-A2731. DOI: 10.1149/2.0691811jes.

(19) Teufl, T.; Pritzl, D.; Krieg, P.; Strehle, B.; Mendez, M. A.; Gasteiger, H. A. Operating EC-based Electrolytes with Li- and Mn-Rich NCMs: The Role of O2-Release on the Choice of the Cyclic Carbonate. *Journal of The Electrochemical Society* **2020**, *167* (11). DOI: 10.1149/1945-7111/ab9e7f.

(20) Yabuuchi, N.; Yoshii, K.; Myung, S. T.; Nakai, I.; Komaba, S. Detailed studies of a high-capacity electrode material for rechargeable batteries, Li2MnO3-LiCo(1/3)Ni(1/3)Mn(1/3)O2. *J Am Chem Soc* **2011**, *133* (12), 4404-4419. DOI: 10.1021/ja108588y From NLM PubMed-not-MEDLINE.

(21) Castel, E.; Berg, E. J.; El Kazzi, M.; Novák, P.; Villevieille, C. Differential Electrochemical Mass Spectrometry Study of the Interface of xLi2MnO3·(1–x)LiMO2 (M = Ni, Co, and Mn) Material as a Positive Electrode in Li-Ion Batteries. *Chemistry of Materials* **2014**, *26* (17), 5051-5057. DOI: 10.1021/cm502201z.

(22) Bryantsev, V. S.; Blanco, M. Computational Study of the Mechanisms of Superoxide-Induced Decomposition of Organic Carbonate-Based Electrolytes. *The Journal of Physical Chemistry Letters* **2011**, *2* (5), 379-383. DOI: 10.1021/jz1016526.

(23) Bryantsev, V. S.; Giordani, V.; Walker, W.; Blanco, M.; Zecevic, S.; Sasaki, K.; Uddin, J.; Addison, D.; Chase, G. V. Predicting solvent stability in aprotic electrolyte Li-air batteries: nucleophilic substitution by the superoxide anion radical (O2(*-)). *J Phys Chem A* **2011**, *115* (44), 12399-12409. DOI: 10.1021/jp2073914 From NLM PubMed-not-MEDLINE.

(24) Hwang, C.; Yoo, J.; Jung, G. Y.; Joo, S. H.; Kim, J.; Cha, A.; Han, J. G.; Choi, N. S.; Kang, S. J.; Lee, S. Y.; et al. Biomimetic Superoxide Disproportionation Catalyst for Anti-Aging Lithium-Oxygen Batteries. *ACS Nano* **2019**, *13* (8), 9190-9197. DOI: 10.1021/acsnano.9b03525 From NLM Medline.

(25) Yim, T.; Woo, S.-G.; Lim, S. H.; Cho, W.; Song, J. H.; Han, Y.-K.; Kim, Y.-J. 5V-class high-voltage batteries with over-lithiated oxide and a multi-functional additive. *Journal of Materials Chemistry A* **2015**, *3* (11), 6157-6167. DOI: 10.1039/c4ta06531j.

(26) Yanmane, H.; Inoue, T.; Fujita, M.; Sano, M. A causal study of the capacity fading of $Li_{1.01}Mn_{1.99}O_4$ cathode at 80 C and the suppressing substances of its fading. *Journal of Power Sources* **2001**, *99*, 60-65.

(27) Wotango, A. S.; Su, W. N.; Leggesse, E. G.; Haregewoin, A. M.; Lin, M. H.; Zegeye, T. A.; Cheng, J. H.; Hwang, B. J. Improved Interfacial Properties of MCMB Electrode by 1-(Trimethylsilyl)imidazole as New Electrolyte Additive To Suppress LiPF(6) Decomposition. *ACS Appl Mater Interfaces* **2017**, *9* (3), 2410-2420. DOI: 10.1021/acsami.6b13105 From NLM PubMed-not-MEDLINE.

(28) Tu, W.; Xia, P.; Zheng, X.; Ye, C.; Xu, M.; Li, W. Insight into the interaction between layered lithium-rich oxide and additive-containing electrolyte. *Journal of Power Sources* **2017**, *341*, 348-356. DOI: 10.1016/j.jpowsour.2016.12.012.

(29) Zheng, J.; Xiao, J.; Gu, M.; Zuo, P.; Wang, C.; Zhang, J.-G. Interface modifications by anion receptors for high energy lithium ion batteries. *Journal of Power Sources* **2014**, *250*, 313-318. DOI: 10.1016/j.jpowsour.2013.10.071.

(30) Lee, D. J.; Im, D.; Ryu, Y.-G.; Lee, S.; Yoon, J.; Lee, J.; Choi, W.; Jung, I.; Lee, S.; Doo, S.-G. Phosphorus derivatives as electrolyte additives for lithium-ion battery: The removal of O 2 generated from lithium-rich layered oxide cathode. *Journal of Power Sources* **2013**, *243*, 831-835. DOI: 10.1016/j.jpowsour.2013.06.091.

(31) Herranz, J.; Garsuch, A.; Gasteiger, H. A. Using Rotating Ring Disc Electrode Voltammetry to Quantify the Superoxide Radical Stability of Aprotic Li–Air Battery Electrolytes. *The Journal of Physical Chemistry C* **2012**, *116* (36), 19084-19094. DOI: 10.1021/jp304277z.

(32) Laoire, C. O.; Mukerjee, S.; Abraham, K. M.; Plitcha, E. J.; Hendrickson, M. A. Elucidating the Mechanism of Oxygen Reduction for Lithium-Air Battery Applications. *Journal of Physical Chemistry C* **2009**, *113* (46), 20127-20134. DOI: 10.1021/jp908090s.

(33) Roberts, J. L.; Sawyer, D. T. Facile degradation by superoxide ion of carbon tetrachloride, chloroform, methylene chloride, and p,p'-DDT in aprotic media. *Journal of the American Chemical Society* **1981**, *103* (3), 712-714. DOI: 10.1021/ja00393a057.

(34) Nicholson, R. S.; Shain, I. Theory of Stationary Electrode Polarogrpahy: Single Scan and Cyclic Methods Applied to Reversible, Irreversible, and Kinetic Systems. *Analytical Chemistry* **1964**, *36* (4), 706-723. DOI: 10.1021/ac60210a007.

(35) Randviir, E. P. A cross examination of electron transfer rate constants for carbon screen-printed electrodes using Electrochemical Impedance Spectroscopy and cyclic voltammetry. *Electrochimica Acta* **2018**, *286*, 179-186. DOI: 10.1016/j.electacta.2018.08.021.

(36) Intan, N. N.; Pfaendtner, J. Effect of Fluoroethylene Carbonate Additives on the Initial Formation of the Solid Electrolyte Interphase on an Oxygen-Functionalized Graphitic Anode in Lithium-Ion Batteries. *ACS Appl Mater Interfaces* **2021**, *13* (7), 8169-8180. DOI: 10.1021/acsami.0c18414 From NLM PubMed-not-MEDLINE.

Chapter 4: Conclusion

Lithium-ion batteries have been and continue to be the central to the consumer electronics industry and are increasingly being targeted as solutions for the electrification of transportation and other high-performance use cases. Current battery technologies are not well suited to such aggressive applications, as conventional cell chemistries lack the necessary energy density and capacity to meet these new challenges while promising next-generation cell designs are limited by poor safety and longevity. At the heart of the lifetime and safety issues facing these cells lies the instability of the solvents necessary to facilitate the transport of Li^+ ions between the electrodes, be that the reductive instability of the carbonate solvents at the anode interface or the vulnerability of the solvent to reactive oxygen species emitted by the cathode. One of the most popular approaches to solving or at least ameliorating these interfacial and chemical stability problems has been the inclusion of additives in battery electrolytes. This thesis details the exploration of a recent and exciting class of such additives, organosilicons. Organosilicon additives have been shown to impart impressive benefits on LIBs utilizing both Si anodes and high-nickel NMC cathodes, however their mechanisms of action in these cases are not fully understood. This work provides two case studies which sought to provide insight into these additives' role in the cells which they protect.

First, we adapted a simultaneous *in operando* EQCM-EIS to the study of Si anode interfaces, allowing a novel perspective into not only the formation of the SEI layer on those surfaces but also insight into the evolution of the charge transfer dynamics of the interface during the formation process. We were able to leverage this insight to show that organosilicon additives had a profound influence on the charge transfer impedance at the anode interface during the first charge cycle, stabilizing the interface against the decomposition of the solvent. This promoted the formation of a thinner SEI layer which was enriched in LiF while containing significantly

less organic material than the layer formed without the additive. This adjustment of the surface chemistry at the anode interface led to the additive-treated cell featuring greater first cycle columbic efficiency and lower impedance growth overall.

In our second study, we performed fundamental kinetic analysis of the reaction between a series of organosilicon additives as well as structural elucidation via a combination of nuclear magnetic resonance spectroscopy (NMR) and tandem gas chromatography-mass spectroscopy (GC-MS) to determine the mechanism of action by which organosilicon additives suppress gassing under high temperature storage conditions. Cyclic voltammetry combined with a finite element simulation method showed that singly fluorinated additives are 150 times more reactive toward the superoxide radical ($O_2^{\bullet-}$), a known trigger for gas generation during storage, than ethylene carbonate. We were also able to show that doubly fluorinated additives are another order of magnitude faster than the analogous singly fluorinated additive, while the non-fluorinated additives feature no appreciable scavenging activity, indicating that the scavenging activity of these additives is very closely tied to their degree of fluorination. Overall, the reactivity of the fluorinated additives toward $O_2^{\bullet-}$suggests that even at additive concentrations, the organosilicons are sufficiently rapid scavengers to protect ethylene carbonate from $O_2^{\bullet-}$. Our study went further to determine the structure of the product formed from the reaction between the singly fluorinated additives and $O_2^{\bullet-}$, and we found that the radical scavenging reaction produced a single, electrochemically stable silanol product. It is thereby suggested that fluorinated organosilicon additives impart their gassing suppression benefit by scavenging $O_2^{\bullet-}$ into an electrochemically stable product, thereby protecting the solvent from decomposition and suppressing the evolution of gaseous byproducts.

This work provides two new perspectives into the ways in which LIBs decompose, especially those batteries that incorporate next generation cathode and anode materials. Further, the studies in this thesis apply the methods described to examine the roles played by organosilicon electrolyte additives in suppressing the deleterious side chemistries that limit such cells. The methods detailed in this study can be applied to any additive or cycling conditions, helping to elucidate the ways in which those adjustments to cell treatment and chemistry might improve battery performance and safety. Further, the conclusions and insights specifically related to the organosilicon additives presented in this work can be used to guide the rational design of next-generation silicon and fluorine containing additive species.

Appendix A: Perspectives on Designing Electrochemical Cells and Electrodes for *In Operando* Spectroelectrochemistry

DISCLAIMER:

This appendix is an informal discussion regarding unfinished works undertaken during the period of my thesis work, which were dedicated to the development of an *in operando* ATR-FTIR spectroelectrochemical system to complement the EQCM-EIS instrument developed for the work in Chapter 2. I have included this here as a memo and repository of advice for future members of my lab or other groups that may be interested in picking up where I had to leave this project off, or in adapting similar methods to their own systems. It is not intended to serve as a formal scientific report as the previous chapters of this thesis have, and as such as written conversationally and includes generalized perspectives on my experiences designing electrochemical cells, as well as building electrochemical devices through additive and subtractive thin film lithographic techniques. The perspectives offered in the following pages are my own personal opinions and advice to new students and non-experts attempting similar experiments. Please be advised that these experiments were not completed at the time of this writing, and your experiences replicating my operating procedures may vary substantially.

Designing Electrochemical Cells for Spectroelectrochemical Measurements of Lithium-ion Battery Model Systems

During this thesis, EQCM-EIS was not the only *in operando* technique we pursued. We were also interested in developing an *in operando* spectroscopic technique that would complement the gravimetric and electrochemical perspectives offered by EQCM. The goal was to build a model Si anode that would be transparent to infrared light, such that it could be utilized in a commercial attenuated total reflection Fourier transform infrared spectrometer (ATR-FTIR). To achieve this, we were able to design an electrochemical cell which built upon the lessons

learned during the development of our EQCM-EIS electrochemical cell, and we made substantial progress toward enabling the electrochemical cycling of transparent model Si anodes. Unfortunately, we were unable to fully realize this instrument, however this appendix will summarize the lessons learned during our work on this project, as well as some forward-looking perspectives on how one may be able to complete it.

When designing an electrochemical cell, especially a spectroelectrochemical system, you need to be cognizant of the behaviors of the electrochemical process you intend to study. Often, simple, large volume electrochemical cells with thin metal wire electrodes simply will not allow you to create functional models of the systems of interest. In my experience with LIB systems, for instance, I found that mass transport through the solution was very slow, and that the electrolyte systems we use were relatively resistive. When we attempted to study our model anode systems in a more conventional electrochemical cell design, with a large separation between working and counter electrodes as well as a very small, Li foil wrapped Cu wire as the counter electrode (Figure 1), the cells exhibited very large uncompensated resistances.

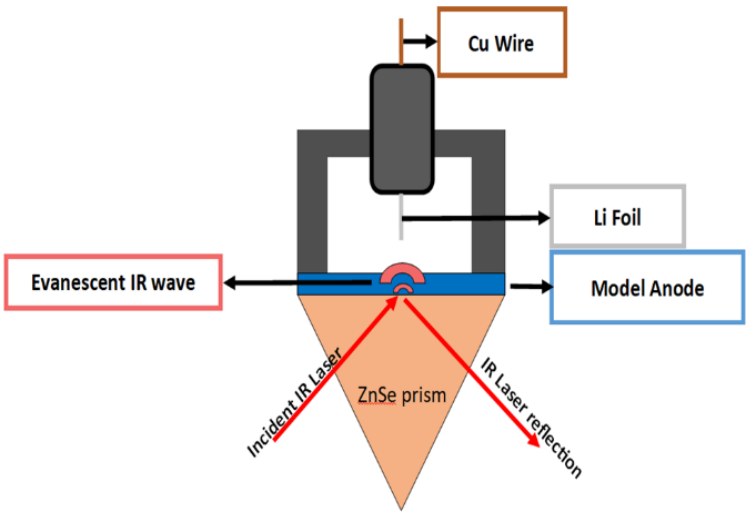

Figure 1. Cartoon representation of a large volume IR cell design with small Li metal CE/RE.

This resulted in incredibly sluggish electrochemical performance in the cell, and as a result, we failed to replicate the charging and interfacial layer formation behaviors on our electrodes that we were trying to study (Figure 2).

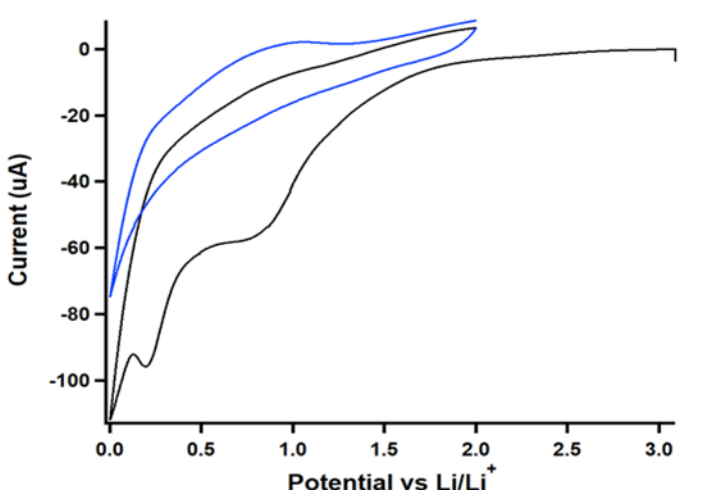

Figure 2. CV showing the poor electrochemical performance of the model anodes when cycled in the large volume electrochemical cell.

To overcome these mass transport-imposed limitations, the cell design was changed to a thin-layer cell model, in which the counter electrode geometry was overhauled to be a large, planar electrode lain parallel to the working electrode, and the two large, flat electrodes were separated by a thin (~200 µm) Teflon membrane (Figure 3).

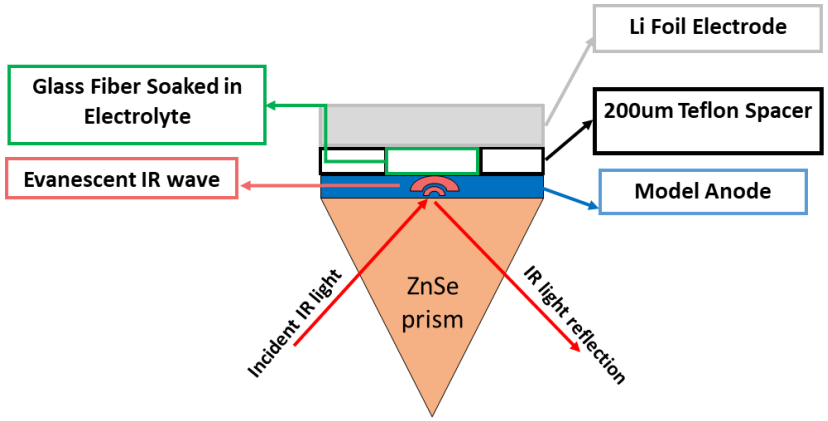

Figure 3. Cartoon representation of the thin layer cell design concept, where the Li metal CE/RE is larger and lain parallel to the model anode WE surface, separated by a very thin Teflon membrane. Electrolyte is retained in the near surface region using a glass fiber filter.

After making these design adjustments, the performance of the cell improved greatly, and it began to replicate the electrochemical behavior of real batteries (Figure 4) much more closely.

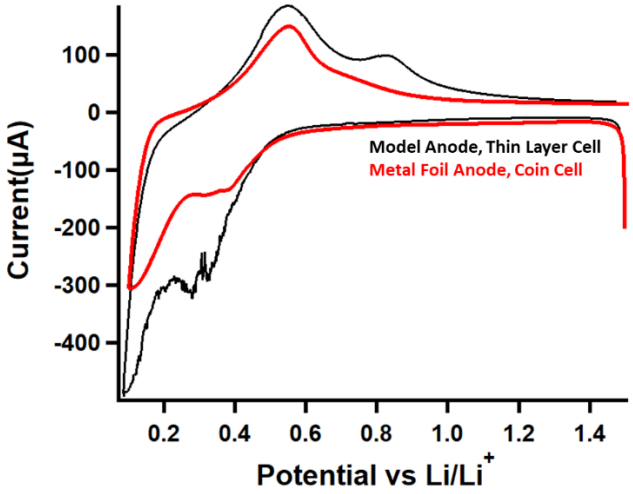

Figure 4. CV data of the initial cycle of a fabricated model anode in the thin layer cell geometry (black) and the initial cycle of the same Si thin film deposited onto a piece of Ti shim and installed into a coin. Both cells were cycled at 0.5 mV/s.

Another concern of the spectroelectrochemical experiments we were attempting was that we needed to be able to distinguish between molecules that were bound or adhered to the model electrode surface, and molecules that were merely present in the solution but not associated with our electrode. The easiest way to do this is to flush the cell with clean solution, carrying away loosely on unassociated species and leaving behind only those that are tightly associated with the surface; however this kind of solvent exchange is not possible using the glass fiber filter solution reservoir pictured in Figure 3. Enabling this type of operation means solvent changing flow systems need to be considered alongside the electrochemical and spectroscopic needs of the system. In the case of the cell designed for the *in-operando* ATR-FTIR, this was achieved by including two ¼-28 tapped holes in the top of the cell cap. On the exterior side, these tapped holes allow users to connect standard plastic flangeless fittings to the electrochemical cell, and thus easily connect tubing which would carry wash solution to and through the system. On the

interior of the cell, these tapped holes connect to untapped narrow passages that end in the cell volume just in front of the counter electrode position (Figure 5). I was not personally able to verify this design's performance, however other lab members reportedly found it to be very similar to that of the thin layer system, (and thus a coin cell) as shown above.

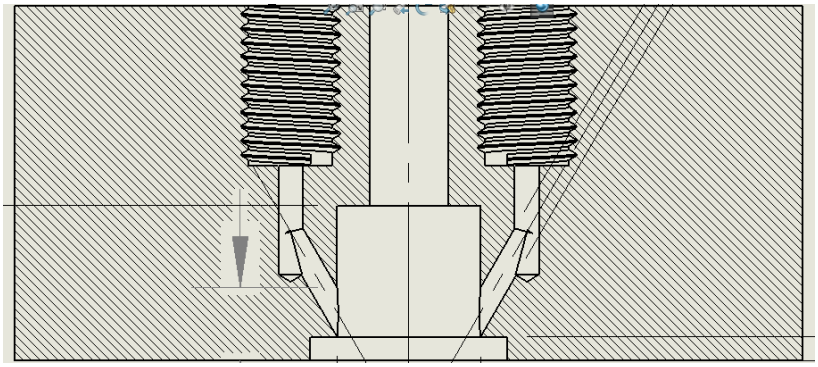

Figure 5. Engineering drawing of the new thin layer electrochemical cell cap designed to allow solution exchange during *in operando* spectroelectrochemical experiments.

This cell cap would sit atop the model anode surface and the ZnSe prism shown in the previous cartoon representations. The threaded columns represent the tapped flow ports through which the electrolyte solution can be exchanged, along with the untapped flow channels designed to allow access to the thin interelectrode spacing. The center void space would be occupied by a press-fit stainless-steel plug, situated so that its bottom surface sits just above the openings for the oblique untapped channels. The slightly enlarged space just above the bottom surface of the cap would house an O-ring for sealing the cap against the electrode surface and would also define the bottom of the electrochemical cell volume. These drawings are scaled such that the interelectrode space here is about 1 mm. During cell assembly in the glovebox, the bottom surface of the stainless-steel plug would be covered with a small circular cutting of 0.5 mm thick Li foil, further reducing the interelectrode spacing to a figure more in line with that necessary to facilitate rapid mass transport and limit uncompensated resistance.

Whatever your electrochemical system of interest, it is incredibly important that you understand how the model system that you are building is supposed to behave and drive your design of the cell toward that behavior. Your spectroscopic results are only as valid as the quality with which the proper electrochemistry is being replicated in the cell. If you are not building a thin layer cell, these designs might not be particularly useful. You may find more useful the book *Laboratory Techniques in Electroanalytical Chemistry* by Peter T. Kissinger and William R. Heineman, which has some great illustrations of different spectroelectrochemical devices, as well as a plethora of references to articles that use them.

Nanofabrication of Infrared-Transparent Electrode Systems

Moving to the design and fabrication of electrodes for these studies, we again encounter the need to design around multiple, conflicting needs. This is especially the case for IR-transparent electrodes, as most of the materials conventionally used as conductors or current collectors (i.e. metals) are IR opaque. As such, our need for the electrode to be conductive will run headlong into our need for the material to be IR transmissive. The solution chosen to work around this conflict in material properties was to create a current collector for this electrode which had an array of holes etched through it. To minimize the resistive loss (IR drop) across these holes, they needed to be kept as small as possible. To maintain IR light transmissivity, however, the holes needed to be at least as large as the longest wavelength of light that we intended to pass through then. In the case of IR studies on relatively insulating electrodes, hole diameters will likely be on the order of 10 to 30 μm, and for our studies we chose a median value of 20 μm. Achieving a regularly spaced, uniform array of etched features this size across the surface of an electrode requires the use of photolithography, and the remainder of this appendix

will detail my approach to fabricating high quality Ti films which are both conductive and transparent.

First, this work must be completed in a cleanroom to protect the electrodes in the process of being etched from particle contamination. My approach used a double side polished, float zone purified intrinsic silicon wafer. Silicon wafers are extremely useful as substrates for this kind of fabrication work, as most common tools and equipment in cleanroom facilities are built around them making cleaning, additive, patterning, etching, and dicing wafer pieces relatively easy. Si wafers are also easily adapted to work as optical substrates, as they are very IR transmissive at low conductivities and when polished can form very good optical contact with other flat optical elements. You must also choose an appropriate metal to use as your patterned current collector. I used Ti for a few reasons. First, Ti adheres well to Si, and as I was building these substrates as model Si anodes and would be adding a layer of amorphous Si on top of the current collector layer to serve as the model anode material, adhesion between layers was key. Second, Ti is relatively stable in the LIB environment and will not alloy Li, which is the primary reason for avoiding Au or Ag, which are of course much more conductive metals. From here I will detail a standard operating procedure for fabricating my substrates and will include brief commentary on sections where appropriate to provide some insight and advice that I think might be helpful.

Section 1: Preparing Your Wafer and Initial Metal Layer

When starting with a new Si wafer, your first step is always to wash the side of the wafer you intend to pattern and etch, called the critical surface. If the wafer is new and has been stored in a cleanroom, it should be free of any major contaminant, so I usually wash with acetone, isopropanol (IPA), and water on a spin coater. Then you'll bring the cleaned wafer to your

deposition tool, here we will use an electron beam metal evaporator, and load it according to the tool instructions. We will not go into the specifics of operating any tool here, just generalizable guidelines for how the materials should be treated.

1. Place your wafer on a spin coater using the appropriate vacuum chuck.
2. Get three squirt bottles, one each of acetone, IPA, and deionized water
3. Set the spin recipe to about 5000 rpm for 30 seconds and start the spin coater.
4. With the acetone bottle in one hand and the IPA bottle in the other, first spray acetone at the surface of the spinning wafer for about 5 seconds to get it fully wet and allow the excess solvent to be spun off.
5. After fully wetting the surface with acetone, start trailing the acetone stream to the edge of the wafer and at the same time, begin spraying IPA at the center so that the wafer surface is never dry. Even process grade acetone can leave residue behind on your surface if it is allowed to dry. This residue can ruin your lithography, so it is critical that it is removed with the IPA step.
6. After 10 seconds of IPA, repeat the trailing maneuver with the water bottle, slowly replacing the IPA stream with water.
7. After 10 more seconds of washing with water, trail the water stream to the edge of the wafer and allow it to spin dry for the remainder of the cycle.
8. If any spots or reside remains, repeat these three washing steps, and if that does not clear it consider using piranha solution.
9. Once clean, blow the wafer dry on both sides with filtered air or nitrogen and bring to the deposition tool, take special care to protect the critical side you just washed.

10. In the case of the metal evaporator process used for my electrodes, you want to deposit your Ti layer at a limited deposition rate to ensure the layer is flat. For my layers, I limit the vacuum chamber pressure to below $2 \cdot 10^{-6}$ torr and the deposition rate to no more than 0.5 Å/s.
11. For your metal layers, you must find a balance between the maximum thickness that you can reliably etch through, and the minimum thickness required to keep the conductivity of the layer high. In my experience with Ti layers, anything thinner than ~50 nm will be more resistive than the bulk metal, and anything thicker than ~150 nm will not etch cleanly. For these reasons, I deposit 125 nm of Ti metal on my wafer in this evaporation step. I find that after etching my 20 μm holes, the conductivity of the layer tends to fall by about 30%, so keep this in mind when designing your own electrodes. Etching smaller holes will lessen the severity of this effect, wider holes will worsen it, and thinner layers will suffer more than thicker layers.
12. Unload your wafer, now coated on one side with Ti metal.

Section 2: Dicing Your Coated Wafer

In my process, I used a photomask which was designed to expose one small, 12x17 mm piece at a time, with multiple hole diameters available to me on the mask. This provided me with flexibility in making pieces at many different hole diameters (and thus degrees of conductivity and transmissivity), however it made patterning and etching many pieces at a time quite tedious. If you are relatively confident in the hole diameter you want to use, it will simplify your processing immensely to design and acquire a photomask which will expose an entire wafer at once with a uniform distribution of your hole array. In that case you would go straight from depositing your metal layer to photolithography, pattern transfer, etching, and finally dicing the

fully etched wafer at the very end. The guidance here may still be of use to you; however, the precise details of etching and development time will likely be different when done on a whole wafer.

1. Take your newly coated wafer back to the spin coater, Ti side up, and coat the surface in S1813 photoresist.
2. Spin the wafer at 5000 rpm for 35 seconds to distribute the photoresist (PR), and then place on a hotplate set to 110 °C (again, Ti and PR side up) to cure for 2 minutes. This will layer of cured photoresist will protect the critical surface of the wafer from chipping or scratching during dicing.
3. Take the coated wafer to your dicing saw and cut the wafer into as many 12x17 mm rectangular pieces as you can get. With a 3-inch wafer, I typically got around 15 pieces.
4. Take your new pieces back to the spin coater and clean the PR from them thoroughly using the washing steps outlined in Section 1 (steps 1-9). If you applied the protective layer just before dicing, it should come off easily, however if the layer sits overnight and is allowed to dry out, it will be more difficult.
5. With the pieces clean and dry, it is time to perform the photolithography.

Section 3: Photolithography and Pattern Transfer

This section, from photolithography to etching, is the most critical period of the fabrication process and the most sensitive. You will likely have to optimize the details presented here for yourself, so I will provide as much advice as I can about what is *supposed* to happen so you can use my recipe as a starting point.

The first and most important thing to know here is that you must apply, expose, and develop the photoresist AND etch the metal layer in the SAME DAY. Do not allow the coated

wafers to sit overnight at any point from the start of this section until the metal is etched as drying out the PR layer will mean that it will not properly take the pattern from the mask, and thus it will not properly transfer that pattern to the metal layer during etching.

The second tip I have for you is to get a wafer or piece dipper of some kind that you can use during the HF etching process. HF is incredibly dangerous, and you do not want to be holding wafer pieces in an HF solution with tweezers. Dipping cages or other holders can be purchased online from various cleanroom suppliers, or if you have access to a machine shop can be made custom. Make sure whatever you use is made of Teflon or another HF resistant material.

1. Ensure wafer pieces are clean and very dry, as the adhersion and uniformity of the PR layer we are about to apply will affect the quality of the etching later.
2. Take your clean wafer piece and mount it to the appropriate spin coater vacuum chuck. Center the piece as best you can, as this will ensure that your PR layer is applyied uniformly.
3. Add a small, ~1mm drop of S1813 PR to the center of the wafer piece, and spin at 5500 rpm for at least 35 seconds. This is aggressive, but because your piece is small and rectangular, the edges are liable to accumulate PR. The higher spin rate helps to wick that off, keeping the layer more uniform.
4. Cure the wafer pieces on a hot plate at 110 °C for 2 minutes. This is also a long cure, but it is important that the pieces are not tacky or sticky during exposure, as they will otherwise stick to the photomask during exposure.
5. Take the cured pieces and your photomask to the appropriate mask aligner and expose the pieces in a soft contact mode using 250 nm light at an intensity of 10.0 J/cm^2 for 6.1 seconds.

6. After exposure, develop the PR layer using MF 321 developer for 60 seconds. During development, hold the piece gently using a pair of plastic tipped tweezers and gently swish them back and forth. This agitation is important to ensure that the exposed PR is fully washed out of the wells you are creating in the PR layer.
7. After 60 seconds of development, wash the piece in flowing water to stop the development process, and gently blow the piece dry in filtered air or nitrogen.
8. Once you have all the pieces developed, your PR layer should have the exact same topography as the metal layer will after etching. Take a few pieces and examine the PR layer under a microscope to ensure that the PR layers appear to be properly and consistently developed. This is your last chance to fix any issues, as the developed PR is easily washed off and you can try again. If you fail to catch an error until after etching the metal, however, you are forced to start over completely.

If everything has gone well, you should see consistent, beautiful layers that look something like this:

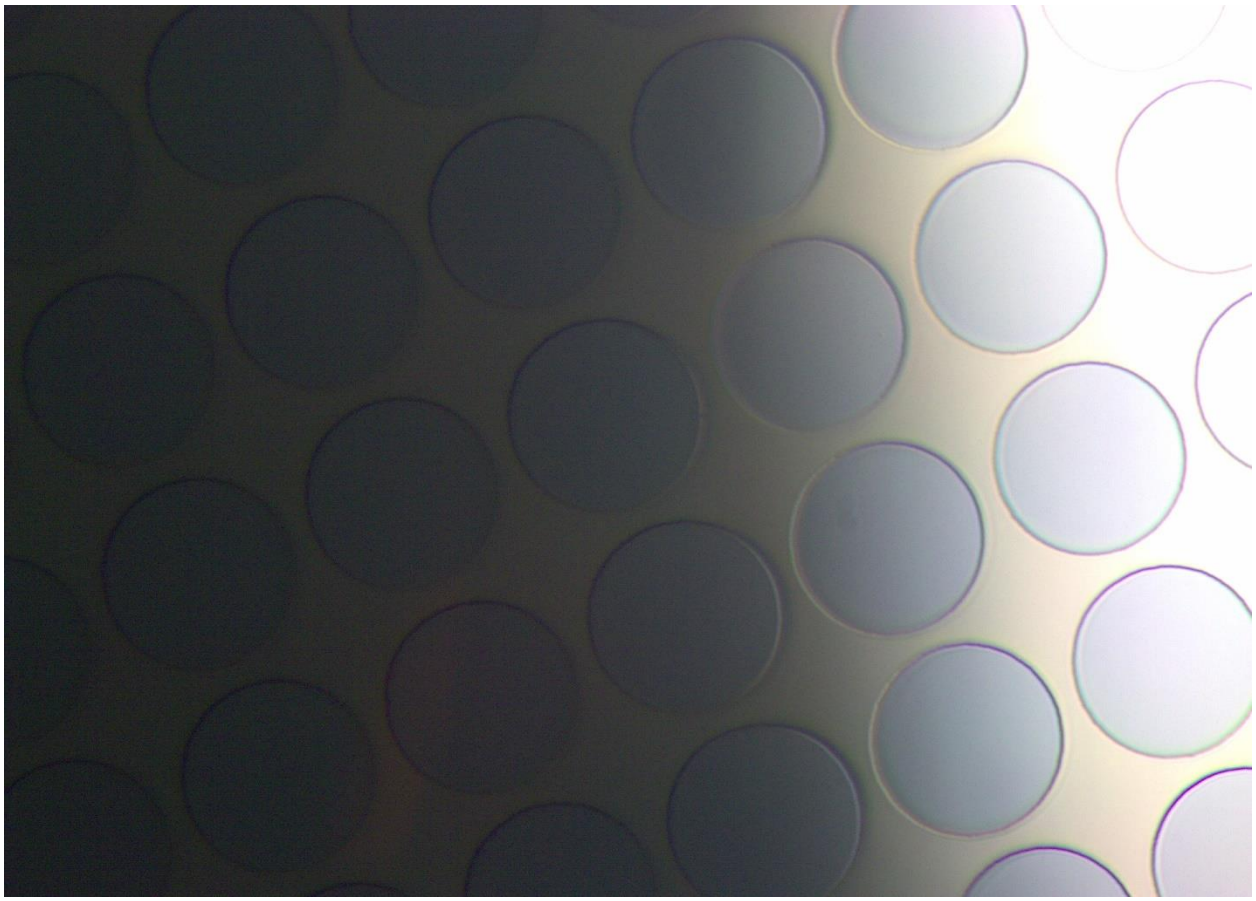

Figure 6. Microscope image of successfully fabricated electrode surface. The yellow-ish elevated field is the Ti metal layer, and the off-white, recessed circles are the bare Si wafer beneath.

Troubleshooting the PR layer pattern transfer:

There are a few things that I have observed when working out the PR exposure and pattern transfer, and I will explain what they are and how to address them. First and most easily are over and under development of the exposed film. What I will show you here are images of the metal layer when over- or underdeveloped, as the color contrast is better between the metal and Si that between PR and metal, making these images clearer.

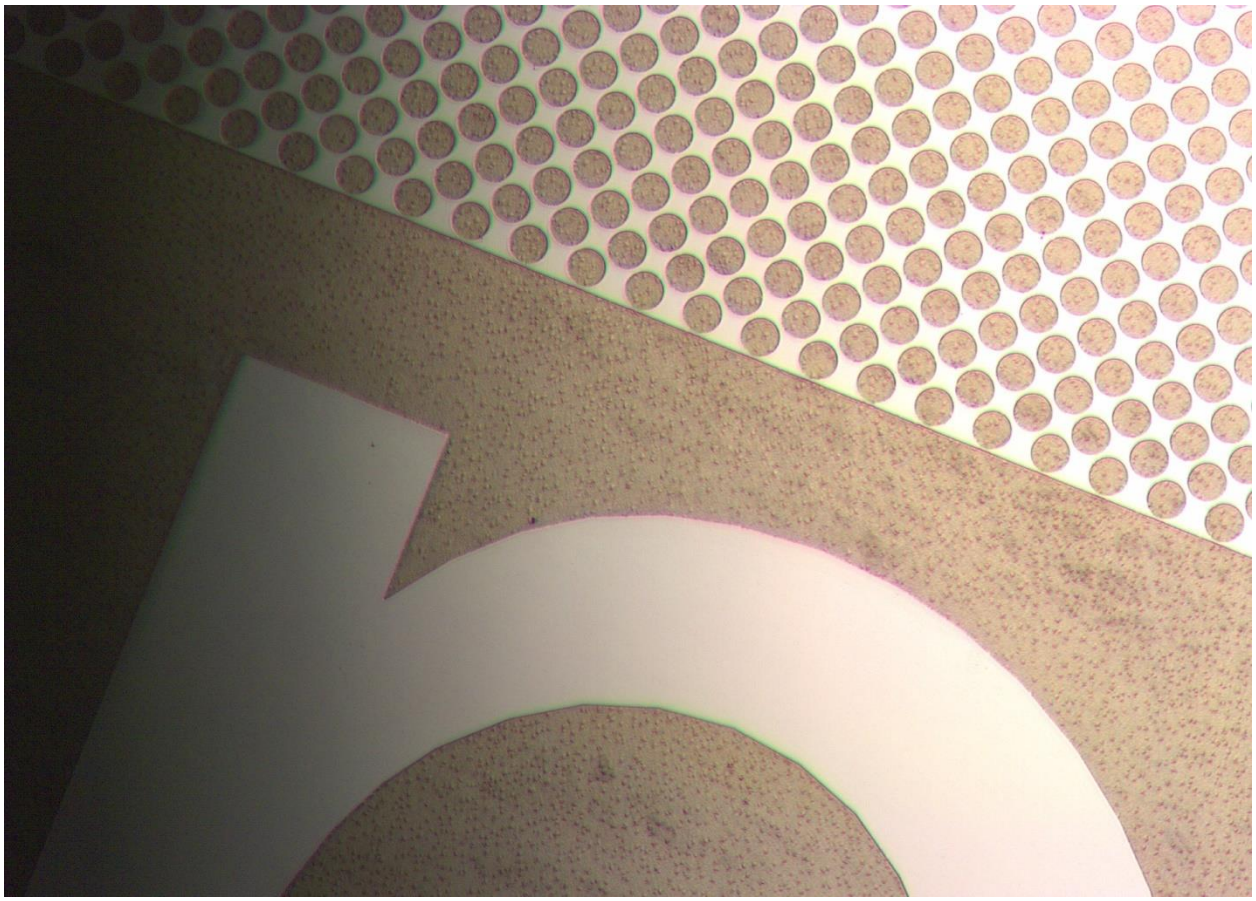

Figure 7. Underdeveloped PR layer resulting in ‘scum’ or excess photoresist sitting in wells after development. These specs on what should be the bare Si surface are excess undeveloped PR and will prevent complete etching in the wells, ruining the transparency of the layer.

There are three solutions to underdevelopment. You could try developing longer or agitating the solution during development a bit more aggressively to encourage complete solubilization of the exposed polymer. You could also increase the exposure dosage, but this is unlikely to help unless the PR layer is much thicker than this guide expects. Finally, you may need to add a plasma ashing step between developing the PR layer and metal etching. Plasma ashing uses a low power O_2 plasma to burn off a very thin layer of the photoresist, hopefully also removing the small amount of nearly invisible scum at the bottom of your wells. This also burns the undeveloped PR, so keep plasma ashing runs to <20 seconds.

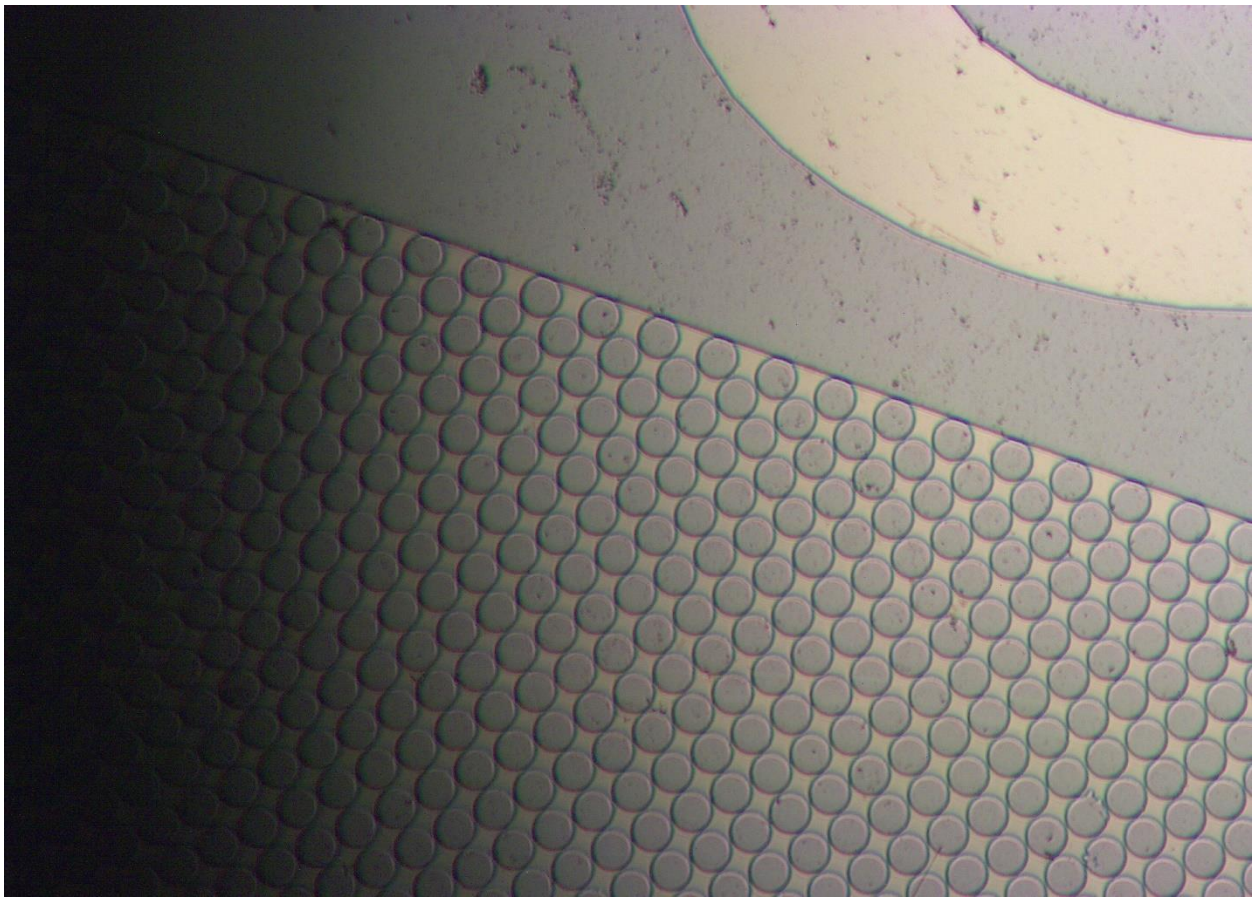

Figure 8. Microscope image of a wafer that has been over-etched.

Over-etching of a layer will cause the thinning of the walls between wells. This will result in increased resistivity across the metal layer can eventually result in the electrical contact across the surface being broken. Here we see how the holes in the layer have grown too large and the isthmuses of Ti between them have nearly been completely consumed. The only solution to this problem is to etch for a shorter amount of time. In the case of developer issues, develop for less than the original 60 seconds and agitate more gently. It is not recommended that you cut the agitation entirely, as this could lead to the previously described scum problem.

Section 4: Etching the Metal

For this step, regardless of your piece size you need a dipper of some kind to let you expose your pieces to the solution without placing your hands directly above the solution.

1. Load your wafer pieces into a dipping container of some kind. Ensure that pieces are not crowded, and that solution can flow freely across the critical surfaces of each piece to maintain uniform etching.
2. Bring your wafer pieces to the HF etching bench. This prep was developed using 6:1 NH_4:HF buffered oxide etch (6:1 BOE) in a flowing recirculation bath. For my wafers, I found that 125 nm of Ti was well etched after 45 seconds in the flowing 6:1 BOE, after which you must transfer the pieces into a series of cascading water baths to remove the HF and stop the etching process.
3. Rinse the wafer pieces for 1 minute in each of three cascading water baths. If you lack such a bath system, rinse the pieces under flowing water for at least 1 minute, or until runoff from rinsing the pieces and dipper into a bowl of sodium bicarbonate no longer reacts. Be sure to wash both the basket of the dipper and the handles vigorously. Test water droplets on all parts of the dipper with litmus paper to make sure no acid remains, and when in doubt just wash it more.
4. Remove your washed wafers from the dipper and take back to the spin coater to remove the PR one more time with the same steps as in Section 1 (steps 1-9).
5. Your metal layer is now etched, and the fabrication is complete. Examine the results under a microscope.
6. If your layers did not etch properly, you can dip them back into the BOE bath to completely remove the Ti layer and start over.

Troubleshooting the metal etching process.

My advice regarding troubleshooting the metal etching process is going to be very similar to the development process, as they are very similar. If you experience incomplete etching of the wells, as you can see in Figure 7, you can etch longer or try a more concentrated etchant. Plasma ashing can also help to ensure that residual photoresist is not causing the issue. One issue I want to mention is under-etching caused by a metal layer which is too thick, the results of which are seen in Figure 9.

Figure 9. Microscope image of a 300 nm Ti layer etched for 2.5 minutes.

Here we see a Ti layer which is much too thick to etch at 300 nm, even after 2 and a half minutes of exposure to the BOE etchant. Once the layers get too thick, the downward etching process starts to slow, and the layers will begin to be etched laterally through walls separating the wells. This will lead to incomplete etching at the bottom of wells and the distortion of the shape of the wells, as seen in Figure 9.

Over-etching will result in the same problems as described in the previous section, even if the PR layer was developed correctly. When the wafer pieces are submerged in the etchant, Ti metal is dissolved in all direction, however the vertical dimension is favored due to diffusion being fastest in that direction so long as the layer is thin. If the piece sits in the etchant for too long, however, the etchant will begin to etch laterally through the wells, leading to distortion of the well shape and loss of electrical conductivity across the surface. Evidence of over-etching can be seen in Figure 8 above.